COMPARAISON DES ENVIRONNEMENTS SÉDIMENTAIRES À PROXIMITÉ DES GLACIERS HUMBOLDT (GROENLAND) ET EUGÉNIE-DOBBIN (ÎLE D'ELLESMERE)

Mémoire présenté
dans le cadre du programme de maîtrise en océanographie
en vue de l'obtention du grade de maître ès sciences

PAR
© Christian Bicera Nfundiko

Mars 2024

Composition du jury :

Urs Neumeier, président du jury, ISMER-UQAR

Jean-Carlos Montero-Serrano, directeur de recherche, ISMER-UQAR

Guillaume St-Onge, codirecteur de recherche, ISMER-UQAR

Alexandre Normandeau, codirecteur de recherche, Commission Géologique du Canada-Atlantique

Matt O'Regan, examinateur externe, Stockholm University

Dépôt initial le [13-12-2023] Dépôt final le [28-03-2024]

Nos limites et nos succès seront souvent basées sur les attentes que nous avons envers nous-mêmes. Ce que l'esprit croit, le corps le transforme en résultats.

Denis Waitley

REMERCIEMENTS

Je tiens tout d’abord à remercier infiniment à mon directeur Jean-Carlos Montero-Serrano pour sa sagesse, sa patience, ses conseils et toutes les orientations qu'il m'a données au cours de ma formation et dans la réalisation de ce travail.

Un grand merci aussi à mes co-directeurs Guillaume St-Onge et Alexandre Normandeau pour leurs commentaires et suivis durant mon programme d’études. Je remercie également Urs Neumeier (ISMER-UQAR) et Matt O'Regan (Université de Stockholm) pour leurs commentaires constructifs sur la première version du mémoire.

Merci à mon épouse Osiris Gonzalez, Ana-Sofia, Christian-Daniel, Imani, Ray, Symy et Jean-Pierre ; à toute la famille Nfundiko ainsi que la famille Gonzalez Galvan.

Merci aussi à mes collègues de l’ISMER, María-Emilia, Chloé, Marie-Anne, Arthur, Hugo, Élodie, Juliette, Brice, Quentin, Fella, Florian, Pauline, Victor, Freddy, Flavie et Yves.

En fin un grand merci à Quentin Beauvais, Dominique Lavallée et Claude Belzile pour la formation et l'aide à la manipulation des instruments de laboratoire à l’ISMER-UQAR. Merci aussi à Nicolas Van Nieuwenhove (UNB) pour le tri des foraminifères des carottes.

AVANT-PROPOS

Ce mémoire de maitrise est présenté en trois parties : une introduction générale rédigée en français, d'un chapitre principal rédigé en anglais sous la forme d'article scientifique en prévision d'être soumis pour publication à la revue internationale « Journal of Quaternary Science » ou « Boreas », et une brève conclusion générale rédigée en français. L'article présenté dans ce mémoire de maîtrise : Bicera Nfundiko, C., Montero-Serrano, J.-C., St-Onge, G., Normandeau, A. *Comparison of the sedimentary environments near the Humboldt (northwest Greenland) and Eugenie (Ellesmere Island) glaciers*, a été rédigé par moi-même avec la supervision de Jean-Carlos Montero-Serrano et de Guillaume St-Onge de l'ISMER-UQAR et d'Alexandre Normandeau de la Commission Géologique du Canada (section Atlantique). En tant que premier auteur, ma contribution fut la réalisation des analyses granulométriques, minéralogiques, préparation des échantillons pour les datations au radiocarbone (^{14}C) et la rédaction de l'article. Jean-Carlos Montero-Serrano, Guillaume St-Onge et Alexandre Normandeau ont fourni l'idée originale, l'implémentation du développement de la méthode et la formation nécessaire pour réaliser les analyses de laboratoires et ont contribué à la rédaction et révision de l'article. Quentin Beauvais (ISMER-UQAR) à effectuer les analyses de propriétés physiques des carottes et Nicolas Van Nieuwenhove (UNB) a effectué le tri des foraminifères des carottes AMD1903-12GC, 02PC, 04GC et 02GC pour les datations au ^{14}C. Les datations au ^{14}C ont été effectuées au

Laboratoire de spectrométrie de masse par accélérateur André E. Lalonde (Université d'Ottawa) et au Alfred Wegener Institute (AWI-MICADAS, Allemagne).

Au cours de ma maîtrise, j'ai eu l'opportunité de présenter les principaux résultats de mon projet de recherche lors de divers congrès nationaux :

Bicera Nfundiko, C., Montero-Serrano, J.-C., St-Onge, G., Normandeau, A. (2022). *Signatures granulométriques des carottes recueillies à proximité des glaciers Humboldt et Eugenie (détroit de Nares) au cours de l'Holocène*. Congrès annuel de Québec-Océan, Québec, du 31 janvier au 3 février 2022 (congrès virtuel; affiche).

Bicera Nfundiko, C., Montero-Serrano, J.-C., St-Onge, G., Normandeau, A. (2022). *Comparaison des environnements sédimentaires à proximité des glaciers Humboldt (Groenland) et Eugénie (l'Île d'Ellesmere)*. Congrès des étudiant.e.s du GEOTOP, Québec, du 29 au 31 mars 2022 (congrès virtuel; affiche).

Bicera Nfundiko, C., Montero-Serrano, J.-C., St-Onge, G., Normandeau, A. (2023). Lithofaciès des sédiments holocènes et processus sédimentaires à proximité des glaciers Humboldt (Groenland) et Eugénie (l'Île d'Ellesmere). Congrès des étudiant.e.s du GEOTOP, Québec, du 10 au 12 mars 2023 (congrès; affiche).

RÉSUMÉ

Le bassin de Kane fait partie du détroit de Nares, qui relie l'océan Arctique à la baie de Baffin. Cette zone est fortement influencée par les décharges glaciaires provenant des glaciers de l'est de l'île d'Ellesmere et de la marge nord-ouest du Groenland. L'étude de séquences sédimentaires marines à proximité de ces glaciers peut aider à mieux comprendre leur dynamique au-delà de l'enregistrement historique, et donc à mieux comprendre l'effet des changements climatiques futurs sur ces glaciers. Dans ce contexte, ce projet de recherche vise à étudier les propriétés physiques, sédimentologiques et minéralogiques des trois carottes sédimentaires recueillies près du glacier Humboldt (nord-ouest du Groenland) et de deux carottes recueillies près des glaciers Eugénie-Dobbin (baie de Dobbin, île d'Ellesmere) afin de documenter la réponse de ces glaciers à l'évolution des conditions océaniques et climatiques au cours de l'Holocène. L'ensemble des résultats montre trois lithofaciès (LF) distinctifs à Humboldt (H) et à Eugénie-Dobbin (ED) qui indiquent des variations considérables des processus sédimentaires au cours de l'Holocène. Près du glacier Humboldt, LFH1 représentant ainsi un environnement glaciaire proximal dominé par les rejets d'eaux de fonte (~14 à 7,8 cal ka BP). LFH2 suggère qu'un environnement glaciaire distal prédomine pendant l'Holocène moyen avec une influence répétée de débris délestés par les icebergs (IRD; 7,8 à 5,2 cal ka BP). LFH3 reflète le retrait du front glaciaire vers la côte (5,2 à 1,5 cal ka BP), suivi d'une re-croissance (1,5 cal ka BP à nos jours). La dynamique sédimentaire près du glacier Humboltd est influencée principalement par l'apport des sédiments de la source d'Ellesmere-Inglefield avec un apport important de sédiments riche en carbonates provenant de la partie nord du canal Kennedy et/ou le sud de la terre de Washington au début de la déposition de le LFH3. Près du glacier Eugénie-Dobbin, LFED1 est considéré comme représentant un environnement proche des marges glaciaires influencé par la présence d'une plate-forme glaciaire étendue de la baie de (avant 8,0 cal ka BP). LFED2 est interprété comme un environnement glaciaire distal influencé par la déglaciation de la baie Dobbin et par le retrait vers l'intérieur des terres des glaciers autour de la baie (8,0 à 3,0-2,2 cal ka BP), tandis que LFED3 est caractérisé par une boue sableuse avec des IRD disséminés qui reflètent une période de croissance des glaciers autour la baie associée au refroidissement néo-glaciaire (3,0-2,2 cal ka BP à nos jours). La dynamique sédimentaire près du glacier Eugénie-Dobbin est influencée principalement par l'apport de carbonates détritiques provenant de l'île d'Ellesmere tout le long de ses trois faciès avec une influence secondaire de sédiments provenant du détroit de Nares pour la carotte situe à l'entrée de la baie.

Mots clés: Glacier Eugenie; Glacier Dobbin; Glacier Humboldt; Holocène; sédimentologie; minéralogie; géochimie; dynamique des glaciers ; dynamique sédimentaire.

ABSTRACT

The Kane Basin is part of Nares Strait, which links the Arctic Ocean to Baffin Bay. This area is strongly influenced by glacial discharges from glaciers on eastern Ellesmere Island and the northwestern margin of Greenland. The study of marine sedimentary sequences in the vicinity of these glaciers can help to better understand their dynamics beyond the historical record, and thus to better understand the effect of future climate change on these glaciers. In this context, this research project aims to study the physical, sedimentological, and mineralogical properties of three sediment cores collected near the Humboldt (northwest Greenland) and two Eugenie-Dobbin (Dobbin Bay, Ellesmere Island) glaciers, to document the response of these glaciers to changing oceanic and climatic conditions during the Holocene. The overall results show three distinctive lithofacies (LF) at Humboldt (H) and Eugenie-Dobbin (ED), indicating considerable variations in sedimentary processes during the Holocene. Near the Humboldt glacier, LFH1 represents a proximal glacial environment dominated by meltwater discharge (~14 to 7.8 cal ka BP). LFH2 suggests that a distal glacial environment prevailed during the Middle Holocene, with repeated influence from ice rafted debris (IRD) from by icebergs (IRD; 7.8 to 5.2 cal ka BP). LFH3 reflects the retreat of the glacier front towards the coast (5.2 to 1.5 cal ka BP), followed by re-growth (1.5 cal ka BP to present). Sedimentary dynamics near Humboltd glacier are influenced mainly by the contribution of sediment from the Ellesmere-Inglefield source with a significant input of detrital carbonate sediments from the northern part of the Kennedy Canal and/or southern Washington Land at the beginning of the deposition of LFH3. Near the Eugenie-Dobbin glacier, LFED1 is considered to represent an environment close to glacial margins characterized by the presence of an extensive Dobbin Bay ice shelf (prior to 8.0 cal ka BP). LFED2 is interpreted as a distal glacial environment influenced by the Dobbin Bay deglaciation and by the landward retreat of glaciers around the bay (8.0 to 3.0-2.2 cal ka BP), while LFED3 is characterized by a sandy mud with scattered IRDs reflecting a period of glacier growth around the bay associated with Neoglacial cooling (3.0-2.2 cal ka BP to present). Sediments near Eugenie-Dobbin Glacier are mainly comprised of detrital carbonate input from Ellesmere Island in three facies with a secondary influence of sediments from the Nares Strait in the core located at the entrance to the bay.

Keywords: Eugenie Glacier; Dobbin Glacier; Humboldt Glacier; Holocene; sedimentology; mineralogy; geochemistry; glacier dynamics; sedimentary dynamics.

TABLE DES MATIÈRES

LISTE DES TABLEAUX

LISTE DES FIGURES

LISTE DES ABRÉVIATIONS, DES SIGLES ET DES ACRONYMES

AMOC *Atlantic Meridional Overturning Circulation,* Circulation méridienne detournement de l'Atlantique.

BIC *Baffin Island current*, Courant de l'île de Baffin.

BP *Before 1950*, Avant 1950.

CAA/AAC *Canadian Arctic Archipelago,* Archipel arctique canadien.

Cal *Calibrated dates*, Âges calibrés.

CCGS *Canadian Coast Guard Ship*.

IIS *Innuitian Ice Sheet*, Inlandsis innuitien.

IRD *Ice Rafted Debris*, débris délestés par les icebergs.

IPCC *Intergovernmental Panel on Climate Change*, groupe d'experts Intergouvernemental sur l'évaluation du climat

IRM *Isothermal Remanent Magnetization*, Aimantation isothermale rémanente.

ISMER Institut des sciences de la mer.

GIS *Greenland Ice Sheet*, Calotte glaciaire du Groenland.

Low field magnetic susceptibility, Susceptibilité magnétique mesurée à champ faible.

LF *Lithofacies*, Lithofaciès

LGM *Last Glacial Maximum*, Dernier maximum glaciaire.

LIA *Little Ice Age*, Petit âge glaciaire.

LIS *Laurentide Ice Sheet*, Inlandsis laurentidien.

MDF_{NRM} *Median Destructive Field of the Natural Remanent Magnetization*, Champs destructif médian de l'aimantation naturelle rémanente.

MSCL *Multi-Sensor Core Logger*, Banc de mesure à senseurs multiples.

MWP *Medieval Warm Period*, Période chaude médiéval.

NGCC Navire de la Garde-Côtière canadienne.

NOW *North Water Polynya*, polynie des eaux du Nord.

NRM *Natural Remanent Magnetization*, Aimantation naturelle rémanente.

RWP *Roman Warm Period*, Période chaude romaine

UQAR Université du Québec à Rimouski.

WGC *West Greenland Current*, Courant ouest groenlandais

XCT *X-ray Computed Tomographic*, Radiographie à rayons X.

XRD *X-Ray diffraction*, Diffraction à rayons X.

XFR *X-ray fluorescence*, spectrométrie de fluorescence des rayons X

INTRODUCTION GÉNÉRALE

L'introduction générale de ce mémoire présente dans un premier temps la problématique du projet de recherche. Dans un second temps, les objectifs de recherche, l'approche méthodologique et une présentation de la zone d'étude sont exposés.

Contexte scientifique et problématique

Le détroit de Nares, situé entre le nord-ouest du Groenland et le sud-est de l'île d'Ellesmere, est l'un des trois passages maritimes de l'archipel arctique canadien (AAC) reliant l'océan Arctique à la baie de Baffin (Fig. 1). Des études précédentes basées sur des données satellitaires ont mis en évidence des changements majeurs dans le volume, la masse et la décharge de glace et d'eau de fonte des glaciers et des calottes glaciaires de l'AAC et du nord de la Groenland en raison du réchauffement climatique moderne (ex. Millan *et al.*, 2017; Mortimer & Sharp 2018; Cook *et al.,* 2019; Van Wychen *et al.,* 2020, 2021; Ciracì *et al.*, 2020).

Par exemple, Cook *et al.* (2019) rapportent une rapide augmentation du retrait de 300 glaciers à terminaison marine dans l'AAC, avec une multiplication par cinq des taux de retrait entre 2000 et 2015 par rapport aux quatre décennies précédentes, principalement sous l'effet de l'augmentation de la fonte de surface des glaciers. Cette étude montre également que les patrons de retrait des glaciers à terminaison marine de l'AAC depuis 1958 ne présentent aucune corrélation avec les changements des températures océaniques de subsurface, ce qui contraste clairement avec la prédominance du forçage océanique dans la marge ouest du Groenland (Cook *et al.,* 2019). Lenaerts *et al.* (2013) suggèrent que la perte de masse des calottes glaciaires dans l'AAC au 21e siècle sera de 12 400 ±8 500 milliards de tonnes (Gt), ce qui équivaut à une élévation eustatique du niveau de la mer de 0.35 ±0.24 mm par an. Cependant, la réponse des glaciers de l'AAC et du Groenland au réchauffement climatique moderne est spatialement hétérogène (ex., les taux de retrait les plus élevés sont observés dans les petites masses de glace ; Sharp *et al.*, 2014; White & Copland 2018). De plus, il existe peu de données disponibles sur les taux de vêlage des icebergs et les flux de sédiments glaciaires à long terme (>100 ans) de ces glaciers et nous avons peu de connaissance sur les mécanismes précis (atmosphérique ou océanique) qui contrôlent les changements frontaux de ces glaciers (Cook *et al.*, 2019).

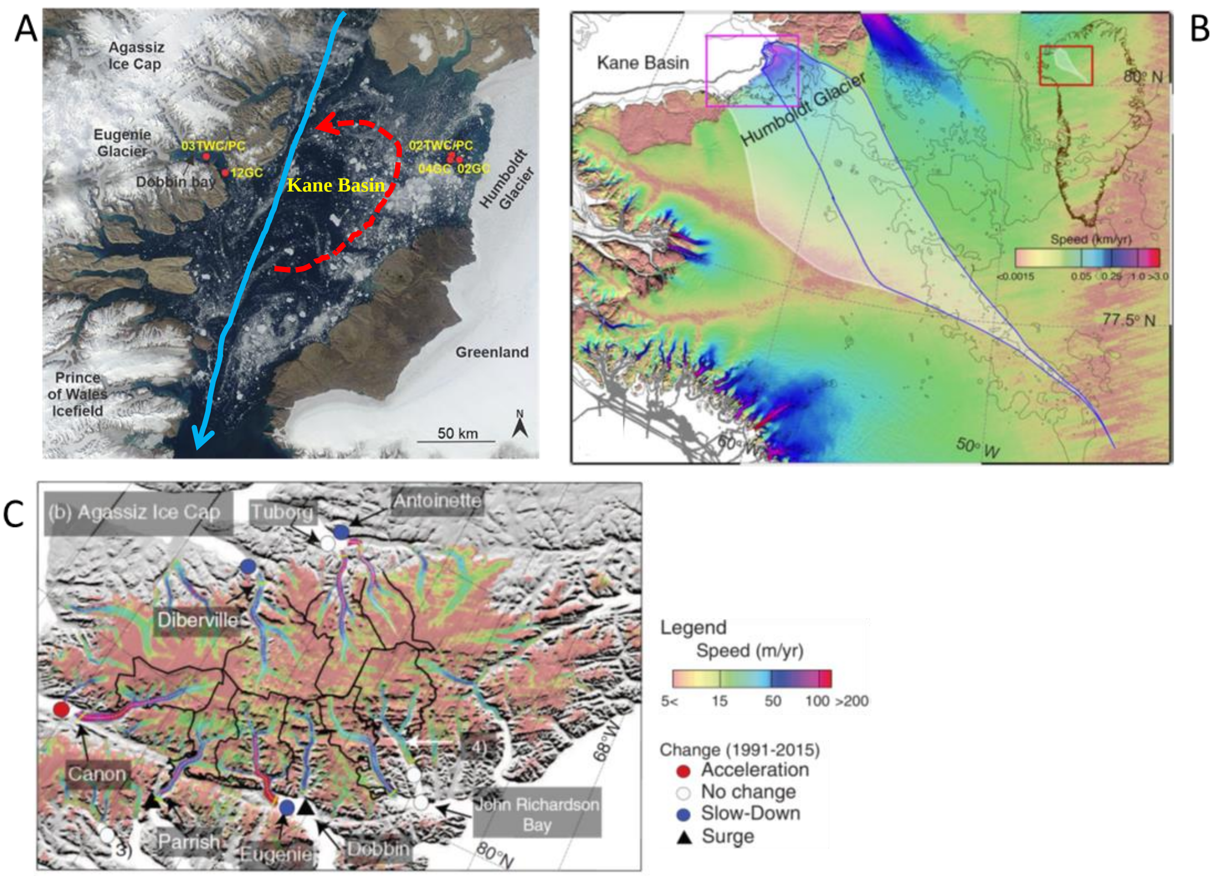

Fig. 1. Cartes de la zone d'étude. A) Image satellite MODIS du 14 août 2019 montrant un aperçu de la distribution de la glace de mer et des icebergs autour du bassin de Kane et la position des carottes étudiées (source: NASA Worldview). B) Vitesse d'écoulement moyen entre 1972 to 2018 pour le glacier Humboldt (Mouginot et al., 2019 ; Rignot et al., 2021). C) Vitesse d'écoulement moyen entre 1991 et 2015 pour la calotte glaciaire Agassiz, incluant les glaciers Eugenie et Dobbin (Millan et al., 2017). Les flèches rouges représentent les

courants de surface chauds (>2 °C) et les flèches bleues les eaux de surface arctiques (ASW) froides (<-1 °C).

La sédimentation marine à proximité des glaciers est influencée par plusieurs processus sédimentaires tels que les icebergs et les floes de glace de mer, les coulées de débris glaciaires, les panaches d'eau de fonte, les courants de turbidité et les courants de fond (ex. Syviski *et al.*, 1989; O'Cofaigh *et al.*, 2013; Andrews *et al.*, 2018; Jennings *et al.*, 2019; Caron *et al.*, 2020; Lévesque *et al.*, 2020; Fig. 2). Ces différents processus sédimentaires sont reflétés par les lithofaciès des carottes sédimentaires (ex. Jenner *et al.*, 2018; O'Regan *et al.*, 2021; Stevenard *et al.*, 2021; Rodriguez-Cuicas *et al.*, 2023). Dans ce contexte, l'étude de séquences sédimentaires marines à proximité des glaciers peut aider à mieux comprendre leur dynamique au-delà de l'enregistrement instrumental et donc de mieux comprendre le rôle du forçage atmosphérique et océanique sur ceux-ci.

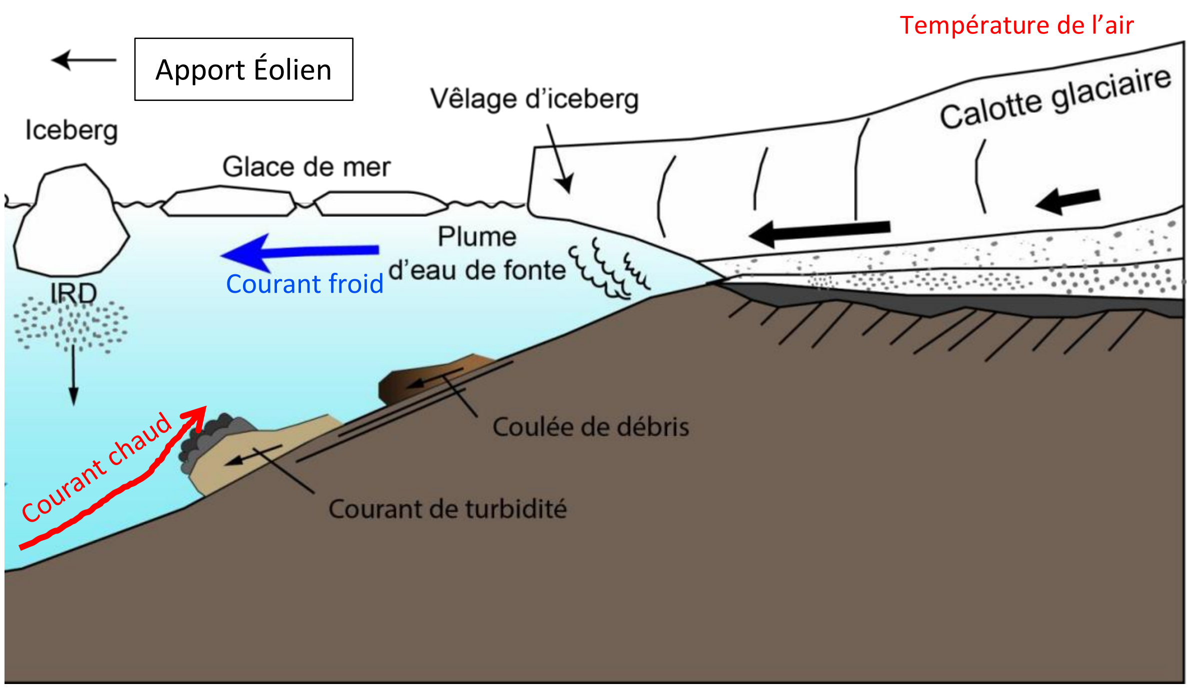

Fig. 2. Représentation de processus de transport sédimentaire associés à une marge glaciaire. Le transport du sédiment peut être liés aux courants des turbidités, icebergs, à la plume d'eau de fonte, et finalement aux courants atmosphériques et marins (inspiré de Aksu & Piper, 1987; Ó Cofaigh *et al.*, 2013).

Plusieurs études glaciologiques, sédimentologiques et paléocéanographiques dans le détroit de Nares ont documenté les phases de retraits glaciaires et d'ouverture du détroit pendant la déglaciation (ex. Dyke *et al.,* 1998; England *et al.,* 2006; Jennings *et al.,* 2011, 2019; Georgiadis *et al.*, 2018; Caron *et al.,* 2019, 2020; Stevenard *et al.,* 2021). Cependant, la dynamique sédimentaire associée à des fronts glaciaires à terminaison marine de part et d'autre du bassin de Kane au cours de l'Holocène (les 11700 dernières années) et leur lien avec l'histoire climatique régionale ont été très peu documentés par des séquences sédimentaires marines. Cette information pourrait donner des pistes pour améliorer notre compréhension sur la variabilité naturelle de ces glaciers dans le contexte du réchauffement climatique moderne.

Présentation de la zone d'étude

Le détroit de Nares est composé du nord au sud par le canal Robeson, bassin Hall, canal Kennedy, bassin Kane et du détroit de Smith (Jennings *et al.,* 2011). Ce détroit présente une profondeur de 220 m à son seuil le moins profond dans le bassin Kane et une largeur de 40 km à son point le plus étroit (Tang *et al.*, 2004). Le bassin de Kane est le bassin central du détroit de Nares avec un largeur de 120 km à son point le plus large et une profondeur moyenne de 220 m. La banquise et les icebergs sont présents continuellement dans le détroit de Nares (Münchow *et al.,* 2006).

L'est du bassin Kane est influencé par les décharges glaciaires provenant du glacier Humboldt. Ce glacier, avec un front de vêlage de près de 100 km de large, est le glacier à terminaison marine le plus large du Groenland et est l'une des principales sources d'icebergs dans le bassin de Kane (Weidick, 1995; Hillebrand *et al.*, 2022). Sa vitesse d'écoulement est très variable, avec un déplacement lent (~100 m/an) dans les eaux peu profondes (150 m) dans sa moitié sud et un déplacement plus rapide (200-600 m/an) dans les eaux plus profondes (300 m) dans sa moitié nord (Rignot *et al.*, 2021). Depuis 1992, le glacier Humboldt a perdu la plus grande superficie de glace ancrée (~200 km^2) de tous les glaciers à terminaison marine du Groenland, principalement dans la moitié nord (Wood *et al.*, 2021).

En fait, les données instrumentales ont démontré que le glacier Humboldt aurait perdu 161 Gt de masse de glace entre les années 1972 et 2019, ce qui en fait le quatrième plus grand contributeur à la perte de masse de l'inlandsis groenlandais, derrière Jakobshavn Isbræ (335 Gt; centre-ouest), Steenstrup/Dietrichson (230 Gt; nord-ouest) et Kangerlussuaq (174 Gt; est) (Mouginot *et al.,* 2019; Rignot *et al.,* 2021). Cette perte de masse a été attribué principalement au réchauffement des masses d'eau environnantes et à l'amincissement de la langue de glace située dans la moitié nord du glacier (Rignot *et al.,* 2021).

D'autre part, l'ouest du bassin Kane est influencé par les décharges glaciaires provenant de la calotte glaciaire Agassiz située sur l'île d'Ellesmere. La calotte glaciaire Agassiz (incluant les glaciers Eugenie et Dobbin) comprend un grand nombre de glaciers à terminaison marine qui représentent environ 8 844 km^2 (~40% de la superficie de la glace de la calotte; Millan *et al.,* 2017). Le taux de vêlage annuel moyen estimé pour la calotte glaciaire Agassiz entre 1999 et 2002 a était de 0.67±0.15 km^3/an, dont ~54% proviennent du glacier Eugénie (Williamson *et al.,* 2008). Ce dernier glacier a une vitesse d'écoulement annuel relativement élevé (~380-480 m/an) comparée aux autres glaciers de la calotte (e.g., ~20–180 m/an; Parrish, John Richardson Bay and Benedict glaciers; Williamson *et al.,* 2008). Entre 1999 et 2015, des mesures basées sur des images satellitaires ont révélé une décélération des vitesses d'écoulement des principaux glaciers de la calotte glaciaire Agassiz (ex. glacier Eugénie : de 300-400 m/an à < 20m/a), principalement attribuée à la fin progressive d'un cycle d'impulsion et de poussé (Van Wychen *et al.,* 2016, 2021).

Cependant, les études sur la dynamique des glaciers autour du bassin de Kane (calotte glaciaire Agassiz et Humboldt) n'ont pas permis de documenter les variations à long terme (>50 ans) dans le taux de vêlage d'icebergs et des flux de sédiments provenant des glaciers. Par conséquent, la dynamique des sédiments glaciaires à long terme dans cette région doit être mieux comprise afin de prédire avec précision le comportement futur des glaciers (Hodson *et al.,* 2013).

Circulation océanique

Le détroit de Nares est un corridor océanographique majeur pour l'exportation d'eau douce arctique vers la baie de Baffin. Dans le bassin de Kane, la circulation cyclonique favorise le mélange d'eaux froides et fraîches provenant de l'Arctique (ASW; température >-1°C, salinité <33) qui s'écoulent vers le sud dans un courant de bordure ouest le long l'Île d'Ellesmere, avec les eaux chaudes et salines provenant de l'Atlantique (courant ouest-groenlandais ou WGC; température >0°C, salinité >34) qui s'écoulent vers le nord du côté est du détroit de Smith jusqu'au front du glacier Humboldt (Tang *et al.*, 2004; Zweng & Münchow, 2006; Kalenitchenko *et al., 2019*; Rignot *et al.*, 2021). Des données de profileurs de courant à effet Doppler (ADCP) recueillis dans des mouillages déployés dans le détroit de Nares indiquent des vitesses moyennes du courant de surface (200 premiers mètres) dans le canal Kennedy de 18 à 32 cm/s (Rabe *et al.*, 2012) et de 10 à 15 cm/s dans le détroit de Smith (Melling *et al.*, 2001).

Ces mélanges d'eaux de températures et de salinités différentes dans le bassin de Kane pourraient avoir un effet sur les processus frontaux des glaciers de terminaison marine d'Eugénie, de Dobbin et de Humboldt, comme c'est le cas avec le courant ouest du Groenland (WGC), qui influence la marge ouest du Groenland (Caron *et al.*, 2018, 2020).

Géologie et sédimentation

La géologie le long du détroit de Nares est composée principalement de roches cristallines précambriennes recouvertes de carbonates de plateformes paléozoïques (Funder, 2011). Dans le bassin de Kane, les gneiss du Protérozoïque précoce qui constituent la ceinture mobile d'Inglefield affleurent dans le nord du Groenland jusqu'à la limite sud du glacier de Humboldt. Sur l'île d'Ellesmere et au nord du glacier Humboldt, une formation sédimentaire carbonatée du Paléozoïque (le bassin Franklinien) chevauche le bouclier précambrien (Hiscott *et al.*, 1989 ; MacLean *et al.*, 1990). Des roches volcaniques basiques avec des lits rouges siliciclastiques, qui constituent les roches du Supergroupe Thulé, affleurent dans le détroit de Smith sur la côte du Groenland et à l'est du champ de glace du Prince de Galles ainsi qu'au sud du glacier de Humboldt dans le bassin de Kane (Harrison *et al.*, 2011).

La sédimentation moderne du bassin de Kane est caractérisée par trois provinces principaux (Kravitz, 1976) : 1) les parties orientale, centrale et méridionale du bassin sont composés de sédiments argileux et silteux cristallins qui sont entrainés par l'eau de fonte en provenance de la terre d'Inglefield et du glacier Humboldt ; 2) l'ouest du bassin est composé de carbonates détritiques avec des débris clastiques et d'une fraction élevée de matériaux transportés par des icebergs provenant principalement de l'est de l'île d'Ellesmere ; et 3) le nord du bassin est composé de carbonates détritiques provenant de la région de Washington Land et du nord du détroit de Nares. La plupart des sédiments superficiels du fond marin du détroit de Nares sont composés de till, de limons à forte teneur en carbonates détritiques (dominés par la calcite et la dolomite détritiques) et en quartz (Andrews *et al.*, 2018 ; Caron *et al.*, 2020). Les vitesses de sédimentation déglaciaire et holocène au centre du bassin de Kane (carotte AMD14-Kane2b) varient de 220 à 20 cm/ka (Georgiadis *et al.*, 2018 ; Caron *et al.*, 2019).

Histoire de la déglaciation du détroit de Nares

Au cours du dernier maximum glaciaire (LGM; ~20 cal ka BP) et au début de l'Holocène précoce (11,7 à 10,3 cal ka BP; Jennings *et al.*, 2011, 2019), l'exportation des eaux froides et peu salées de l'Arctique vers la baie de Baffin était complètement bloquée en raison de la confluence des Inlandsis laurentidien (LIS), innuitien (IIS) et groenlandais (GIS) dans les détroits de Nares, de Jones et de Lancaster (ex. Dyke *et al.*, 2002 ; England *et al.*, 2006 ; Stokes *et al.*, 2015; Jennings *et al.*, 2011, 2019). Des études sédimentologiques et paléocéanographiques ont documenté les phases de déglaciation et d'ouverture du détroit de Nares au cours de l'holocène. L'ouverture du détroit de Smith s'est produite durant la période allant de 11,15 à 10,4 cal ka BP (Jennings *et al.*, 2019), tandis que l'ouverture du bassin de Kane et du bassin de Hall se produite à 9,0 cal ka BP (Jennings *et al.*, 2011; Georgiadis *et al.*, 2018; Caron *et al.*, 2019, 2020). Cependant, l'ouverture du détroit de Nares aux alentours de 9 cal ka BP a entraîné la liaison entre les océans Arctique et Atlantique à partir de la baie de Baffin (Jennings et al. 2011 ; St-Onge & St-Onge 2014). Le canal Kennedy représente la dernière partie de l'ouverture du détroit de Nares entre 8,5 et 8,3 cal ka BP, marquant la séparation de l'IIS et de l'inlandsis groenlandais (Jennings *et al.*, 2011, 2019; Georgiadis *et al.,* 2018; Fig. 3). Cependant, l'impact de l'ouverture du détroit de Nares et de l'établissement du flux arctique-atlantique sur le transfert de sédiments depuis les glaciers autour du bassin de Kane (ex. Eugénie-Dobbin et Humboldt) a été peu documenté par des séquences sédimentaires marines. Ces informations pourraient nous aider à mieux comprendre la variabilité naturelle de ces glaciers dans le contexte du réchauffement climatique (ex. Stevenard *et al.,* 2022).

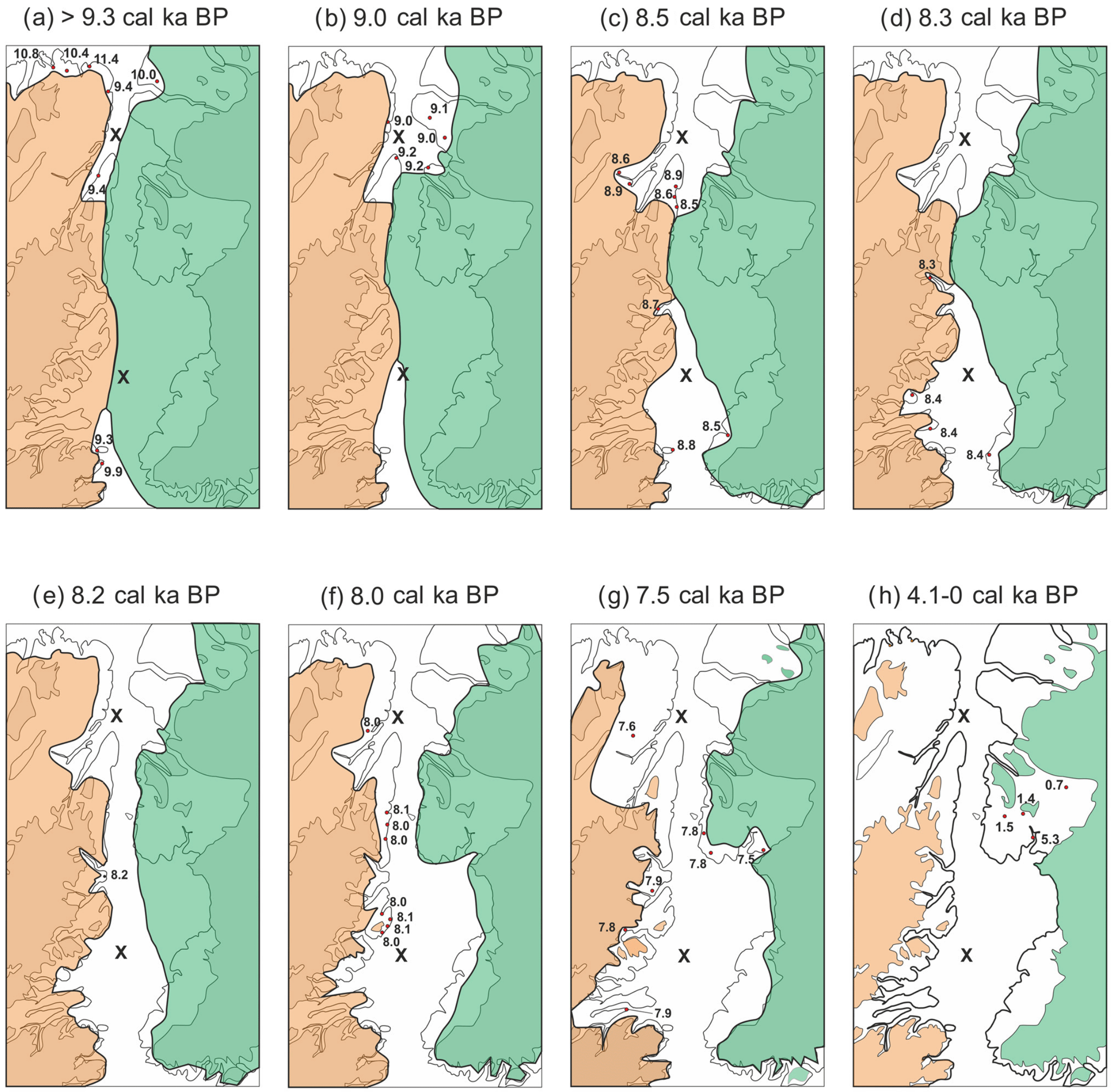

Fig. 3. Cartes schématiques du retrait des inlandsis innuitien (IIS; orange) et groenlandais (GIS; vert) dans le détroit de Nares (Georgiadis *et al.*, 2018). Les emplacements des carottes AMD14-Kane2b dans le bassin de Kane (Georgiadis *et al.*, 2018; Caron *et al.*, 2019, 2020) et HLY03-05 (Jennings *et al.*, 2011) dans le bassin de Hall sont marqués par des croix. Tous les âges ^{14}C ont été calibrés by Georgiadis *et al.* (2018) à l'aide de la courbe Marine13 (Reimer *et al.*, 2013) en appliquant une correction de l'âge du réservoir régional (ΔR) de 240 ± 55 years en Calib 7.1 (Stuiver *et al.*, 2018).

Objectifs de recherche

L'objectif général de ce travail de recherche est de caractériser et de comparer les lithofaciès des carottes sédimentaires recueillies à proximité des glaciers Humboldt et Eugenie-Dobbin afin de documenter l'évolution des environnements sédimentaires associés à ces glaciers au cours de l'Holocène. Pour ce faire, ce projet de recherche s'appuie sur deux objectifs spécifiques : **1)** déterminer les lithofaciès et reconstituer les transferts sédimentaires en provenance des glaciers Humboldt, Eugenie-Dobbin au cours de l'Holocène et **2)** documenter l'influence des changements climatiques et océanographiques holocènes sur la dynamique des glaciers Humboldt et Eugenie-Dobbin. Dans l'ensemble, cette étude fournira des informations sur la dynamique sédimentaire associée à des fronts glaciaires à terminaison marine de part et d'autre du bassin de Kane au cours de l'Holocène et sur leur lien avec l'histoire climatique régionale.

Approche méthodologique

L'échantillonnage a été réalisé au cours de l'expédition estivale d'ArcticNet de 2019 à bord du brise-glace de la Garde côtière canadienne (NGCC) Amundsen (Fig. 1; Montero-Serrano et al., 2019). Deux carottes à gravité (AMD1902-02GC et 04GC) et une à piston (AMD1902-02PC ; incluant la carotte de déclenchement — TWC) ont été prélevées dans la zone du glacier Humboldt, tandis qu'une carotte à gravité (AMD1902-12GC) et à piston (03PC/TWC) ont été échantillonnées dans la baie de Dobbin à proximité des glaciers Eugenie- Dobbin (Fig. 1).

Les profils sismiques et la bathymétrie multifaisceaux ont été utilisés pour sélectionner les sites d'échantillonnage (Figs. S1 & S2). Ces carottes offrent un bon emplacement pour documenter et comparer les décharges de sédiments glaciaires provenant des glaciers Humboldt et Eugénie-Dobbin ainsi que pour évaluer l'importance des changements récents de ces glaciers.

Les carottes à gravité (GC) et à déclenchement (TWC) ont été sous-échantillonnées à tous les 4 cm et tous les 8 cm dans les carottes à piston, pour un total de 355 échantillons. Une description visuelle a été réalisée pour l'ensemble des carottes afin de déterminer la couleur des sédiments en utilisant la charte de Munsell et d'identifier de possibles changements de faciès sédimentaires. Pendant cette description, des fragments de coquilles de mollusques ont été récupérés à différents intervalles pour la datation au radiocarbone (^{14}C). Afin de visualiser les variations de structures et de faciès sédimentaires, les carottes ont été radiographiées (GEOTEK X-ray CT System; St-Onge *et al.,* 2007), tandis que les paramètres physiques (incluant photographie à haute résolution, densité, susceptibilité magnétique et couleur) et chimiques (fluorescence X portable ou pFRX) ont été mesurés avec un GEOTEK Multi Sensor Core Logger (MSCL, St-Onge *et al.,* 2007).

Les analyses granulométriques ont été effectuées sur la fraction détritique (fraction <2 mm) à l'aide d'un granulomètre laser Malvern-Panalytical Mastersizer 3000. Avant l'analyse, les échantillons de sédiments ont été traités avec 10 mL de peroxyde d'hydrogène (H_2O_2 ; 30 % v/v) pendant au moins 72 h pour éliminer la matière organique. La défloculation des échantillons a été réalisée en ajoutant 30 mL d'une solution de Calgon (hexamétaphosphate de sodium ; 20 g L^{-1}) et en l'agitant mécaniquement pendant 12 h avant la mesure. La distribution granulométrique et les paramètres statistiques ont été calculés avec le logiciel GRADISTAT version 9.1 (Blott & Pye, 2001).

La composition minéralogique des échantillons a été analysée par diffraction des rayons X (DRX) selon la méthode développée par Eberl (2003) et en utilisant un diffractomètre Panalytical X'Pert Powder. Pour la quantification des principaux composants minéralogiques, les diffractogrammes obtenus ont été convertis en pourcentage de poids de minéraux (% en poids) en utilisant le programme powdR (Butler & Hillier, 2020). Le macro-Excel SedUnMix a été utilisé avec les données de DRX pour documenter et quantifier les variations à long terme de la provenance des sédiments (Andrews & Eberl, 2012 ; Andrews *et al.,* 2015 ; Caron *et al.,* 2020). Les sources de sédiments utilisées dans SedUnMix ont été les mêmes que celles utilisées par Andrews et al. (2018), Caron et al. (2020), Stevenard et al. (2021) et Jennings et al. (2022): 1) la ceinture mobile d'Ellesmere-Inglefield composé par quartz et feldspaths; les carbonates détritiques du courant glaciaire de Nares, qui comprennent des sédiments de la partie nord du canal Kennedy et de la région de Washington Land, dominés par calcite détritique, dolomite et muscovite; et les carbonates détritiques de l'est de l'île d'Ellesmere dominés principalement par la calcite et secondairement par la dolomite.

Finalement, les variations des traceurs détritiques a été comparées avec d'autres enregistrements paléoclimatiques situés autour du détroit de Nares (ex. température estivale modelée de la calotte glaciaire Agassiz - Buizert et al., 2018 ; données des conditions océaniques de surface reconstituée dans la carotte AMD14-Kane2b - Caron *et al.,* 2019; Georgiadis et al., 2020) afin de mieux comprendre la réponse de ces glaciers à la variabilité climatique et océanographique régionale et globale au cours de l'Holocène (ex. Stevenard *et al.,* 2021).

L'ensemble de données obtenus dans ce projet seront archivées sur le site de gestion des données paléocéanographiques et paléoclimatiques PANGEAE (https://www.pangaea.de/).

Holocene sediment lithofacies and depositional processes near the Humboldt (northwest Greenland) and Eugenie-Dobbin (Ellesmere Island) glaciers

Christian Bicera Nfundiko [1], Jean-Carlos Montero-Serrano [1], Guillaume St-Onge [1,2], Alexandre Normandeau [3]

[1] Institut des sciences de la mer (ISMER), Université du Québec à Rimouski (UQAR), Québec-Océan, Geotop, Rimouski, Québec, Canada.

[2] Canada Research chair in Marine Geology, Rimouski, Quebec, Canada.

[3] Geological Survey of Canada (Atlantic), Bedford Institute of Oceanography, Dartmouth, Nova Scotia, Canada.

1. INTRODUCTION

The Arctic has warmed four times faster than the rest of global average since 1980, this phenomenon is known as Arctic amplification (Serreze *et al.* 2006; Rantanen *et al.* 2022). This has large and unprecedented impacts on the dynamics of the Arctic cryosphere. Indeed, observational data from the last decades have shown major changes in ice acceleration, thinning, and calving from glaciers, ice caps, and ice sheets of the Canadian Arctic Archipelago (CAA) and northern Greenland due to modern climate warming (Millan *et al.* 2017; Mortimer & Sharp 2018; Cook *et al.* 2019; Van Wychen *et al.* 2020, 2021; Ciracì *et al.* 2020). For example, Cook *et al.* (2019) report a rapid increase in the retreat of 300 marine-terminating glaciers in the CAA, with a five-fold increase in retreat rates between 2000 and 2015 compared to the previous four decades, primarily driven by increased glacier surface melt. This study also shows that retreat patterns of CAA marine-terminated glaciers since 1958 do not correlate with changes in subsurface ocean temperatures, in clear contrast to the dominance of oceanic forcing along the West Greenland margin (Cook *et al.* 2019). Lenaerts *et al.* (2013) suggest that ice sheets on the CAA will loose 12.400±8.500 Gt of ice during the

21st century, which would contributed to a rise of 0.35±0.24 mm yr^{-1} in the global sea level. Future climate change projections suggest that this glacial melt will continue in the next years (Ono *et al.* 2022).

Nares Strait, located between northwestern Greenland and southeastern Ellesmere Island, is one of three marine passages in the CAA connecting the Arctic Ocean to northern Baffin Bay (Fig. 4). This area is strongly influenced by 1) ice, meltwater, and sediment discharge from outlet glaciers on eastern Ellesmere Island and the northwestern Greenland margin (O'Cofaigh et al. 2013; Dowdeswell et al. 2015) and 2) drift ice from northern Nares Strait (Tang *et al.* 2004; Georgiadis et al. 2020). The largest glaciers and ice caps surrounding Nares Strait are the Agassiz Ice Cap, Prince of Wales Icefield, and Manson Icefield on eastern Ellesmere Island, and Humboldt Glacier in northwest Greenland. The response of these glaciers and ice caps to modern climate warming is spatially heterogeneous (Sharp et al. 2014; White & Copland 2018). Furthermore, previous sedimentological and palaeoceanographic investigations in Nares Strait have documented phases of glacial retreat and opening of the Strait during deglaciation (e.g., Dyke et al. 1998; England et al. 2006; Jennings et al. 2011, 2019; Georgiadis *et al.* 2018; Caron *et al.* 2020; Stevenard et al. 2021) and changes in sea-surface conditions during the Holocene (e.g., Caron et al. 2019; Georgiadis et al. 2020; Ribeiro et al. 2021; Koerner et al. 2021; Jackson et al., 2021). However, the iceberg calving rates, sediment fluxes and sedimentary dynamics associated with marine-terminating glaciers on either side of the Kane Basin during the Holocene and their link to regional climate history have been poorly documented.

In this context, the physical, sedimentological, mineralogical and elemental geochemical properties of sediment cores collected in the vicinity of the Humboldt (northwest Greenland) and Eugenie-Dobbin (Dobbin Bay, Ellesmere Island) glaciers are used here to **1)** determine lithofacies and reconstruct glacial sediment transfer during the Holocene, **2)** document the sensitivity of these glaciers to changing climatic and oceanic conditions during the Holocene, and **3)** document changes in detrital sediment provenance and transport in Nares Strait since the last deglaciation. This study provides information about the natural variability of these glaciers in the context of modern climate warming and improves our understanding on the sediment provenance and transport pathways in Nares Strait since the last deglaciation.

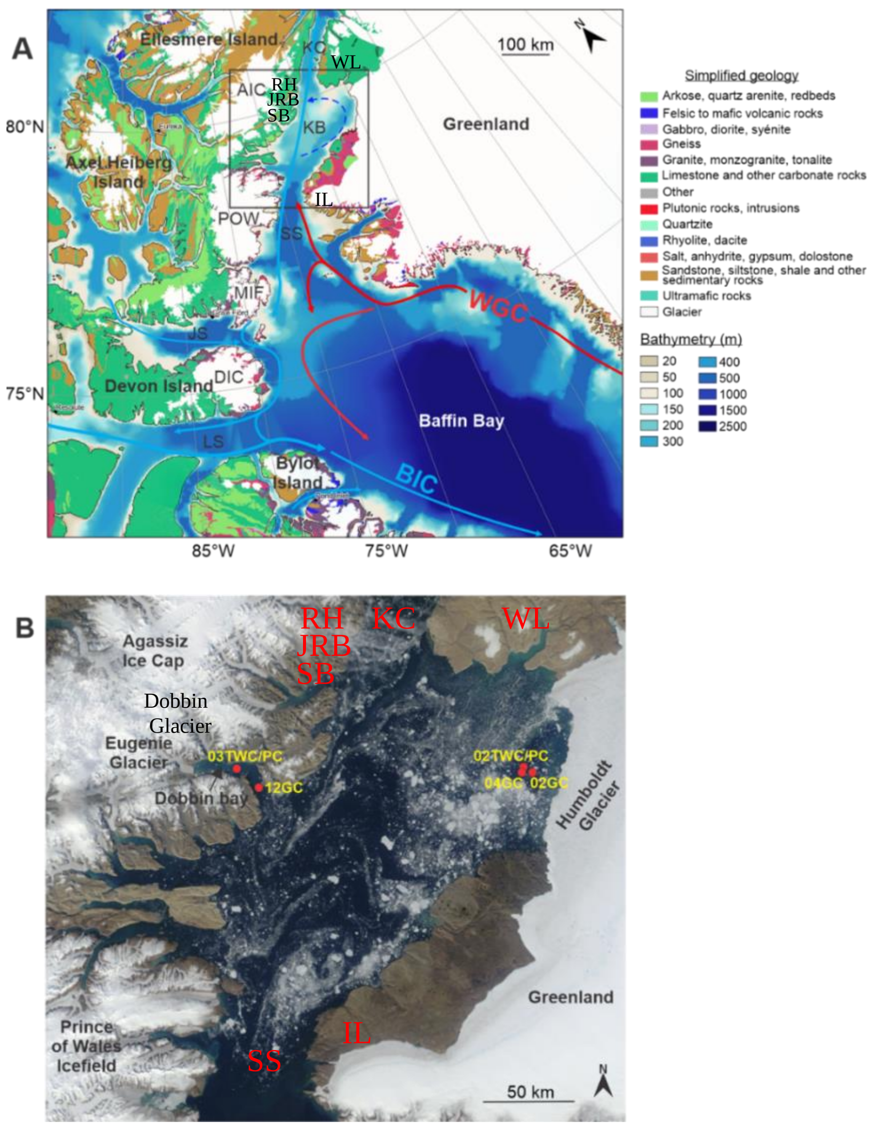

Fig. 4. Maps of the study area. A) Simplified bathymetric and geologic map of northern Baffin Bay with major surface currents. Red arrows represent warm (>2 °C) surface currents, and blue arrows represent cold (<-1 °C) Arctic surface waters (ASW). WGC = West Greenland Current; BIC = Baffin Island Current; LS = Lancaster Sound; JS = Jones Sound; SS = Smith Sound; KB = Kane Basin; KC = Kennedy Channel; MIF = Manson Icefield;

POW = Prince of Wales Icefield; DIC=Devon Ice Cap; AIC=Agassiz Ice Cap; IL=Inglefield Land; WL=Washington Land; Scoresby Bay=SB, John Richardson Bay =JRB and Readmore Harbour = RH. Modified from Brice et al. (2022) and Harrison et al. (2011). B) MODIS satellite image from August 14, 2019, showing an overview of the distribution of sea ice and icebergs around Kane Basin with the location of the sediment cores (yellow text and red dots) analyzed in this study.

2. Regional Setting

2.1. Ocean Circulation

Nares Strait is composed from North to South by the Robeson Channel, Hall Basin, Kennedy Channel, Kane Basin, and Smith Sound (Jennings et al. 2011) (Fig. 4a). It has depths varying from 200 m to 500 m. The Kane Basin in the central Nares Strait is 120 km wide at its widest point and has an average depth of 220 m (Tang et al. 2004). Nares Strait is influenced by two main ocean currents, the Arctic Surface Water (ASW) in the upper 100 to 300 m of the water column and the West Greenland Current (WGC) below, both separated by a halocline (Tang *et al.* 2004; Zweng & Münchow, 2006; Münchow et al. 2014). ASW consists of a mixture of waters from the North Pacific (entering the Arctic Ocean via the Bering Strait), river runoff and sea ice melt. While the WGC consists of a mix of the East Greenland Current (EGC; Arctic water from the Fram Strait) and the Irminger Current (IC; North Atlantic water), both of which mix south of Greenland to form the WGC (Tang *et al.* 2004). In Kane Basin, cyclonic circulation favors the mixing of cold, fresh ASW (temperature >-1°C, salinity <33) flowing southwards in a western boundary current along Ellesmere Island, with warm, saline WGC (temperature >0°C, salinity >34) flowing northwards along the eastern side of Smith Sound to the Humboldt Glacier front (Tang et al. 2004; Zweng & Münchow, 2006; Kalenitchenko et al. 2019; Rignot et al. 2021). Thus, changes in the balance between the WGC and the ASW could have an impact on the frontal processes of marine-terminating glaciers in Eugenie-Dobbin and Humboldt glaciers. Doppler current profiler (ADCP) data collected in moorings deployed in Nares Strait indicate mean surface current velocities (first

200 meters) in Kennedy Channel of 18-32 cm/s (Rabe et al. 2012) and 10-15 cm/s in Smith Sound (Melling et al. 2001).

The sea-ice cover in Nares Strait regularly transitions from a landfast state during winter when an ice arch forms across Kane Basin (this marks the boundary with the North Water Polynya; Barber et al. 1999; Kwok *et al.* 2013) to a mobile state during July–October when sea ice flows southward of the Strait. The variability in the formation of the winter landfast sea-ice cover can affect ocean circulation within Nares Strait (e.g., Münchow et al. 2007, 2011; Shroyer et al. 2015, 2017). Indeed, based on a high-resolution coupled ocean and sea-ice models and sub-sea mooring data, Shroyer et al. (2015, 2017) suggest that a collapse of the ice arch across Kane Basin may promote during the summer a westward Ekman transport of ASW and an increase in oceanic heat flux along the Greenland coast of Nares Strait, and consequently influence the mass loss of marine-terminating glaciers. Ice floes and icebergs are present continually through Nares Strait (Münchow et al. 2007).

2.2. Surrounding Geology and Sedimentation

Four major geological provinces outcrop along Nares Strait (Trettin 1991; Dawes, 2006): the Ellesmere-Inglefield mobile belt, the Thule Basin, the Fraklinian mobile belt, and the Eureka Sound Group. The Palaeoproterozoic Ellesmere-Inglefield mobile belt, outcropping on both shores of Smith Sound (southeastern Ellesmere Islands and Inglefield Land), is mainly composed of gneisses, metasedimentary rocks, and granitic intrusive rocks (crystalline shield). This Palaeoproterozoic basement is also thought to underlie the 100 km wide Humboldt Glacier (Dawes 2004; Caron et al. 2020). The Mesoproterozoic Thule Basin, cropping out on the northwestern part of Greenland coast and the eastern Prince of Wales Icefield, is composed by varicoloured sandstones and shales (including red beds) and basic volcanic rocks (Dawes 2004; Harrison et al. 2011). These rocks constitute the Thule Supergroup rocks and directly overly the shield (Dawes, 2004). The red sediments found in the Smith Sound marine sediment cores come from this supergroup, and can therefore be used as a sedimentary proxy reflecting deglaciation on both sides of Smith Sound (e.g., St-

Onge & St-Onge 2014; Jennings et al. 2019; Caron et al. 2019; 2020; Stevenard et al. 2021). The Lower Palaeozoic Franklinian Basin, out cropping out on North of Humboldt Glacier and the Ellesmere shoreline north of Smith Sound, is mainly composed of sedimentary carbonate-bearing rocks and evaporites, which overly the Precambrian Shield (Dawes 2004; Harrison et al. 2011). Finally, some rocks outcropping on the Ellesmere shores of the Kane Basin and Kennedy Channel, as well as on the Judge Daly Promontory, are composed by Paleogene sandstones, shales and lignites and are part of the Eureka Sound Group (Kerr, 1967, 1970; Harrison et al. 2011).

Marine sedimentation near glaciers is influenced by several sedimentary processes such as iceberg and sea ice rafting, glacial debris flows, meltwater plumes, turbidity currents, and bottom currents (e.g., Syviski et al. 1989; O'Cofaigh et al. 2013; Andrews et al. 2018; Jennings et al. 2019; Caron et al. 2020; Lévesque *et al.* 2020). These various sedimentary processes are reflected by the lithofacies of sedimentary cores (e.g., Jenner et al. 2018; O'Regan et al. 2021; Stevenard et al. 2021).

Modern sediments in the Kane Basin are derived from three main provinces (Kravitz, 1976): 1) the eastern, central and southern parts of the basin are composed of crystalline clayey and silty sediments that are entrained by meltwater from the Inglefield Land and Humboldt Glacier ; 2) the western part of the basin is composed of detrital carbonates with clastic debris and a high fraction of iceberg-transported material originating mainly from eastern Ellesmere Island; and 3) the northern part of the basin is composed of detrital carbonates originating from the Washington Land area and northern Nares Strait. Most Nares Strait seafloor surficial sediments are composed of till, silts with high detrital carbonate (dominated by detrital calcite and dolomite) and quartz content (Andrews et al., 2018; Caron et al., 2020). Deglacial and Holocene sedimentation rates in the central Kane Basin (core AMD14-Kane2b) range from 220 to 20 cm/ka (Georgiadis et al. 2018; Caron et al. 2019).

2.3. Deglacial–Holocene history of Nares Strait

During the LGM (~20 cal ka BP) and early Holocene (11.7 to 10.3 cal ka BP; Jennings *et al.* 2011, 2019), there was the junction of the three major ice sheets, the Greenland Ice Sheet (GIS) and Innuitian Ice Sheet (IIS) with the Laurentide Ice Sheet (LIS), which blocked passage through Nares Strait, Jones Sound and Lancaster Sound, preventing the flow of polar waters to Baffin Bay (Dyke, 2004; Dyke et al. 2002; England et al. 2006). Sedimentological and paleoceanographic studies have documented the deglaciation and opening of Nares Strait during the Holocene. The opening of Smith Strait occurs during the period from 11.15 to 10.4 cal ka BP (Jennings *et al.* 2019), while the opening of Kane Basin and Hall Basin occurs at 9.0 cal ka BP (Jennings *et al.* 2011; Georgiadis et al. 2018; Caron *et al.* 2019, 2020). However, the opening of Nares Strait around 9 cal ka BP led to the connection between the Arctic and Atlantic oceans from Baffin Bay (Jennings et al. 2011; St-Onge & St-Onge 2014). The Kennedy Channel represents the last part of the Nares Strait opening between 8.5 and 8.3 cal ka BP, marking the separation of the IIS and the GIS (Jennings *et al.* 2011, 2019; Georgiadis et al. 2018). However, the impact of the opening of Nares Strait and the establishment of the Arctic-Atlantic outflow on sediment transfer from glaciers around the Kane Basin (e.g., Eugenie-Dobbin and Humboldt) has been poorly documented by marine sedimentary sequences. This information could help to better understand the natural variability of these glaciers in the context of global warming (e.g., Stevenard *et al.* 2022).

3. MATERIALS AND METHODS

3.1. Marine sediment core

Sediment cores were recovered onboard the Canadian Coast Guard Ship (CCGS) icebreaker Amundsen during the 2019 ArcticNet summer expedition (Table 1; Fig. 4). Coring was conducted using a 9 m long piston corer (PC) and 2.15 m trigger weight corer (TWC) as well as a 3 m gravity core (GC). Cores AMD1902-02PC (piston core and companion trigger weight core) and AMD1902-02GC and AMD1902-04GC, hereafter referred to as

02PC/TWC, 02GC and 04GC, were collected near Humboldt Glacier at 750 meters between cores (Northwest Greenland). Cores AMD1902-03PC and AMD1902-12GC, hereafter referred to as 03PC and 12GC were recovered in Dobbin Bay near Eugenie-Dobbin Glaciers at 15.4 kilometers between cores (Fig. 4b). All coring sites were targeted using high-resolution seismic profiles (Figs. S1 and S2) and multibeam-bathymetry data (Montero-Serrano *et al.* 2019). Multibeam bathymetric data were collected using a Kongsberg EM302 multibeam echosounder (30 kHz) equipped with the Seafloor Information System (SIS). The data obtained were analyzed using CARIS HIPS&SIPS 11.1 software. Subsurface profiles were acquired using a CHIRP Knudsen 3260 sonar at a frequency of 3.5 kHz.

Table 1. Location of the sampling sites, water depth, location and length of the cores used in this study.

Core (AMD1902-)	Latitude (°N)	Longitude (°W)	Water depth (m)	Location	Length (cm)
02TWC/PC	79.51553	-65.76922	379	Humboldt Glacier	29/551
02GC	79.50713	-65.65826	299	Humboldt Glacier	146
04GC	79.50946	-65.78536	352	Humboldt Glacier	262
03TWC/PC	79.78564	-73.66978	215	Dobbin Bay	142/558
12GC	79.69218	-73.09499	246	Dobbin Bay	229

3.2. Laboratory analyses

3.2.1. Multi-Sensor Core Logger Analyses (physical and chemical properties)

Prior to core splitting, wet bulk density (determined from gamma ray attenuation) and low field volumetric magnetic susceptibility (k_{LF}; loop sensor) were measured at 1 cm intervals using a GEOTEK Multi-Sensor Core Logger (MSCL, St-Onge *et al.* 2007). Next, all cores were split, described, and digitally photographed. The k_{LF} (point sensor), diffuse spectral reflectance and chemical composition (Si, Al, K, Ca, Ti, Fe, Mn, Rb, Sr, Zr) by portable X-ray fluorescence (pXRF) were then measured on sediment cores using a GEOTEK MSCL system at 1 cm intervals (e.g., St-Onge et al. 2007). The reflectance was obtained by using a hand-held Minolta CM-2600d spectrophotometer coupled to the MSCL, and the sediment color is expressed according to the L*, a* and b* color space of the International Commission of Light (St-Onge et al. 2007; Debret et al. 2011). Only the L* and a* indexes are used in this study. L* is a black-to-white scale (0–100) and a* is a green–red scale (-60 to +60). The pXRF scans were made using an energy-dispersive Olympus Innov-X DELTA portable X-ray fluorescence analyzer integrated with the MSCL and equipped with a 40 kV rhodium anode X-ray tube. pXRF analysis was conducted using the two beams (40 and 10 kV) GeoChem mode with a 60-second exposure time per beam. To visualize the variations of sedimentary structures and facies, all core sections were X-radiographed using a GEOTEK X-ray CT system (e.g., St-Onge et al. 2007).

3.2.2. Grain-size

Grain-size analyses (<2 mm fraction) were carried out using a Malvern Panalytical Mastersizer 3000 laser diffractometer. Prior to the analyses, the sediment samples were treated with 10 mL of hydrogen peroxide (H_2O_2; 30% v/v) for at least 72 h to remove organic matter. The samples were deflocculated by adding 30 mL of a Calgon solution (sodium hexametaphosphate; 20 g L^{-1}) and disaggregated using an in-house rotator for 12 hours prior to measurement. The grain size distribution and statistical parameters (e.g., D90) were calculated with the GRADISTAT software version 9.1 (Blott & Pye, 2001). Cores 02GC, 04GC, and 12GC were evenly sampled at a downcore resolution of on 1-cm-wide sections taken at 4 cm intervals, whereas cores 02PC and 03PC were sampled every 8 cm (samples were 1 cm wide), for a total of 355 samples.

3.2.3. Quantitative X-ray diffraction mineralogy

Quantitative X-ray diffraction mineralogy (qXRD) of the <2 mm sediment fraction was studied according to the method developed by Eberl (2003). This method has been used successfully in other Quaternary glacial marine studies that address sediment mineralogy in the Arctic (e.g., Andrews & Eberl 2011; Andrews et al. 2018; Deschamps et al. 2018; Andrews 2019; Caron *et al.* 2020; Stevenard et al. 2021). For this, 1 g of dry sediment sample (<2 mm) was spiked with 0.25 g of corundum and then ground in a McCrone micronizing mill using 5 mL of ethanol. The slurry was dried in a fume hood overnight and then slightly homogenized with an agate mortar. Next, to prevent the possible agglomeration of finer particles, 0.5 mL of vertrel was added to the mixture. The powder sample was then sieved (<300 µm), backloaded into the holders and analyzed on a PANalytical X'Pert Powder diffractometer. Samples were scanned from 5° to 65° two theta in steps of 0.02° two theta, with a counting time of 2 seconds per step. The sediment XRD scans were converted into mineral weight percentage (wt%) using the powdR software (Butler and Hillier, 2020). This program uses a library of previously measured pure phase diffractograms (Eberl, 2003) and their reference intensity ratios (Hillier, 2000) to model the measured spectrum as the sum of these pure phases. This fitting method allows quantification of the mineralogy in a sample with an average absolute bias of 0.6% for non-clay minerals, 2% for clay minerals and 5% for amorphous phases (Butler & Hillier, 2020). The calculated total mineral wt% was normalized to a sum of 100%. The principal minerals that were analyzed by this method are amphibolite (Am), amorphous silica (A. silica), biotite (Bt), calcite (Cal), chlorite (Chl), dolomite (Dol), Fe-bearing (Fe-b; magnetite, hematite), illite (Ill, including muscovite), K-feldspar (Kfs), kaolinite (Kln), plagioclase (Pl), pyroxene (Px), quartz (Qz), smectite (Sme), and vermiculite (Vm).

3.2.4. Radiocarbon and palaeomagnetic analyses

The chronology of cores 03PC and 12GC was constrained by eleven accelerator mass spectrometry (AMS) radiocarbon (^{14}C) ages (Table 2). Ten samples were measured on well-preserved marine shell fragments (mainly *Astarte borealis*), while one sample was measured on mixed benthic and planktic foraminiferal species. The chronology of core 02PC was determined by combining ^{14}C dating with paleomagnetic data. In core 02PC, two ^{14}C ages were obtained from mixed benthic and planktic foraminiferal species. Very few foraminifera (<0.01 mg) were recovered in core 04GC and from the last 200 cm of the core 02PC, which was not enough to perform AMS analysis. This low recoverable amount is related to the poor preservation of foraminifera due to calcium carbonate dissolution in bottom waters of the Arctic (e.g., Aksu 1983; de Vernal et al. 1992; Azetsu-Scott et al. 2010). Therefore, a combination of dating techniques, including AMS ^{14}C and paleomagnetic analysis, were used to produce a reliable age model for cores 02PC and 04GC. AMS ^{14}C measurements were performed with a MICADAS (MIni CArbon Dating System) at the André E. Lalonde AMS Laboratory at the University of Ottawa (Canada) and the Alfred Wegener Institute Helmholtz Centre for Polar and Marine Research (Bremerhaven, Germany).

Paleomagnetic data in 02PC and 04GC were acquired at 1-cm intervals on u-channel (u-shaped plastic liners 2x2 cm in cross section and up to 1.5 m in length) samples using a 2G Enterprises u-channel cryogenic magnetometer model 755 SRM and a pulse magnetizer for the induction of isothermal remanent magnetizations (IRMs). Due to the finite spatial resolution of the magnetometer pickup coils, each measurement integrates a stratigraphic interval of 7-8 cm (Philippe *et al.* 2018). To reduce this edge effects, the data points from the upper and lower 4 cm of each u-channel were excluded (Weeks et al., 1993). The natural remanent magnetization (NRM) was measured using alternating field (AF) demagnetization steps from 0 to 80 mT at 5-mT increments. The inclination of the characteristic remanent magnetization (ChRM) was computed by principal component analysis (PCA; Kirschvink 1980) using AF demagnetization steps from 15 to 50 mT within the Excel macro developed by Mazaud (2005). This computation also provides information on the maximum angular deviation (MAD; an indicator of the quality of the palaeomagnetic data) and the median destructive field (MDF). MDF indicates the demagnetizing field required to halve the initial magnetic remanence. MDF is a marker of magnetic mineralogy, reflecting the average coercivity of the magnetic grain assemblage and resulting from both mineralogy and grain size (e.g., Stoner & St-Onge, 2007). MAD values lower than 5° indicate high-quality data (Stoner and St-Onge 2007).

3.2.5. Age modelling

Prior to the construction of age-depth models, the correlation of the a* profiles of 02PC/04GC and the Ca/K profiles of 03TWC/PC was carried out to estimate the absence and deformation of sediments at the tops of the piston cores (Fig. S3). These correlations suggest that: i) approximately 2 cm and 8 cm of sediments at the top of cores 02PC and 03PC, respectively, were lost during piston coring; and ii) the uppermost parts of cores 02PC and 03PC show deformations at approximately 35 cm and 32 cm, respectively, which is related to the cumulative action of compaction and stretching during piston coring (Fig. S3). Therefore, the depth of cores 02PC and 03PC were adjusted accordingly. In addition, since the gravity corer (maximum recovery length of ~2.80 m) is designed to recover a relatively less undisturbed sample of the sediment–water interface than the piston corer, cores 04GC/02PC were combined into a composite sequence (hereafter referred to as 02CS) based on the correlation of the a* profiles (Fig. S3). Indeed, the upper 211 cm of core 02CS corresponds to core 04GC, and the rest of the sequence corresponds to core 02PC (211 to 631 cm). The depths of this composite sequence were adjusted. The age-depth models of cores 02CS and 03PC were generated using the corrected depths. The R package ‘rbacon’ version 2.5.7 (Blaauw & Christen 2011) was used to derive the best age-depth model of the cores. This program allows the estimation of the best fit or weighted mean age for each depth with a 95% confidence interval using a Bayesian approach. The conventional ^{14}C ages in this study were corrected using the Marine20 calibration curve (Heaton et al. 2020) and a regional marine reservoir age correction (ΔR) of 188 ± 91 years, as suggested by Pieńkowski et al. (2022) for

NW Canadian Arctic Archipelago (including Nares Strait). We assumed a constant ΔR through the Lateglacial and Holocene period. We recognize that this assumption introduces unquantified uncertainty in the age-depth models (e.g., Butzin et al. 2017).

Table 2. Accelerator mass spectrometry (AMS) radiocarbon dates and calibrations for cores 12GC, 03PC and 02PC. * Indicate data that were not used in the age model.

Lab ID	Core	Depth (cm)	Corrected Depth (cm)	Material	^{14}C (a BP)	±	ΔR = 188 ± 91	
							Median (cal a BP)	Range 2σ
UOC-20699	12GC	1		Shell fragment	124	11	modern	
UOC-20700	12GC	86.5		Shell fragment	4143	14	3770	3491 - 4058
UOC-20701	12GC	114		Shell fragment	8260	18	8371*	8129 - 8621
AWI-10211.1.1	12GC	139		Mixed benthic and planktic foraminifera	7975	84	8074	7791 - 8355
UOC-20702	03PC	0.5	19.5	Shell fragment	423	11	modern	
UOC-20703	03PC	107	166	Shell fragment	3348	13	2804	2523 - 3070
UOC-20704	03PC	239.5	298.5	Shell fragment	4225	14	3880	3583 - 4160
UOC-20705	03PC	290.5	349.5	Shell fragment	4613	14	4393	4096 - 4692
UOC-20706	03PC	380	439	Shell fragment	5088	15	5004	4752 - 529
UOC-20708	03PC	410.5	469	Shell fragment	5388	15	5368	5076 - 5592
UOC-20707	03PC	447	506	Shell fragment	5571	16	5560	5312 - 5811
AWI-10213.1.1	02PC	220	316	Mixed benthic and planktic foraminifera	7574	79	7671	7421 - 7930
AWI-10212.1.1	02PC	460	556	Mixed benthic and planktic foraminifera	11970	219	13112	12642 - 13618

3.2.6. Sediment sources and unmixing model

Based on recent sediment provenance work conducted in Nares Strait and northern Baffin Bay (e.g., Andrews et al. 2014, 2018; Andrews 2019; Jennings et al. 2019; 2022; Caron et al. 2020; Stevenard et al. 2022), we estimate that Late Quaternary sediments near the Humboldt (northwest Greenland) and Eugenie-Dobbin (Ellesmere Island) glaciers are derived from the following source areas: Ellesmere- Inglefield mobile belt dominated by quartz and feldspars (Caron et al. 2020); detrital carbonates from Nares Ice Stream which include sediments from northern part of the Kennedy Channel and Washington Land region- dominated by detrital calcite, dolomite and muscovite (Andrews et al. 2018; Caron et al. 2020; Jennings et al. 2022); and detrital carbonates from eastern Ellesmere Island dominated by mainly by calcite and secondary by dolomite (Stevenard et al. 2022). A linear discriminant analysis was performed with the potential sediment sources to demonstrate the different mineralogical compositions of these sources. Prior to discriminant analysis, a log-centered (clr) transform was applied to the dataset (Aitchison, 1990). This analysis was conducted with R software using the packages adegenet (Jombart, 2008) and compositions (van den Boogaart & Tolosana-Delgado, 2008). Then, we used the nonlinear unmixing Excel macro SedUnMix (version 2014-10-08; Andrews & Eberl 2012; Andrews et al. 2015) with the three sources described above to gain a quantitative understanding of the downcore changes in bulk sediment provenance. We ran SedUnMix on the normalized (100%) data for the 12 key minerals (Qz, Kfs, Pl, Cal, Dol, Bt+Chl, Ill) that represented more than 80 % of the overall mineral concentration in the sediment samples.

4. RESULTS AND INTEPRETATIONS

4.1. Chronology

Composite sequence 02CS (cores 02PC and 04GC). – Paleomagnetic chronological markers were obtained by comparing the inclination profiles for cores 02PC and 04GC versus depth to other regional palaeomagnetic records (AMD14-KANE2B from Caron *et al.* 2019; Peterman PSV stack from Reilly et al. 2019; and Greenland-Iceland PSV composite from Stoner *et al.* 2013). Based on similar shifts in the Earth's magnetic field behavior in the different records, 8 chronostratigraphic markers (tie points) were determined (Fig. 5, Fig. S4, Table 3). These tie points were then used in the construction of an age-depth model. The age-depth model indicates that the composite sequence 02CS spans the last 14 cal ka BP (Fig. 6A), and the calculated sedimentation rates range from ~42-53 cm ka^{-1} (631-54 cm depth) and ~28 cm ka^{-1} (top 54 cm depth).

Cores 03PC and 12GC. –The age-depth model indicates that core 03PC spans the last 6720 cal ka BP, and the calculated sedimentation rates range from ~111 cm ka^{-1} (502-352 cm depth; ~6.8 to 4.8 cal ka BP), ~100 cm ka^{-1} (352-167cm depth; ~4.8 to 3.1 cal ka BP) to 63 cm ka^{-1} (top 167 cm; 3.1 cal ka BP to present) (Fig. 6B). In core 12GC, we rejected one dated shell fragment at 114 cm depth, as it is older (8371 cal a BP) than the date of the bottom of the core (8074 cal ka BP; mixed benthic and planktonic foraminifera) and, therefore, is most probably remobilized. Core 12GC spans the last 8000 cal a BP, and the calculated sedimentation rate ranges from ~13 cm ka^{-1} (140-85 cm depth; 8.0 to 3.8 cal ka BP) and ~23 cm ka^{-1} (top 85 cm depth; 3.8 cal ka BP to present) (Fig. 6C). The low sedimentation rates in core 12GC compared to core 03PC suggest that most of the sediments at the Dobbin Bay entrance are transported out to the western Kane Basin by surface currents.

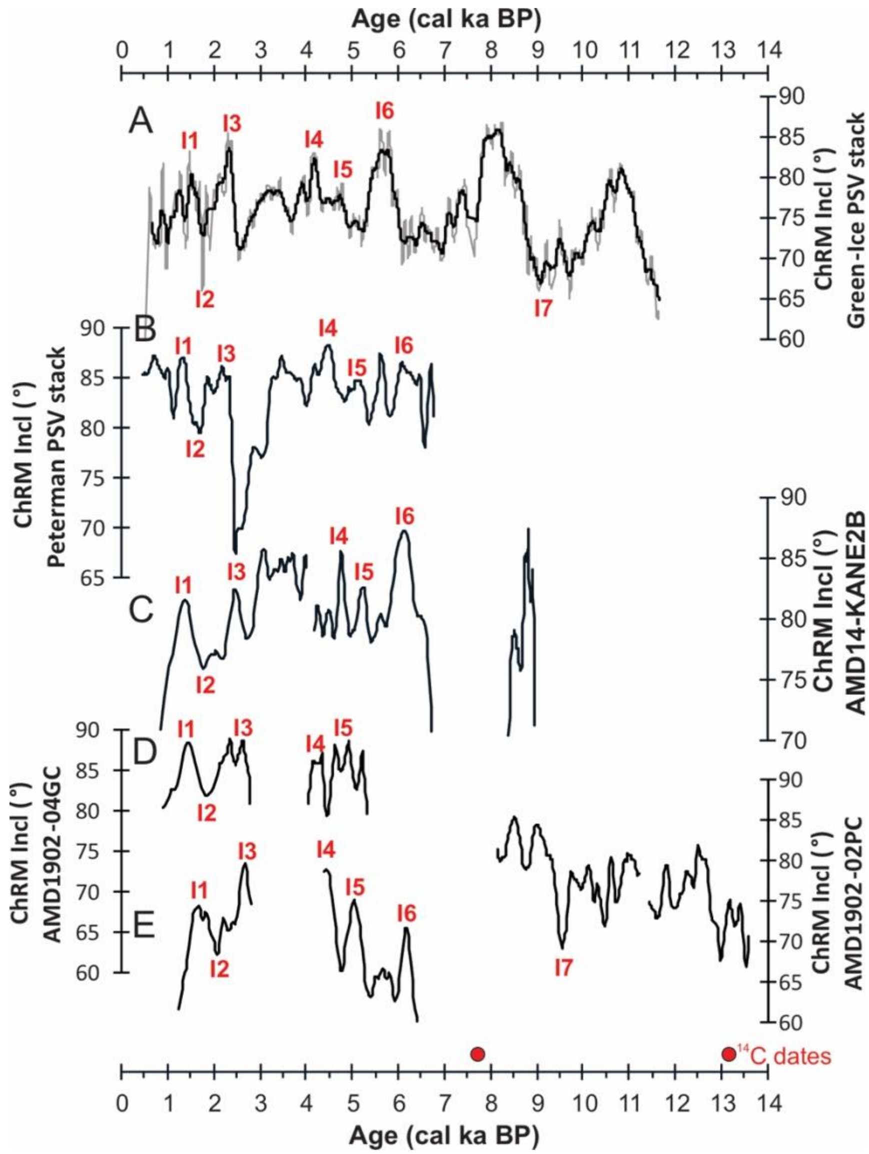

Fig. 5. Comparison of the inclination values from sediment cores 02PC (E) and 04GC (D) compared to (A, C) Green-Ice record from Stoner *et al.* (2013), Peterman PSV stack from Reilly *et al.* (2019), and core AMD14-KANE2B from Caron *et al.* (2019). Breaks in the inclination data of cores 02PC and 04GC are unreliable intervals for paleomagnetic reconstruction (see Fig. S4 for details).

Table 3. Paleomagnetic chronostratigraphical markers (tie points) based on the correlation between the 02PC and 04GC cores presented in this study with other paleomagnetic records (AMD14-KANE2B from Caron *et al.* 2019; Peterman PSV stack from Reilly *et al.* 2019; and Greenland-Iceland PSV composite from Stoner *et al.* 2013).

Tie-points	**Depth (cm)**			**Age (cal a BP)**				
	02PC	04GC	02CS	AMD14-KANE2B	Peterman	GREEN-ICE	Median age	2σ
I1	18	36	40	1400	1400	1500	1400	89
I2	32	44	48	1780	1710	1760	1760	53
I3	52	76	80	2450	2200	2340	2340	173
I4	113	180	184	4790	4500	4170	4500	422
I5	132	209	213	5255	5200	4800	5200	380
I6	170		266	6100	6100	5820	6100	249
I7	308		404			9090	9090	

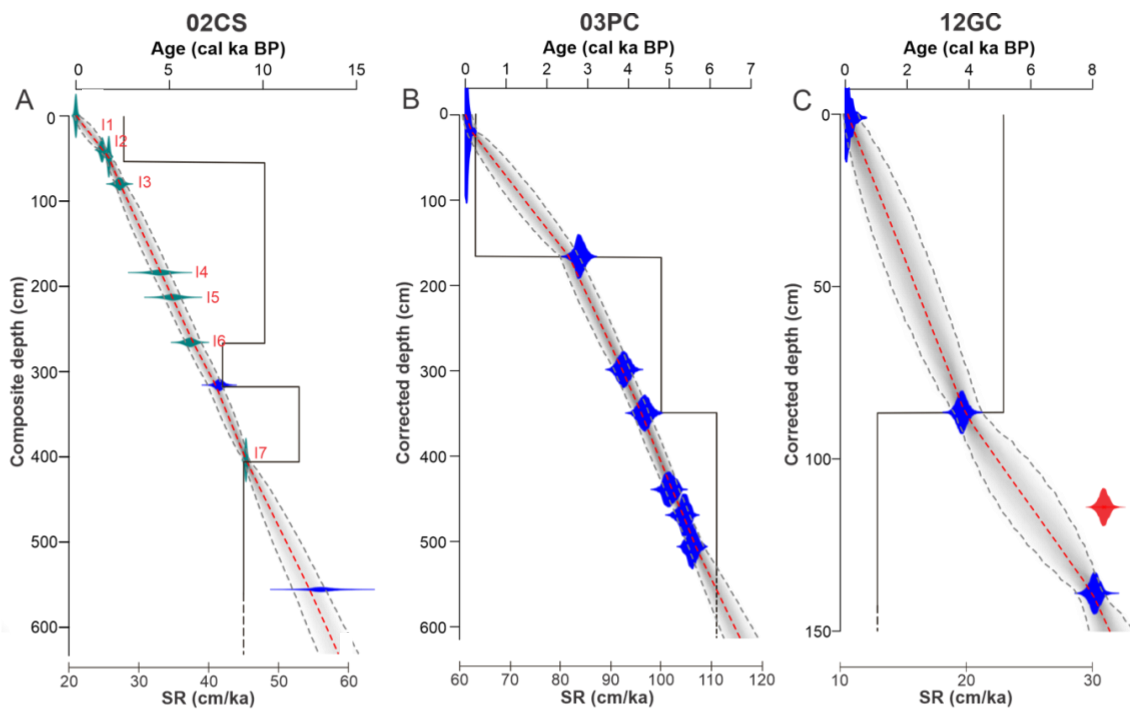

Fig. 6. Bayesian age model and sedimentation rates (SR) for cores 02CS, 03PC and 12GC. The red dashed line shows the best age model, and the gray shading represents the chronological uncertainties (95% confidence interval). Changes in sedimentation rate (SR) are represented by the black line.

4.2. General grain size, mineralogical and elemental geochemical characteristics

The grain size distributions of cores near the Humboldt (02PC, 04GC, 02GC) and Eugenie-Dobbin (03PC and 12GC) glaciers indicate a composition that is generally dominated by silts and clays, with some intervals composed of medium to coarse sand (Fig. 7). The D90 values show that these coarse-grained intervals are characterized by values of up to 25 µm and 75 µm in cores 03PC-12GC and to 200 µm and 700 µm in cores 02PC-02GC-04GC, respectively (Fig. 7). IRD are most abundant in core 02PC, with the highest concentrations in the interval between 0 and 58 cm, while core 03PC and 12GC shows low IRD.

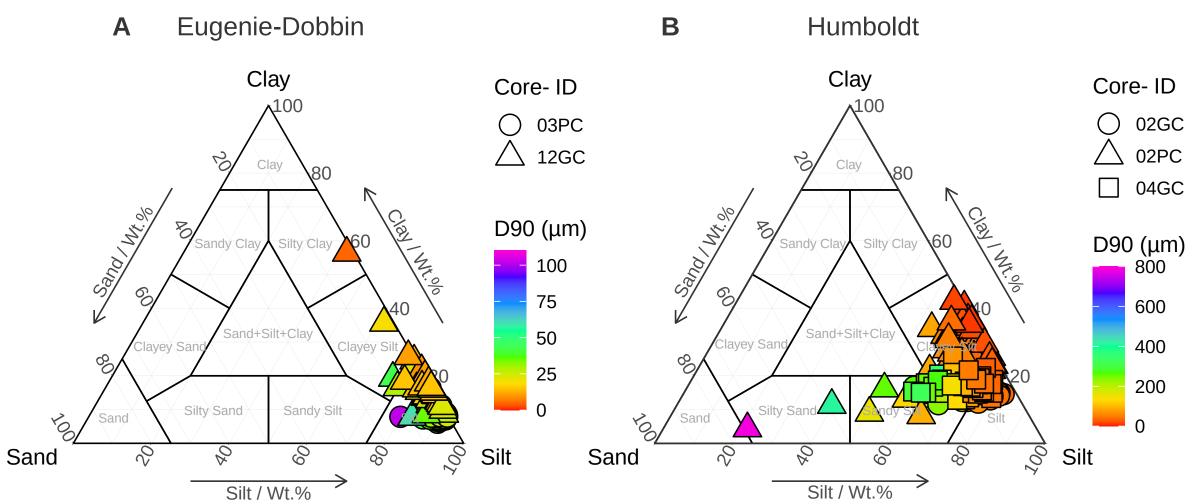

Fig. 7. Ternary diagram showing Shepard's sediment classification (Shepard, 1954) of cores collected near the Eugenie-Dobbin (A) and Humboldt (B) Glaciers.

All raw pXRF and qXRD vertical profiles are presented in the Annexes (Figs. S4 to S10). The boxplot of qXRD and pXRF data from all cores are shown in Fig. 8. Sediment cores from Eugenie-Dobbin are dominated by Cal (~18-35%), Dol (~11-22%), Pl (~3-55%), Qz (~13-17%), Bt+Chl (~6-16%), Ill (~12-27%) and by lower proportions of Kfs (~3-6%), Kln (~0-3%) and Vm (~0-3%). While, sediment cores near Humboldt Glacier are dominated by Pl (~18-29%), Qz (~13-22%), Kfs (~14-19%), Bt+Chl (~8-16%), Ill (~5-16%) and by lower proportions of Vm (~3-7%), Kln (~1-5%), Am (~1-5 wt%), Dol (~1-5%), Sme (~0-5 %) and Px (~0-2%).

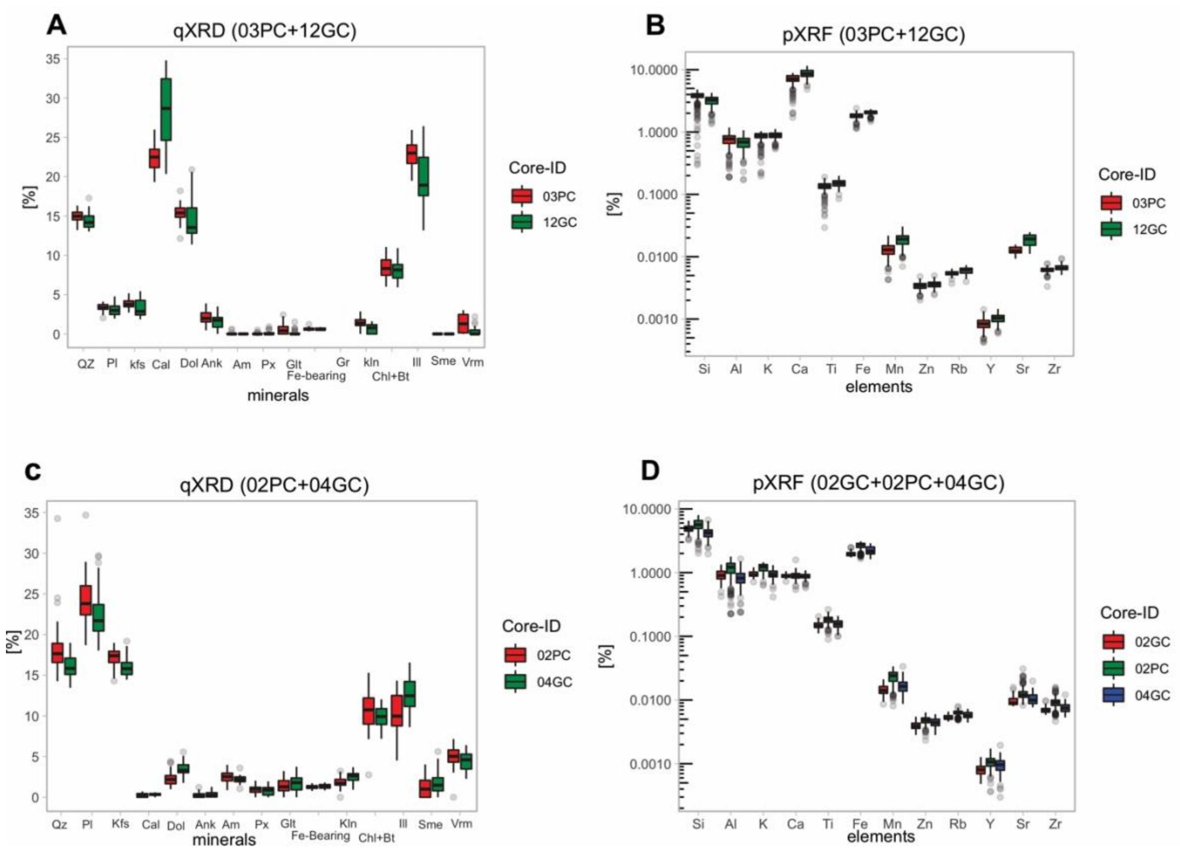

Fig. 8. Mineralogical and geochemical composition of sediment cores collected near the Eugenie-Dobbin and Humboldt Glaciers. (A, C) Boxplots of the qXRD data of cores (%); (B-D) boxplots of the pXRF data (%) of the cores. Note that 1) The box encloses 50% of the samples with the line being the median and 2) the relative intensities obtained with the of pXRF sensor were converted to percentage (1%=10000 ppm) for better visualization.

Furthermore, the major element compositions of sediment cores from Eugenie-Dobbin are dominated by Ca (~1-2 wt. %), Si (~1-5 wt.%), Fe (~0.2-0.1 wt.%), K, Al, Ti, while the minor and trace elements are dominated by Mn (49-267 mg kg^{-1}), Sr (93 -247 mg kg^{-1}), Zr (33-94 mg kg^{-1}), Rb (37-70 mg kg^{-1}), Zn (20-46 mg kg^{-1}) and Y (4-13 mg kg^{-1}).

Near the Humboldt Glacier, sediment cores are dominated by Si (~2-8 wt.%), Fe (~2-3 wt.%), Al (~0.4-2 wt.%), K, Ca, Ti, while the minor and trace elements are dominated by Mn (81-

308 mg kg^{-1}), Sr (77-159 mg kg^{-1}), Zr (46 -130 mg kg^{-1}), Rb (46-79 mg kg^{-1}), Zn (29-64 mg kg^{-1}) and Y (6-17 mg kg^{-1}) (Fig. 8).

The pXRF data from sediment cores recovered near Eugenie-Dobbin and Humboltd Glaciers indicate elevated Si, Al, Fe, and Ca, which may be related to elevated concentrations of Qz, Pl+Kfs, Fe-rich clays (Bt + Chl), and Cal + Dol.

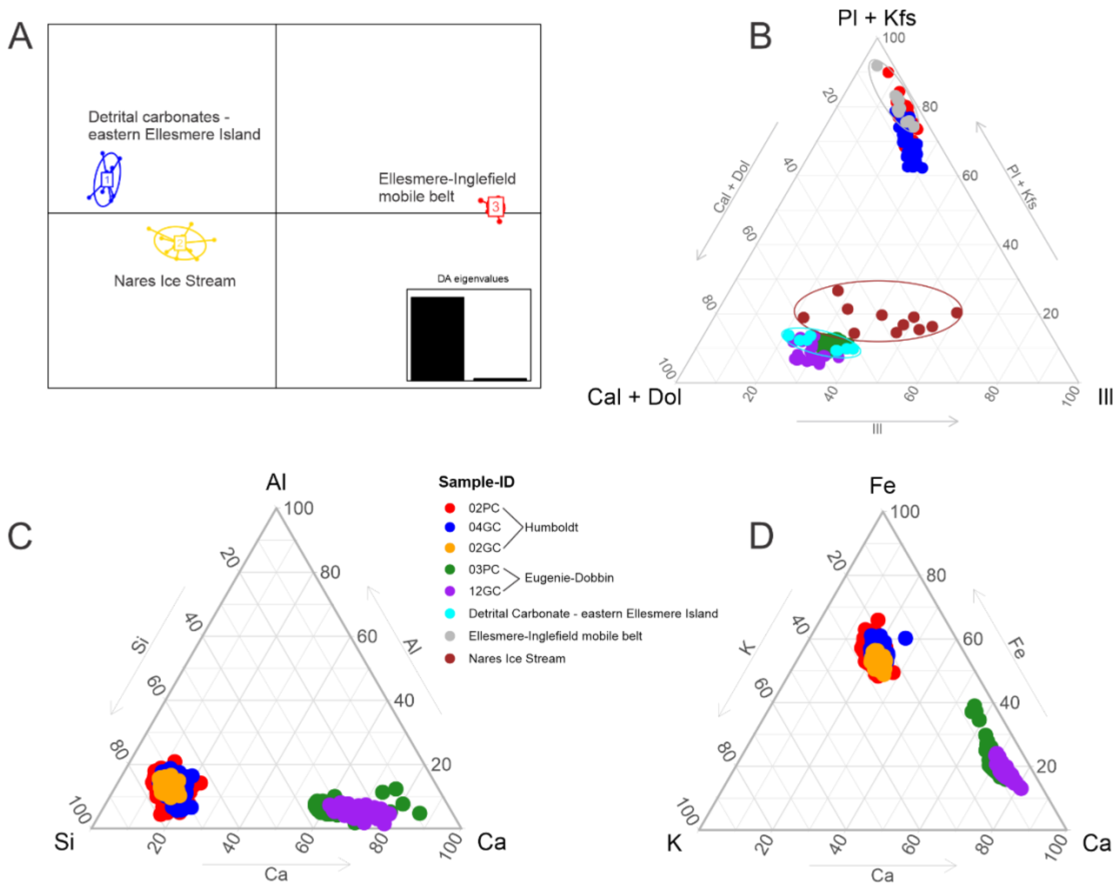

Fig. 9. (A) Linear discriminant analysis of the three sedimentary sources used in this study (Ellesmere- Inglefield mobile belt, Nares Ice Stream-, and detrital carbonates from eastern Ellesmere Island). (B) Total feldspar (Pl+Kfs)–carbonates (Cal+Dol)–Illite (Ill) ternary plots showing the overall composition of the sediment from the five cores and the three sources of sediments discussed in this study. (C-D) Al-Si-Ca and Fe-K-Ca ternary plots showing the overall composition of the sediment from the five cores.

The linear discriminant analysis and ternary plot Cal+Dol − Pl+Kfs − Ill show that the three potential sediment sources used in this study (i.e., Ellesmere-Inglefield mobile belt, Nares Ice Stream, and detrital carbonates from eastern Ellesmere Island) have mineral signatures that allow a reasonable degree of sediment discrimination (Table S1). The Ellesmere-Inglefield mobile belt sources are rich in Pl and Kfs, the sediments from Nares Ice Stream and from eastern part of Ellesmere Island are enriched in Cal and Dol. These results validate the use of these sources in the SedUnMix software. In addition, sediment cores near the Eugenie Glacier are characterized by higher detrital carbonates (mainly Cal) and Ca contents, while sediment cores near the Humboldt Glacier are rich in Pl and Kfs, Si and Fe (Fig. 9 C-D). Overall, these mineralogical and geochemical results are consistent with those reported for surface and core sediments from Nares Strait, Kane Basin, and southern part of Ellesmere Island (Andrews et al. 2018; Andrews, 2019; Caron et al. 2020; Stevenard et al. 2021).

Based on these results, we selected for the Eugenie-Dobbin area the ratios Ill+Chl+Bt/Pl+Kfs and Cal/Pl+Kfs to trace changes in clay minerals and detrital carbonate contents derived from Lower Paleozoic Franklinian basin rocks, while for the Humboldt area we selected the ratio Kln+Ill/Pl+Kfs to trace changes from the Palaeoproterozoic Ellesmere-Inglefield mobile belt sources (rich in Pl) and the ratio Dol/Pl+Kfs to trace changes in the detrital carbonate content from rocks in the northern part of the Kennedy Channel and southern Washington Land. Additionally, the Ca/K ratio was used to represent variations in terrigenous sediment delivery based on the abundance of Ca in plagioclase facies and detrital carbonates and K in clay minerals (e.g., Adgebie et al. 2003; Croudace & Rothwell 2015). The Zr/Rb ratio was used as a semiquantitative grain size indicator (von Eynatten et al. 2012; Croudace & Rothwell 2015; Wu et al. 2020) with a better vertical resolution than discrete grain size analysis. In this case, Zr is associated with coarse weathering-resistant mineral facies, and Rb is linked with fine-grained clay minerals.

4.3. Description and interpretation of lithofacies

Lithofacies (LF) were determined based on visual core descriptions, high-resolution core photography, X-CT scan images, physical properties (i.e., wet bulk density, k_{LF}, color) and grain size (D90, IRD content), qXRD and pXRF data (Table 4, Figs. 10-18). In view of these observations, three different lithofacies were identify and correlated between different cores near the Eugenie-Dobbin and Humboldt glaciers, respectively. These LFs, labeled 1-3 from base to top of the sediment cores, are described and interpreted below according to core depths.

Table 4. Summary of Humboldt and Eugenie-Dobbin lithofacies associated with sedimentary features and depositional processes.

Core	Lithfacies (LF)	X-ray	Image	Facies	Colour	Sedimentary structures	D90 (µm)	Depositional processes
Humboltd	LFH3	5cm 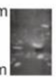 20cm		-Sandy mud with moderate bioturbation - ice-rafted debris(IRD) increase	5YR 5/3 Reddish brown	Moderately bioturbated Dispersed IRD	78	Glacier growth Landward retreat of the ice front -Meltwater plume -Increased iceberg calving
	LFH2	121cm  140cm		-Sandy mud with occasional intervals of medium sand -More IRD	5YR 6/4 Light reddish brown	Some lamination present Indistinct boundaries	146	Distal glacial environment -Repeated influence of IRD
	LFH1	290cm 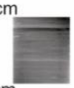 305cm 470cm  500cm	 	Sandy mud with laminations (turbidites) and IRD	5YR 5/6 Yellowish red	Dispersed IRD Massive mud Parallel lamination	134	Proximal glacial environment -Turbidity currents -Decrease of turbidites towards the top of unit -Meltwater discharge
Eugenie-Dobbin	LFED3	20 cm  40cm		-Sandy and silty mud poorly sorted and without structure -Disseminated IRD	2.5Y4/2 Dark grayish -brown	Stratified modered mud with IRD	27	Glacier growth into the bay -Sandy mud with disseminated IRD
	LFED2	121cm 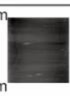 140cm 520cm  535 cm	 	Sandy mud with disseminated IRD Homogenous mud	7.5 YR 5/2 Brown 7.5 YR 6/3 Ligth brown	IRD Sporadic Massive mud	23	Glaciers retreat landward -Meltwater plumes and repeated IRD
	LFED1	200 cm  220 cm		Laminated mud	10YR 5/2 Grayish brown	Parallel lamination	19	Distal glacial environment (Dobbin Bay deglaciation) -Melwater plumes

4.3.1. Lithofacies near the Humboldt glacier

– LFH1 (02PC: 544-240 cm ; ~14 to 7.8 cal ka BP) is mainly composed of yellowish red (Munsell color 5YR 5/6) sandy mud with centimeter to subcentimeter-scale sandy laminations and disseminated gravel-sized clasts (interpreted as IRD). D90 ranges from 13 to 827 µm (mainly medium silt to coarse sand). The sandy mud laminations in this LF are characterized by a rapid upward increase and then decrease in D90, wet bulk density, magnetic susceptibility (k_{LF}) and Zr/Rb values, which can be interpreted as instantaneous turbidite deposit related with brief punctuated subglacial meltwater discharge (e.g., Powell, 1985; Figs. 11 and 12). In these depositional sequences, the meltwater-induced turbidity currents, deposit the so-called normally graded Bouma sequence (Bouma, 1962). X-CT scan images show that the transition to LFH2 is gradual and is manifested by a gradual decrease of laminations and suggesting a loss of intensity of sedimentary transport. The stable vertical variations in Ca/K (~0.7) and a* (~3.6) through the LF and the SedUnMix results indicate a homogeneous sedimentary provenance mainly dominated by sediments from the Ellesmere-Inglefield mobile belt (Fig. 13). Overall, the sedimentological characteristics of LFH1 suggest that sediments were deposited in an ice-proximal environment influenced by subglacial meltwater discharge (e.g., Reilly *et al.* 2019; Stevenard *et al*. 2021).

– LFH2 (02PC: 240-120 cm ; 7.8 to 5.2 cal ka BP // 04GC: 260-240 cm ; 6.1 to 5.7 cal ka BP) is composed of light reddish brown (5YR 6/4) sandy mud with some medium sand intercalations. The D90 (up to 553 µm), wet bulk density (up to 1.8 g cm^{-3}) and k_{LF} (up to 400 SI $x10^{-5}$) shows high values between 180 and 130 cm, which coincide with a high IRD abundance. Several disseminated gravel-sized clasts are also observed in this interval. The a* values show stable vertical variations to 160 cm and decrease markedly up to the top of this LF (Figs.10-12, Fig. S9). The Ca/K, Dol/Pl+Kfs and Kln+Ill/Pl+Kfs ratios increase progressively up to the top of the LF. The SedUnMix modelling indicate that this increase is associated with the increase in sediment input from Nares Ice Stream, i.e. from northern part of the Kennedy Channel and southern Washington Land. Altogether, LFH2 is interpreted to reflect an increasingly ice-distal environment following regional deglaciation with recurrent IRD influence. A strong decrease in the wet bulk density, $k_{LF,}$ D90, Zr/Rb, a* and

MDF_NRM (Fig. S4) values and an increase in Ca/K, Dol/Pl+Kfs and Kln+Ill/Pl+Kfs marks the transition between LFH2 and LFH3 (Fig. 13).

– LFH3 (02PC: 120-0 cm ; 5.2 cal ka BP to present // 04GC: 240-0 cm ; 5.7 cal ka BP to present // 02GC: 140-0 cm) is composed of a massive reddish brown (5YR 5/3) sandy mud with moderate bioturbation (based on the X-CT scan images). High wet bulk density, k_{LF}, a* and D90 values are observed in the upper 40 cm in comparison with the lower part of the unit, which coincides with an increase in the abundance of gravel-sized clasts (Figs. 10-12). A 4 cm granitic rock fragment is also visible in X-CT scan images of the core 02PC between 33 and 37 cm. Ca/K, Dol/Pl+Kfs and Kln+Ill/Pl+Kfs show a continuous decrease throughout the LF associated with a progressive increase the sediment input from the Ellesmere-Inglefield mobile belt sources (Fig. 13). Overall, the sedimentological characteristics of LFH3 suggest that two sedimentary processes operate within this LF. The interval between 120 and 40 cm was probably deposited in a distal glacial marine setting with low IRD influence. While the last 40 cm of the LF reflects sediment deposition influenced by an increased iceberg calving activity of the Humboldt Glacier and meltwater outwash.

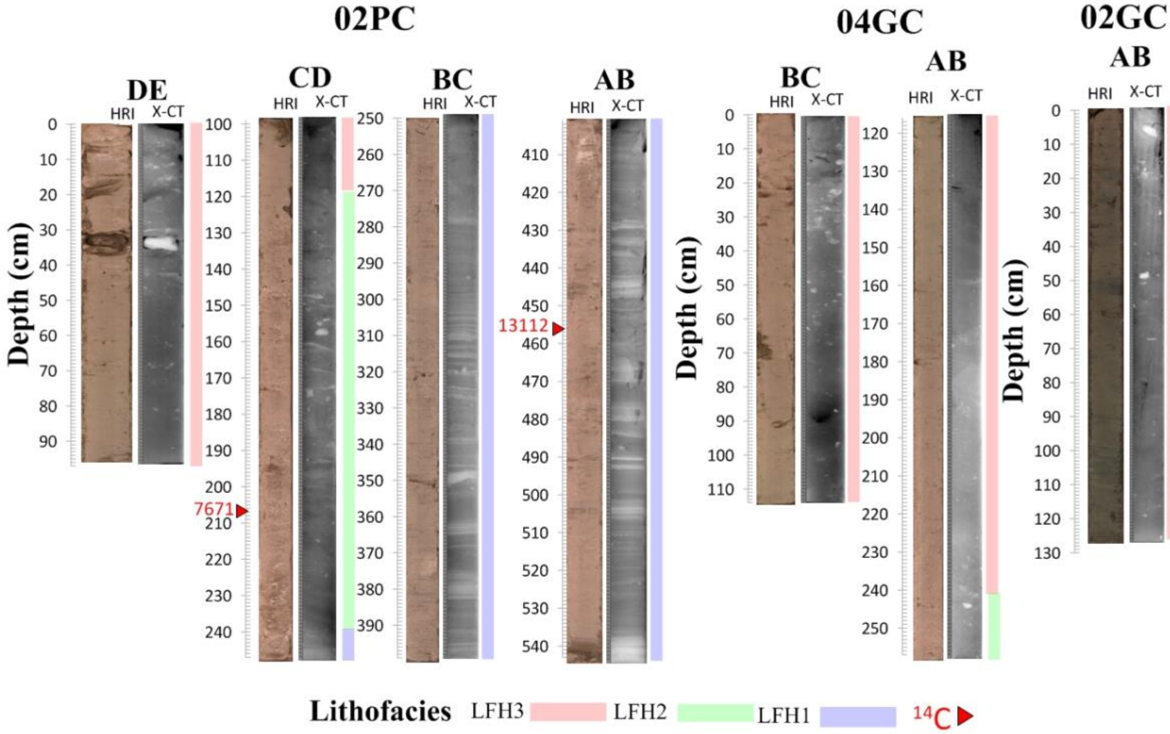

Fig. 10. X-CT scan images and associated lithofacies for each core near the Humboldt Glacier. The white in the X-CT images corresponds to areas of higher density and black to areas of lower density. Red arrows represent levels of calibrated radiocarbon dates.

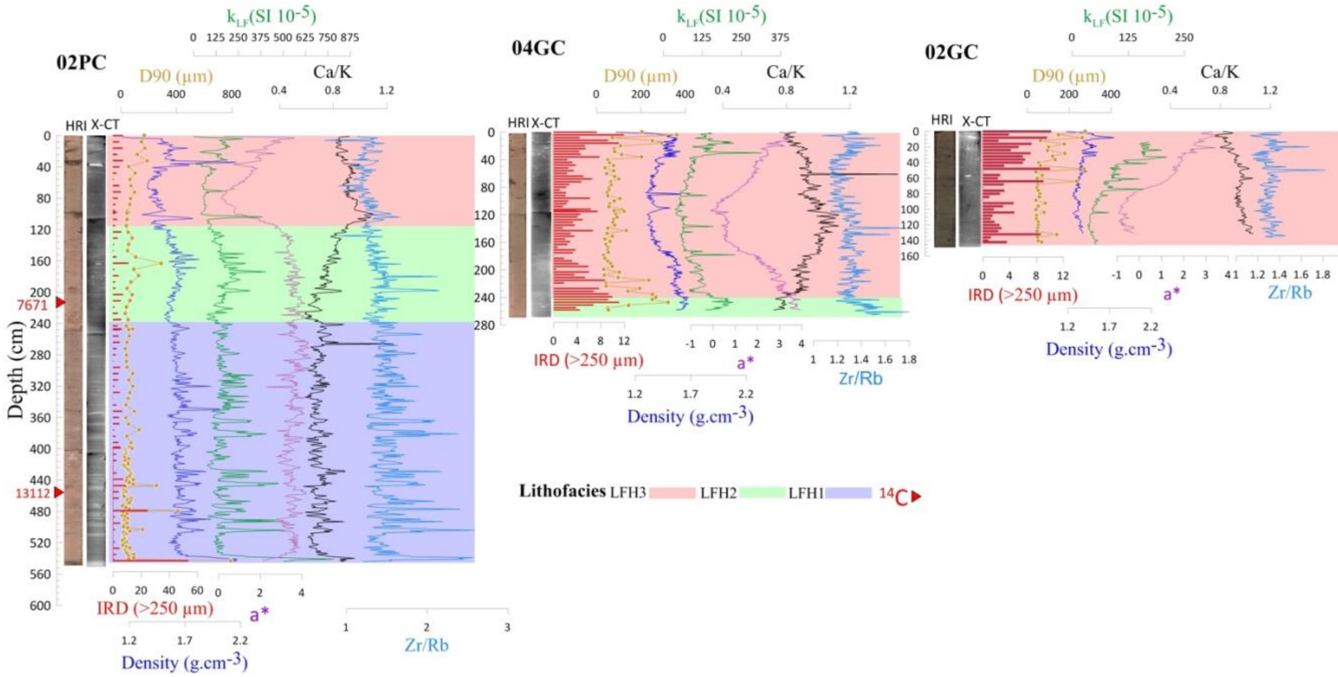

Fig. 11. Correlation of lithofacies near the Humboldt Glacier. From left to right: high-resolution core photography; X-CT scan image, % IRD (>250 µm), D90, wet bulk density, magnetic susceptibility (k_{LF}), a∗ red color indicator, and Ca/K and Zr/Rb profiles. Red arrows represent levels of calibrated radiocarbon dates.

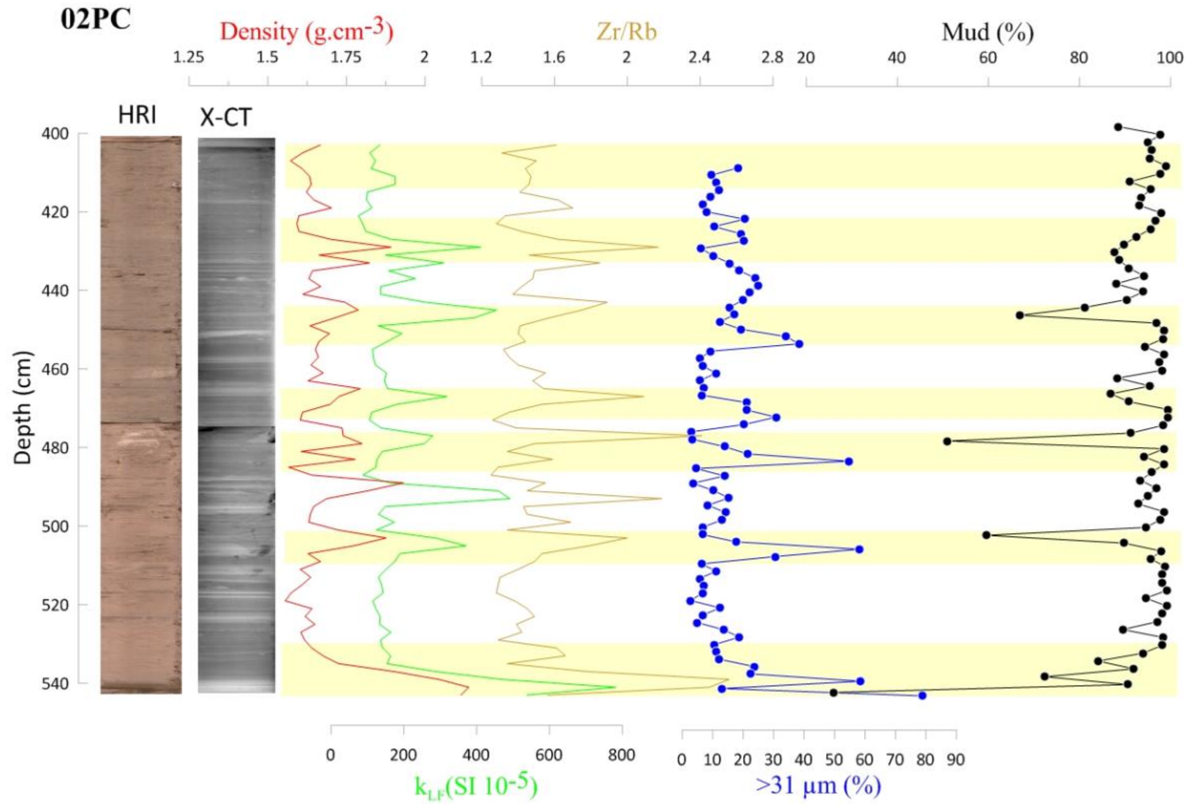

Fig. 12. High-resolution core photography, X-CT scan image, wet bulk density, magnetic susceptibility (k_{LF}), Zr/Rb, abundance of the coarse-grained (>31 µm) fraction and proportion of mud of the base of LFH1 in core 02PC. This interval of the LFH1 is characterized by centimeter to subcentimeter-scale sandy mud laminae alternating with mud laminae with isolated IRD. Turbidites are highlighted in yellow.

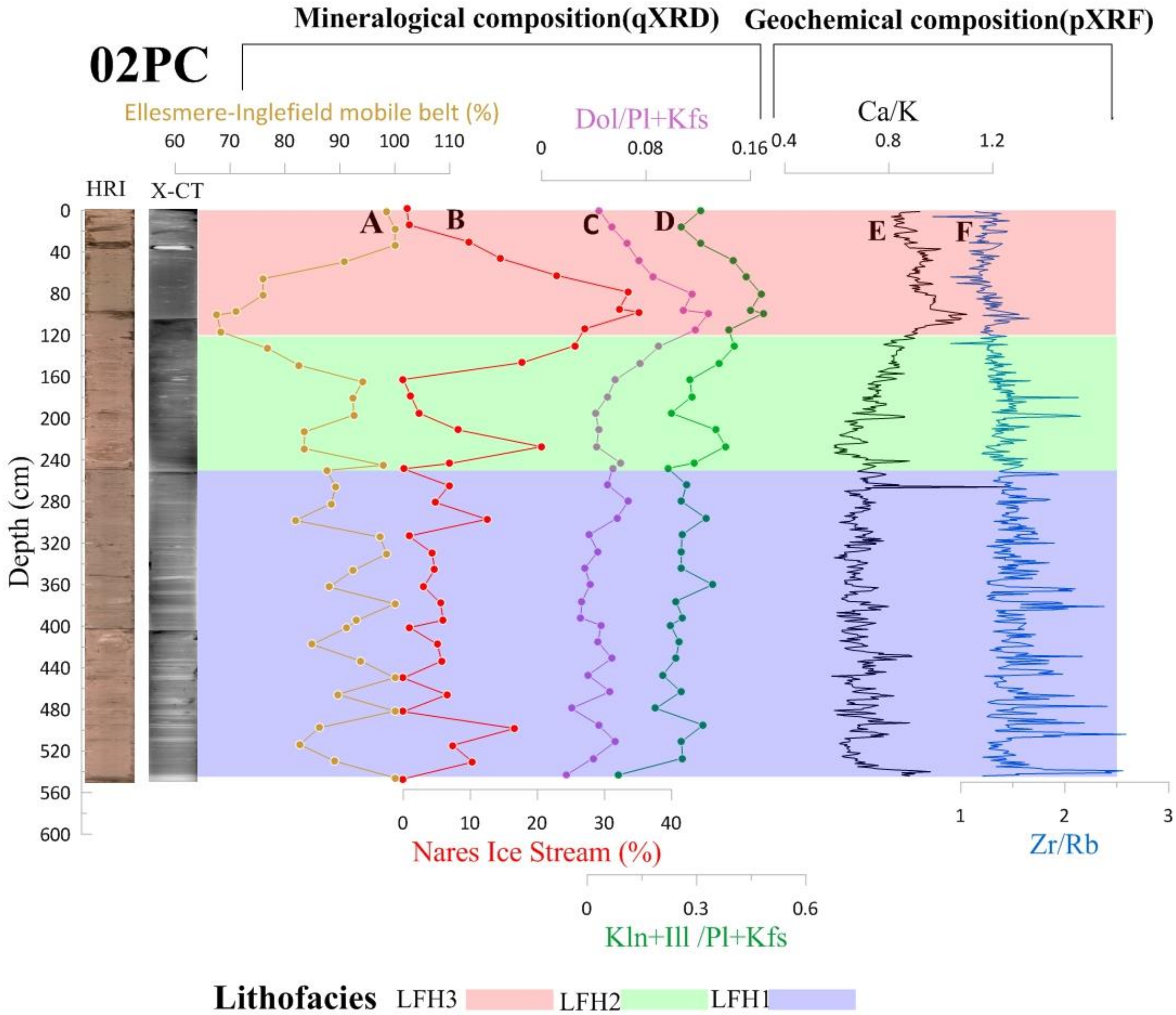

Fig. 13. Detrital proxies used for core 02PC. From left to right: high-resolution core photography; X-CT scan image; SedUnMix results with the proportions of sediment from Ellesmere-Inglefield mobile belt (blue) and the Thule Supergroup (red); mineralogical (Dol/Pl+kfs and Kln+Ill/Pl+Kfs) and chemical (Ca/K, Zr/Rb) tracers.

4.3.2. Lithofacies near the Eugenie-Dobbin glaciers

Core 12GC (ice-distal)

– LFED1 (225-160 cm; prior to ~8.0 cal ka BP) consists of a grayish brown (10YR 5/2) laminated to massive mud with disseminated gravel-sized clasts (IRD) and lack of notable evidence for bioturbation (based on the X-CT scan images; Table 4; Fig. 14). A large dropstone (limestone fragment) was found at 198-194 cm. The wet bulk density, Ca/K and Cal/Pl+kfs show the highest values at the base of the LF which then progressively decrease to the top of the LF (Figs. 15 and 18). SedUnMix modelling indicates that this decrease is associated with a constant sediment supply from the Paleozoic carbonates of eastern Ellesmere Island (Fig. 18). The D90, k_{LF}, a* and Zr/Rb values are low and remains relatively constant throughout the unit. All these indicators reflect the establishment of sub-ice shelf close to Dobbin Bay where deposition was dominated by suspension settling of fine-grained sediment from turbid meltwater plumes.

– LFED2 (160-50 cm; 8.0 to 2.2 cal ka BP) represents a homogeneous mud light brown (7.5 YR 6/3) and sandy mud brown (7.5 YR 5/2), with a few laminae intervals (Table 4; Fig. 14). IRDs are mainly present at the middle of the LF (~100-84 cm / 4.8 to 3.7 cal ka BP). The wet bulk density and D90 values show a decreasing trend throughout the LF which is interrupted by a marked increase around 76 cm. The k_{LF}, a* and Zr/Rb profiles show a marked increase at ~100 cm which then remains relatively constant to the top of the unit. While Cal/Pl+Kfs and Ill+Chl+Bt/Pl+Kfs are characterized by a decrease trend towards the top of the LF. This LF show an increase in sediment supply from from the Paleozoic carbonates of the eastern Ellesmere Island (from 85% to ~100%). All these characteristics suggest that LFED2 was deposited in a distal glacial environment mainly influenced by meltwater plumes but with an increased iceberg calving activity at the middle of the unit.

– LFED3 (50-0 cm; 2.2 cal ka BP to present) consists of a bioturbated sandy and silty mud poorly sorted and dark grayish-brown without a structure (2.5 Y 4/2; Table 4; Fig.14). The IRD, D90 and wet bulk density profiles show similar variations with high values at the base and top of the unit. k_{LF} and Zr/Rb show the highest values (up to 42 $x10^{-5}$ SI and 1.9, respectively) of all the LFs at the base of the unit which progressively decrease towards the top. a* values show a rapid upward decrease up to 8 cm (lowest values of the record; ~-0.7) after which they increase towards the top of the unit (up to 0.1). Cal/Pl+Kfs and Ill+Chl+Bt/Pl+Kfs are characterized by a decreasing trend towards the top of the LF, while Dol/Ca increases upwards showing the highest values of the record. Despite these changes in mineralogical composition, SedUnMix modeling suggest that this LF continues to be dominated by sediments from the Paleozoic carbonates of the eastern Ellesmere Island. LFED3 reflects the deposition of sediments influenced by increased iceberg calving activity and meltwater plumes from Eugenie-Dobbin Glaciers.

Core 03PC (ice-proximal)

– LFED2 (558-145 cm; 6.8 to 2.9 cal ka BP) represents a homogeneous mud light brown (7.5 YR 6/3) and sandy mud brown (7.5 YR 5/2), with a few laminated intervals (Table 4; Fig.13). X-CT scan images show that scattered gravel-sized clasts (IRD) are present throughout the LFED2. The wet bulk density profile remains relatively constant until 440 cm and then decreases progressively towards the top of the LF. The k_{LF} profile shows little variation up to 440 cm, after which it increases rapidly upwards and then decreases progressively up to 240 cm, and then increases slightly towards the top of the unit (Fig. 15). The a* have relatively constant values up to 300 cm after which it decreases progressively up to 240 cm and then increases towards the top of the unit (Fig. 15). Zr/Rb values remain relatively constant throughout the unit. The Ca/K, Cal/Pl+Kfs and Ill+Chl+Bt/Pl+Kfs ratios gradually decrease towards the top of the LF (Fig. 17). The SedUnMix modeling suggest that this decrease is associated with a low detrital carbonate input from the Paleozoic carbonates of the eastern Ellesmere Island (Fig. 17). The D90 profiles increase progressively toward the top of the unit (Figs. 15 and 17). Overall, the sedimentological characteristics of this LF suggest that the sediment deposition took place in an ice-distal environment dominated by hemipelagic sedimentation, suspension settling from turbid meltwater plume overflows and repeated IRD.

– LFED3 (145-0 cm; 2.9 cal ka BP to present) consists of bioturbated, poorly sorted, dark grayish brown sand and silty mud (2.5 Y 4/2), with no preserved laminations (Table 4; Fig. 13). X-CT scan images show the presence of scattered gravel-sized clasts (IRD) at 76-78 and ~64 cm and high concentrations in the upper part of the unit at 57-48, 37-26 and 17 to 0 cm (Fig. 14). The wet bulk density profile remains relatively constant throughout the unit. D90 and k_{LF} values slightly decreases towards the top of LF. The a* value increases upwards to 75 cm, after which it progressively decreases to 40 cm to finally increase towards the top of the unit (Figs. 14 and 16). The Cal/Pl+Kfs and Ill+Chl+Bt/Pl+Kfs are characterized by an increase towards the top of the LF. However, as observed in a* profile, Ca/K, Cal/Pl+Kfs and Ill+Chl+Bt/Pl+Kfs show a marked increase at 75 cm, which can be related to an large glaciogenic meltwater discharge event. In summary, the presence of bioturbation, the lack of preserved laminations and the scattered IRD observed in LFED3 between 145-57cm suggest the absence of a sub-ice shelf, and thus, the predominance of more open water conditions in the bay. The last 57 cm of the unit reflects sediment deposition influenced by the regrowth of a marine-based glacier which promote the release of icebergs and large inputs of rock-flour-laden meltwater into the bay.

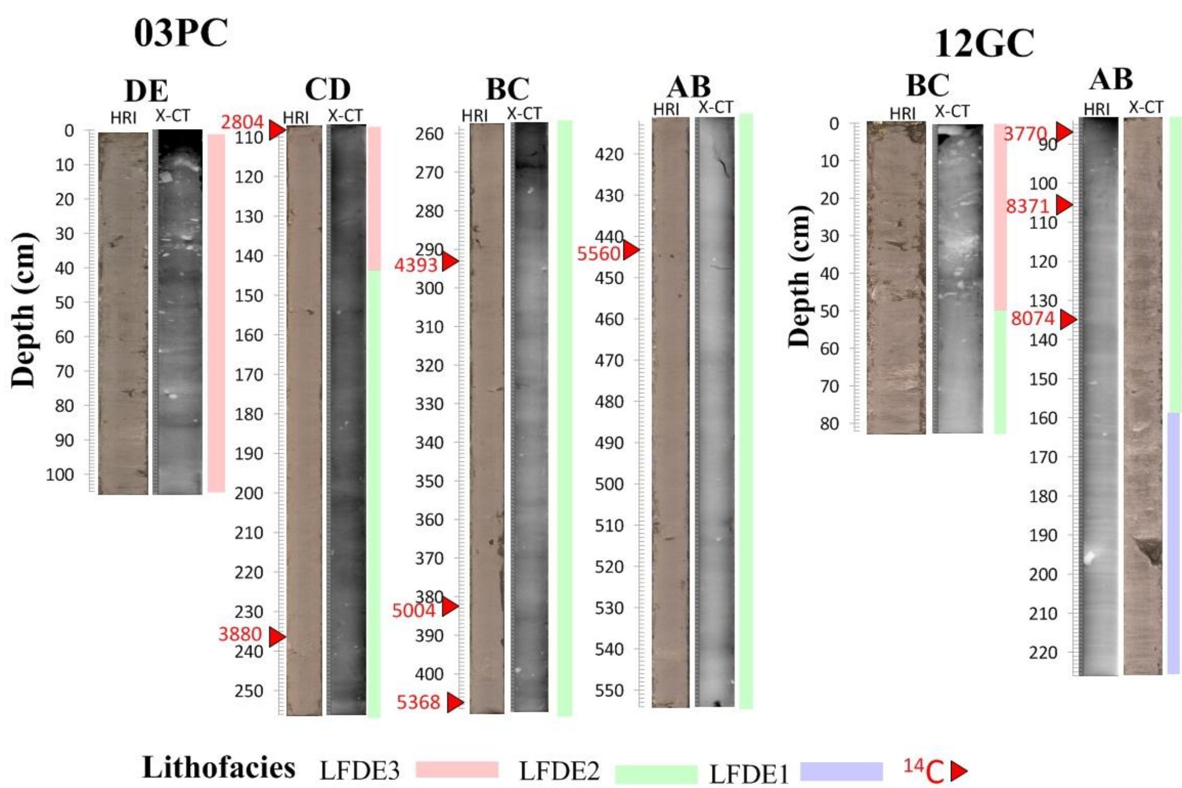

Fig. 14. X-CT scan images and associated lithofacies for each core near the Eugenie-Dobbin-Dobbin Glaciers. The white in the X-CT images corresponds to areas of higher density and black to areas of lower density. Red arrows represent levels of calibrated radiocarbon dates.

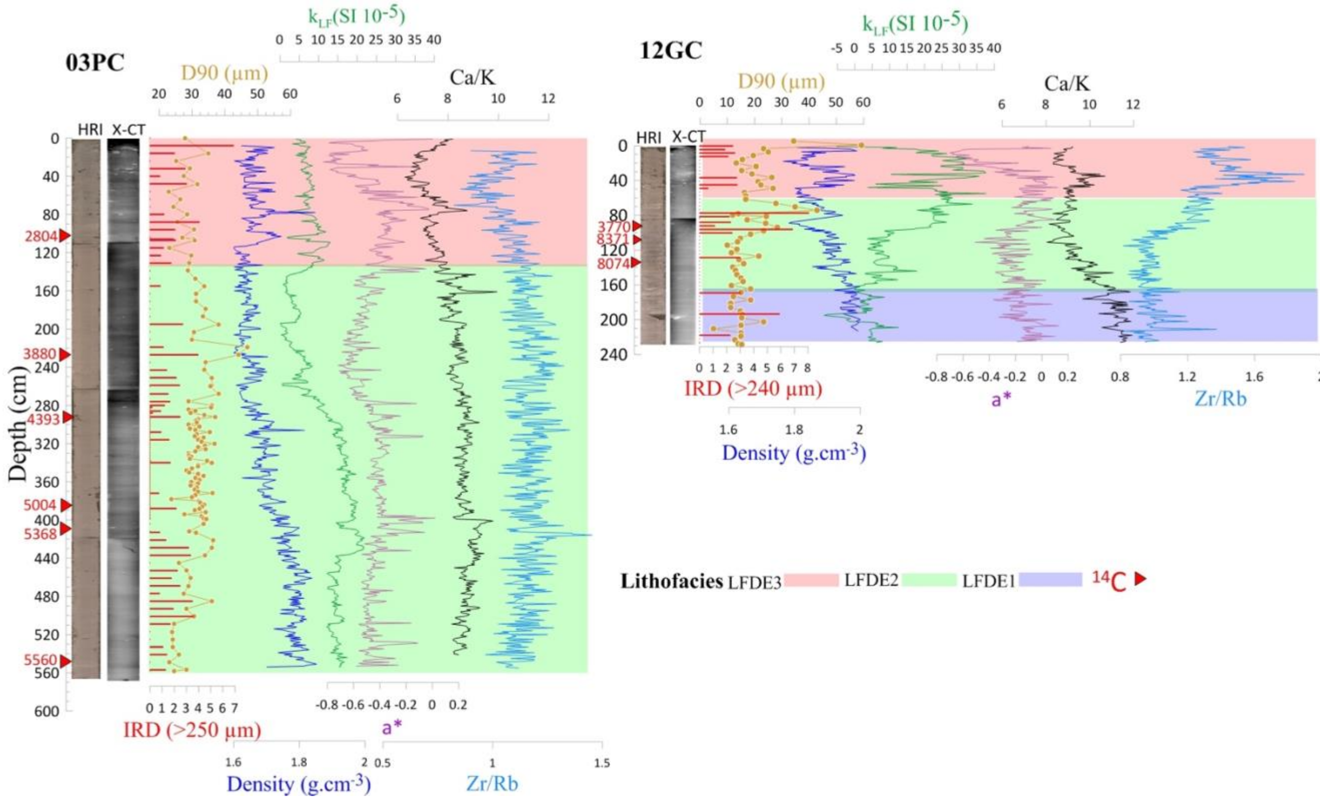

Fig. 15. Correlation of lithofacies near Eugenie-Dobbin Glaciers. From left to right: high-resolution core photography; X-CT scan image, % IRD (>250 µm), D90, wet bulk density, magnetic susceptibility (k_{LF}), a∗ red color indicator, and Ca/K and Zr/Rb profiles. Red arrows represent levels of calibrated radiocarbon dates.

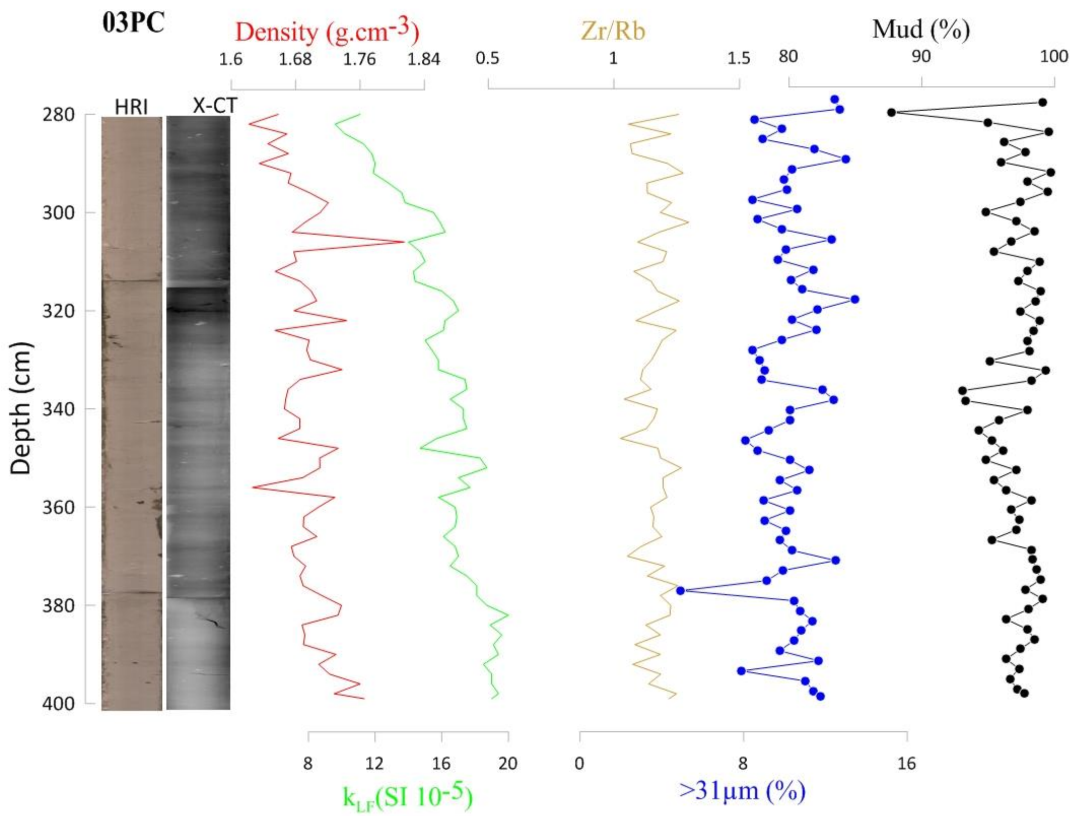

Fig. 16. High-resolution core photography, X-CT scan image, wet bulk density, magnetic susceptibility (k_{LF}), Zr/Rb, abundance of the coarse-grained (>31 µm) fraction and proportion of mud of the middle of LFED1 in core 03PC. This interval of the LFED1 is composed of a succession of centimeter to subcentimeter-scale mud and silt laminae.

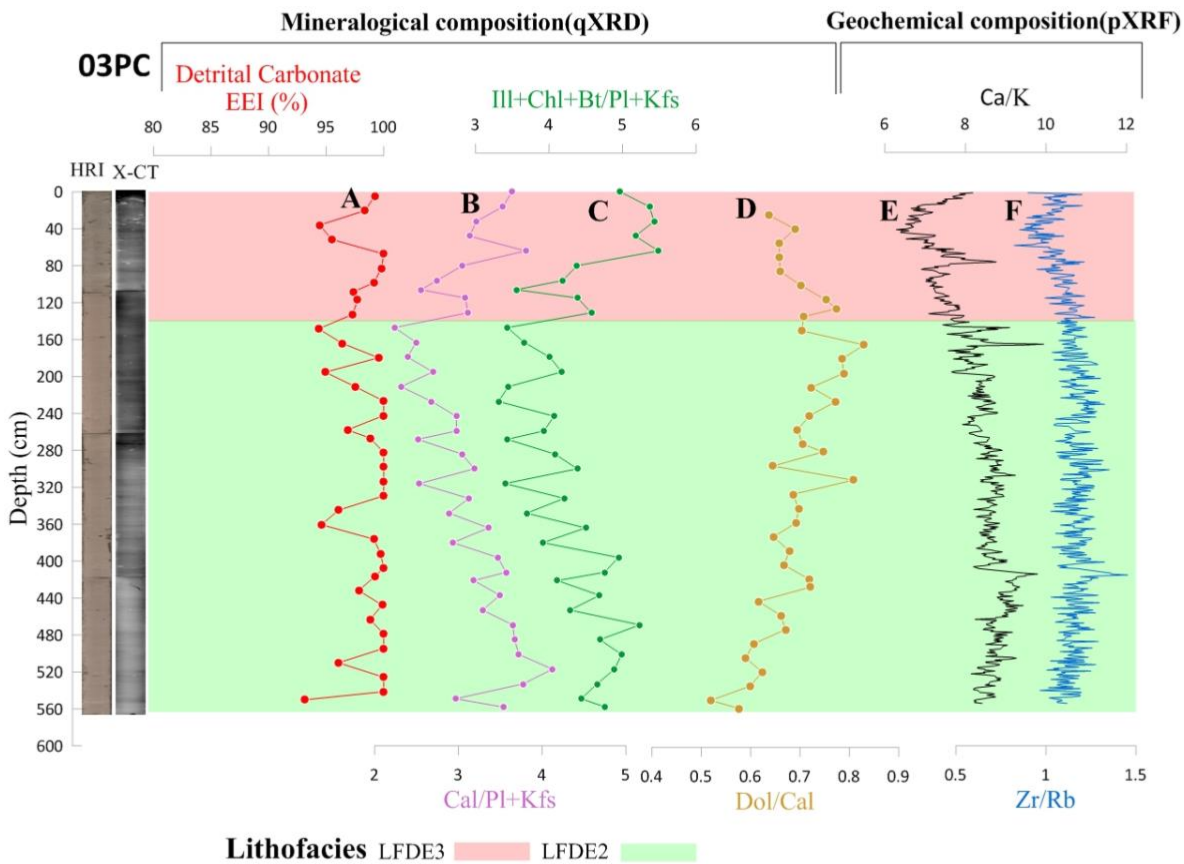

Fig. 17. Detrital proxies used for core 03PC. From left to right: high-resolution core photography; X-CT scan image; SedUnMix results with the proportions of sediment from eastern Ellesmere Island (EEI); mineralogical (Cal/Pl+kfs, Ill+Chl+Bt/Pl+Kfs, Dol/Cal) and chemical (Ca/K, Zr/Rb) tracers.

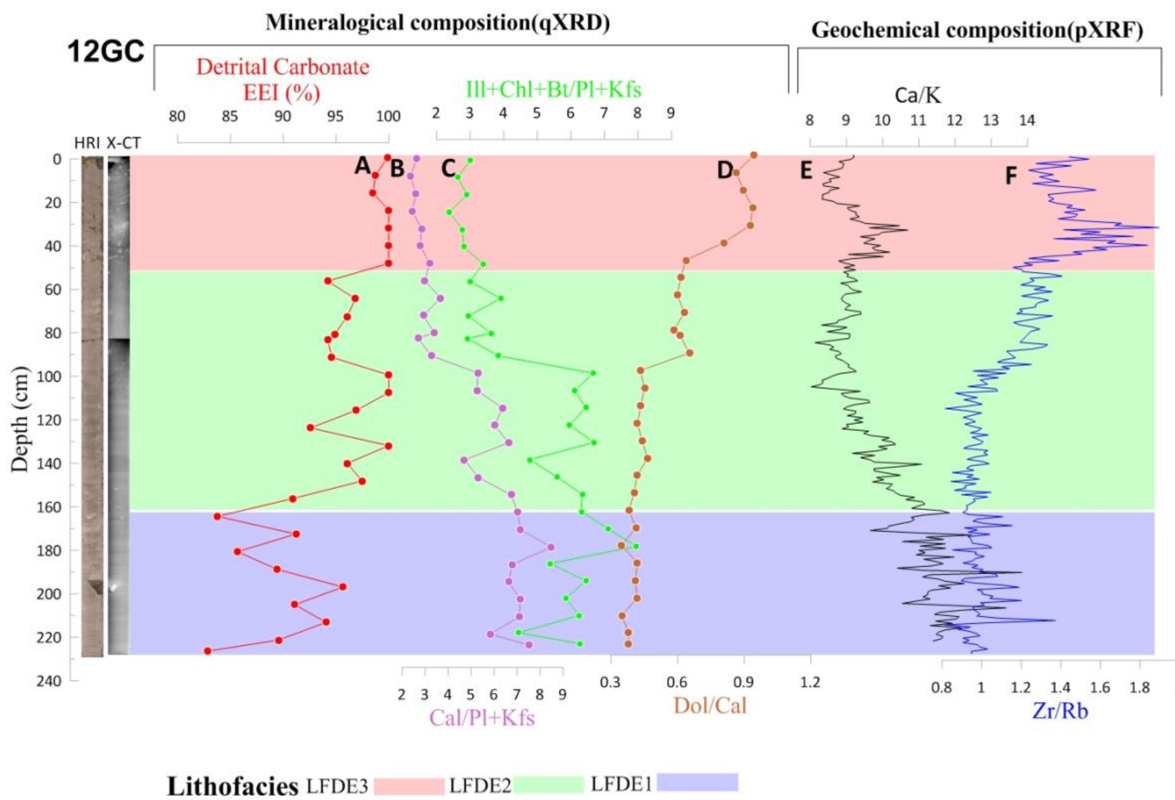

Fig. 18. Detrital proxies used for core 12GC. From left to right: high-resolution core photography; X-CT scan image; SedUnMix results with the proportions of sediment from eastern Ellesmere Island (EEI), mineralogical (Dol/Pl+kfs, Kln+Ill/Pl+Kfs, Dol/Cal) and chemical (Ca/K, Zr/Rb) tracers.

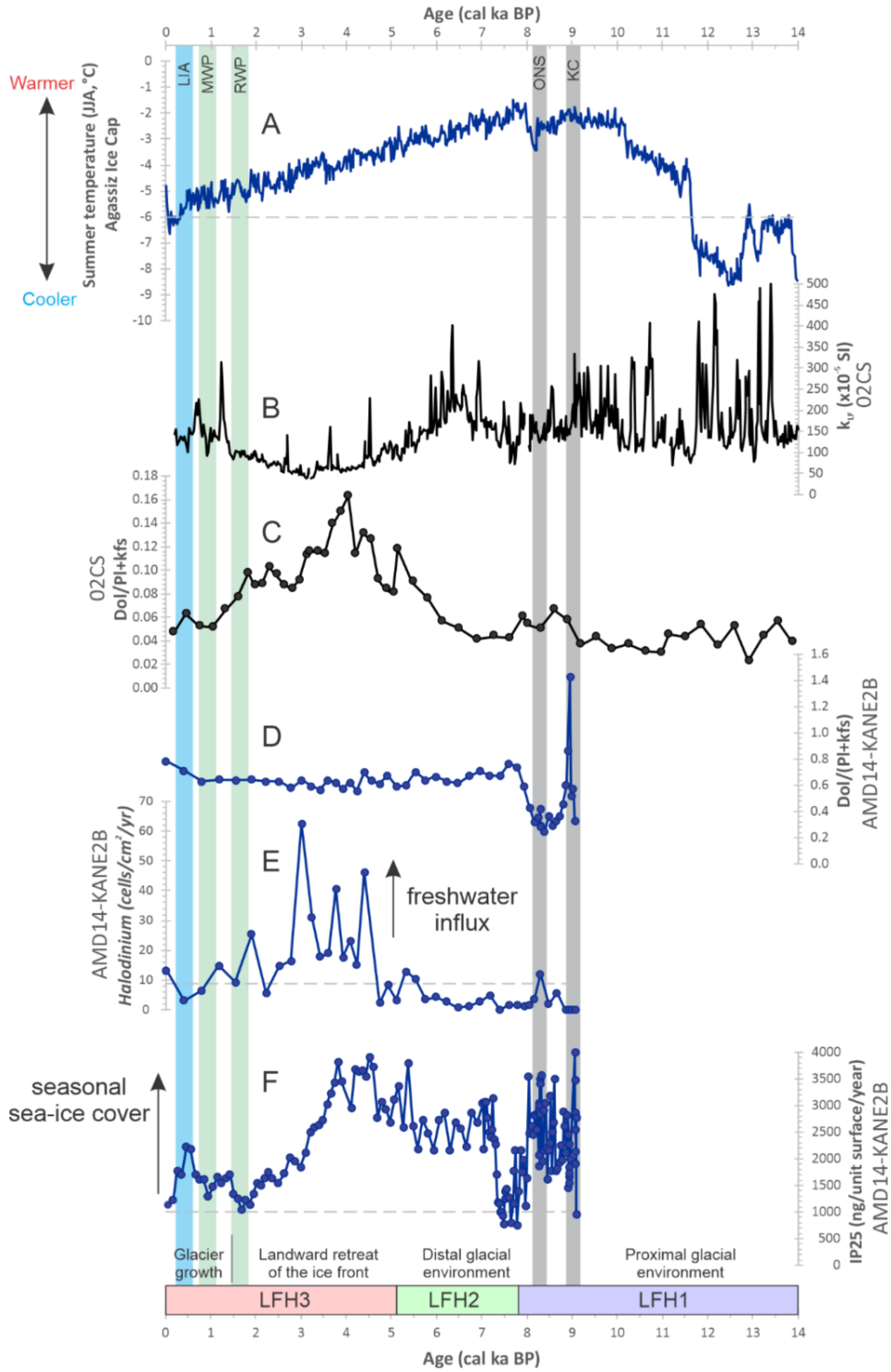

Fig. 19. Comparison of proxies from the composite Humboldt Glacier core 02CS (in age) with other regional paleoenvironmental proxies**.** (A) Modelled summer (June-July-August,

JJA) temperature (°C) anomalies of the Agassiz Ice Cap (Buizert et al., 2018). (B-C) k_{LF} and Dol/Pl+Kfs profiles from core 02CS (this study). (D-F) Dol/Pl+Kfs (Caron et al. 2020), freshwater palynomorphs influx here represented by *Halodinium* spp. (Caron et al. 2019) and the biomarker IP25 (ice proxy with 25 atoms of carbon) fluxes indicative of sea-ice conditions (Georgiadis et al., 2020) from core AMD14-Kane2b. The black dashed line represents the pre-industrial (1750 CE) values in A, the median of the datain E and the core-top influx in F. Grey shaded areas highlight the breaking of the ice saddle in Kennedy Channel (KC) and the opening of Nares Strait (ONS; Jennings et al. 2019; Caron et al., 2020). The green shaded areas shown the Roman Warm Period (RWP) and the Medieval Warm Period (MWP), while the blue area represents the Little Ice Age (LIA) interval.

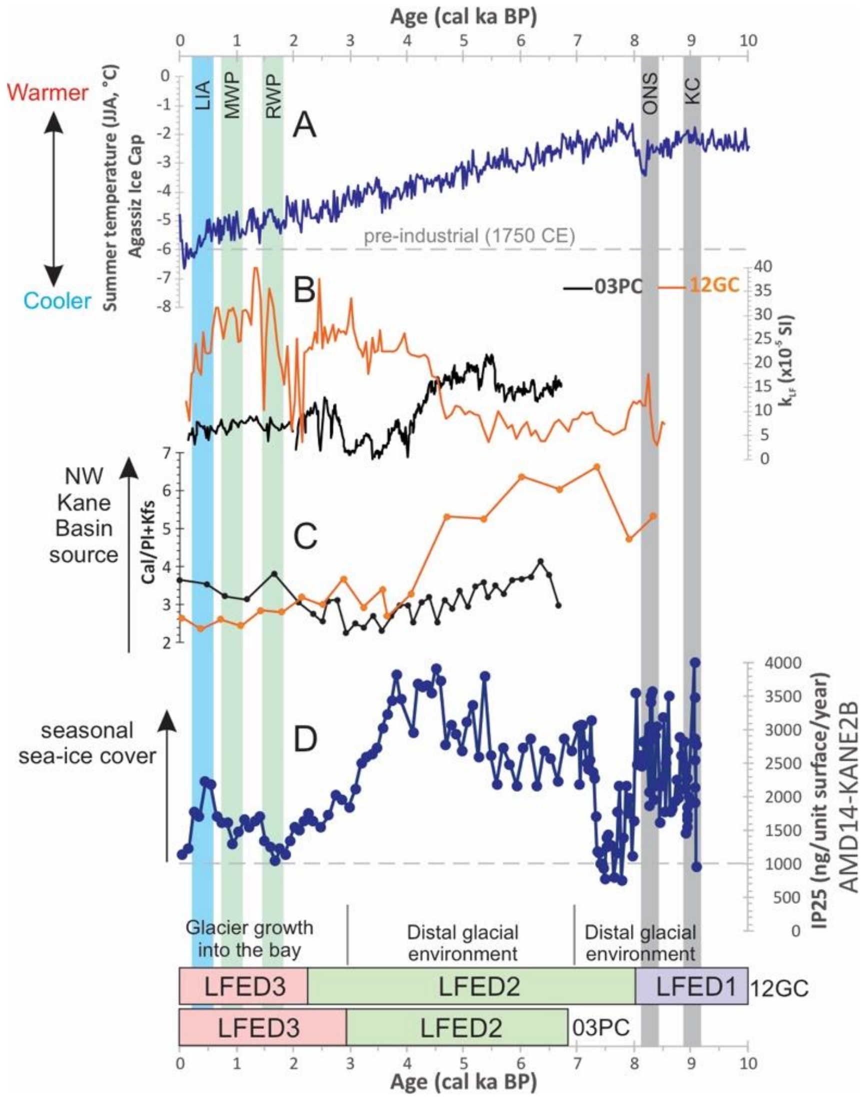

Fig. 20. Comparison of proxies from the Eugenie-Dobbin cores 03PC and 12GC (in age) with other regional paleoenvironmental proxies. (A) Modelled summer (June-July-August, JJA) temperature (°C) anomalies of the Agassiz Ice Cap (Buizert et al. 2018). (B-C) k_{LF} and Cal/Pl+Kfs profiles from cores 03PC and 12GC (this study). (D) The biomarker IP25 (ice proxy with 25 atoms of carbon) fluxes indicative of sea-ice conditions from core AMD14-Kane2b (Georgiadis et al., 2020). The black dashed line represents the pre-industrial (1750 CE) values in A and the core-top IP25 influx in D. Grey shaded areas highlight the breaking of the ice saddle in Kennedy Channel (KC) and the opening of Nares Strait (ONS; Jennings et al. 2019; Caron et al., 2020). The green shaded areas shown the Roman Warm Period

(RWP) and the Medieval Warm Period (MWP), while the blue area represents the Little Ice Age (LIA) interval.

5. DISCUSSION

5.1. Glacial to Early Holocene sediment dynamics (~14 to 8.0-7.8 cal ka BP)

Near Humboldt Glacier, our age-depth models confirm that LFH1 of cores 02CS was deposited between ~14 and 7.8 cal ka BP corresponding with the deglaciation phase of the GIS (Humboldt Glacier; England et al. 2006; Dalton et al. 2020; Søndergaard et al. 2020) and the completed opening of the Nares Strait (9.0-8.3 cal ka BP; Jennings et al. 2011; Georgiadis et al. 2018; Caron et al. 2018, 2020). The strong vertical variability in the wet bulk density, k_{LF}, coarse-grained (>31 µm) fraction, Ca/K and Zr/Rb suggest that sediment dynamic at this time was dominated by the retreat of the Humboldt Glacier grounding line towards the coast. In addition, the Ca/K profile shows a marked increase at ~8.3 cal ka BP that may be associated with an increase in detrital carbonate input following the complete opening of the Nares Strait. This enhanced detrital carbonate input could be associated with the deglaciation of the southern Washington Land region where limestones and other carbonate rocks outcrop (Fig. 4A). Overall, the sedimentological characteristics of LFH1 suggest that the Humboldt Glacier margin reached its present-day extent by ~8.3 cal ka BP, in line with interpretations of ^{10}Be data by Reusche et al. (2018) obtained on the northern flank of the Humboldt Glacier. The high boreal summer insolation and the marked increase in summer air temperatures recorded in the Agassiz ice core suggests that warmer than present summer conditions prevailed in the study area during the deglacial/Early Holocene (Berger & Loutre 1991; Lecavalier et al. 2017). These high temperatures probably played an important role in the opening of Nares Strait and the landward retreat of the Humboldt Glacier (Jennings et al. 2011; Reusche et al. 2018; Søndergaard et al. 2020). The high Pl+Kfs and K contents together with SedUnMix modeling indicate that sandy laminations in LFH1 from 02CS are composed of reworked subglacial sediments derived from glacial erosion of the Inglefield Land bedrock. Overall, the sedimentological characteristics of the LFH1 from the core 02CS support the evidence for a deglaciation of the eastern Kane Basin before 8.8 cal ka BP (Jennings et al. 2011; Georgiadis et al. 2018; Caron et al. 2019; 2020).

At the entrance of Dobbin Bay, the sedimentological features of LFED1 in core 12GC (prior to 8.0 cal ka BP) reflecting the influence of an extensive Dobbin Bay ice shelf extending from IIS, probably grounded at the mouth of bay, dominated by suspension settling of fine-grained sediment from turbid meltwater plumes. This interpretation agrees with the reconstruction of Nares Strait ice shelves based on ice shelf lithofacies of Jennings et al. (2022) and with the synthesis of ice-sheet reconstructions of Dalton et al. (2020).

5.2. Middle to Late Holocene sediment dynamics (8.0 to 3.0-2.2 cal ka BP)

The period between 8.2 and 3.0 cal ka BP was characterized by the establishment of the modern Arctic–Atlantic throughflow in the Nares Strait (e.g., Jennings et al. 2011). In Kane Basin, this interval is characterized by more open glacial marine conditions associated with seasonal sea-ice melting (Georgiadis et al. 2020; Fig. 19F) and a marked increase in freshwater palynomorph influx between 4.7 and 3.0 cal ka BP (Caron et al. 2019; Fig. 19E). In Smith Sound, higher k_{LF} values recorded in core HU2008-029-38PC between 4 and 2 cal ka BP indicates enhanced deposition by iceberg calving (St-Onge & St-onge, 2014). Likewise, mean summer surface air temperatures in the Agassiz Ice Cap were 1.3-4.6 °C warmer than pre-industrial period between 8.2 to 3.0 cal ka BP (Lecavalier et al. 2017; Buizert et al. 2018). Tentative emergence curves from Washington Land region suggest a progressive decrease in relative sea level from 80 to 20 m over the western and southern Washington Land during the Middle to Late Holocene, related to isostatic adjustment after retreat of GIS (Humboldt Glacier; Bennike, 2002). This period is captured in LFH2 of core 02CS near Humboldt Glacier by an upward decrease in k_{LF} values and IRD content and a progressive increase in the contribution of detrital carbonate-rich sediments (Figs. 19B-C and 21D). Variations in IRD content, particularly in terms of IRD peaks, reflect periods of ice shelf instability or break-up, resulting in the loss of the ice shelf debris filtering process and the evacuation of IRD (Jenning et al. 2022).

The Dol/Pl+Kfs profile of core AMD14-Kane2b located in the central part of the Kane Basin (Caron et al. 2020; Fig. 19D) shows few variations over this interval. Based on these results, we hypothesize that a combination of higher summer atmospheric temperatures with the progressive decrease in relative sea level promoted the remobilization of carbonate-rich glaciogenic sediments stored on the southern coast of Washington Land, as well as their subsequent transport by sea-ice and meltwater plumes eastward to the Kane Basin. Indeed, based on an increase in IP25 fluxes in core AMD14-Kane2b (Fig. 19E), Georgiadis et al. (2020) document a recurrent and seasonal formation of a stable ice arc in the Kane Basin between 7.5 and 3.0 cal ka BP. This extended sea-ice cover may have contributed during the late spring and early summer with an enhanced sea-ice transport and discharge of turbid meltwater plumes rich in detrital carbonates from southern Washington Land. These interpretations agree with reconstructed ice retreat patterns on the northern flank of the Humboldt Glacier and Washington Land during the Middle to Late Holocene (Bennike, 2002; Dalton et al. 2020; Søndergaard et al. 2020).

At the entrance of Dobbin Bay, the highest values in wet bulk density, Ca/K, Cal/Pl+Kfs recorded between 8.0 and 4.5 cal ka BP in core 12GC suggest an increased fine-grained detrital carbonate input at the Dobbin Bay entrance (Figs. 20B-C and 21C). We infer that an increased sea ice cover (Fig. 20D), coupled with higher summer atmospheric temperatures (1.3-4.6 °C warmer than pre-industrial period) and increased southward flow of Arctic sea ice, could have triggered during late spring or early summer an increased input of turbid meltwater plumes rich in detrital carbonate into both northwestern part of the Kane Basin (e.g., Scoresby Bay, John Richardson Bay and Readmore Harbour; England, 1996) and Dobbin Bay entrance. Note that the core 03PC is located in the inner Dobbin Bay and, therefore, is unlikely to be influenced by the ice rafting and meltwater input derive from northern part of the Kennedy Channel. The predominant lithofacies in this area of northern Nares Strait is an IRD-free stratified mud deposited by meltwater suspension beneath the ice shelf and beyond the calving line (Jennings et al. 2022).

Radiocarbon ages obtained on deglacial Holocene deltas at the inner Dobbin Bay suggest that the head of the bay became ice-free ~8.1 to 7.6 cal ka BP (England, 1996; Robertson, 1999). In core 03PC, high k_{LF} and a* values and high sand contents (up to 6%) observed prior to 4 cal ka BP in LFED2 provides evidence for both a landward retreat of the Eugenie Glacier and rapid regional emergence (related to post-glacial rebound). Indeed, the landward retreat of marine-terminating glaciers promotes the formation of glacial outwash plains and deltas at the glacial front (Powell, 1981). In this environment, glacial meltwater streams can introduce a mixture of fine-grained sand and glacial flour in more ice distal marine locations (Powell 1981; Stevenard et al. 2022). As indicated above, this landward retreat was most likely fostered by higher summer atmospheric temperatures (3-4 °C warmer than pre-industrial period) that prevailed at this time (Fig. 19A). A radiocarbon on one shell collected from an inner lateral moraine of the Eugenie Glacier at ~38 m.a.s.l. returned an age of 3460 ± 70 BP (3561 – 3923 cal a BP; England, 1996), providing a maximum age for moraine formation. This ^{14}C age supports the idea that Eugenie Glacier was behind its present-day position at ~4 cal ka BP, in agreement with our results. Few variations are observed in k_{LF} and Cal/Pl+Kfs profiles between 4 and 2.2 cal ka BP (Fig. 21B-C), suggesting a stabilization of the local glacier activity and/or or the beginning of glacier regrowth. The fine-grained stratified sediments, with few IRD and foraminifers, correspond to meltwater-dominated Northern Hemisphere ice shelf facies, which is probably present in other Arctic margin contexts (Jennings et al. 2022).

5.3. Late Holocene to modern sediment dynamics (3.0-2.2 to present day)

Cooler conditions driven by a long-term decrease in boreal summer insolation were established regionally in the Arctic from ~3.5 cal ka BP, associated with the onset of Neoglacial period. These conditions promoted across the Arctic regrowth in glaciers/ice caps (e.g., Blake et al. 1992; Solomina et al. 2015; Reusche et al. 2018) and colder surface waters (e.g., Ledu et al. 2010; Caron et al. 2019). Georgiadis et al. (2020) report a decrease in sea ice cover in the Kane Basin after ~3.5 cal ka BP and associate this with the prevalence of strong winds that favor the export of sea ice across the Nares Strait and affect the formation of the Kane Basin ice arc.

Near the Humboldt Glacier, the decrease in sediment accumulation rates (from 48 to 28 cm ka^{-1}), the predominance of silty-clay sediments, the low IRD content and the progressive increase of sediments originating from Ellesmere-Inglefield mobile belt (as reflected by the upward decrease in Ca/K, Dol/Pl+Kfs and Kln+Ill/Pl+Kfs) observed between 3.0 to 1.5 cal ka BP (107 and 40 cm) in 02CS provide evidence for a landward retreat of the Humboldt Glacier ice front during this time interval. This interpretation agrees with ^{14}C data from reworked marine mollusks collected in moraines along the southern and northern margin of the Humboldt Glacier, which suggest that the glacier was behind its present-day position between ~3.7 and 0.3 cal ka BP (Bennike, 2002; Søndergaard et al. 2020). This landward retreat was likely driven by 1) higher summer atmospheric temperatures (0.6-2.5 °C warmer than in the pre-industrial period; Lecavalier et al. 2017; Buizert et al. 2018) which would increase surface melting on Humboldt Glacier; and 2) the fact that the bed topography on the northern flank of Humboldt Glacier was below sea level during this period (Bennike, 2002; Morlighem et al. 2017; Søndergaard et al. 2020). However, the glacial retreat observed at Humboldt Glacier contrasts with the glacier growths observed along the west Greenland coast during the onset of Neoglaciation (~4.3 to 2 cal Ka BP, e.g., Briner et al. 2016; Schweinsberg et al. 2017). The observed difference in glacial dynamics between these two regions has been associated to the fact that marine based outlet glaciers in western Greenland margin respond more rapidly to climate and ocean change than glaciers in northern Greenland (e.g., Axford et al. 2019; Søndergaard et al. 2020).

Conversely, the sedimentological characteristics of LFH3 observed after 1.5 cal ka BP in 02CS indicate an increase in iceberg calving rates and meltwater plumes during this time (Fig. 21). We argue that the cooler conditions associated with the Neoglaciation promoted a greater advance of the Humboldt Glacier marine-based ice front towards its maximum Little Ice Age (LIA) extent (~1350–1850 CE or 600-100 cal a BP; Reusche et al. 2018) and, consequently, an enhanced input of glacially eroded sediments (rock flour) and a greater rate of iceberg discharges to the eastern Keane Basin during this time. These conditions also appear to have triggered a more stable ice tongue for Petermann Glacier in Northwest Greenland after 2 cal ka BP (Reilly et al. 2019). Few changes in sediment dynamic are observed in 02CS during the Roman Warm Period (RWP; 2.2-1.6 cal ka BP; Bianchi and McCave, 1999) and the Medieval Warm Period (MWP; ~1050-600 cal a BP; Bradley 2003; Spielhagenet al. 2011), which are characterized by Arctic summer temperatures warmer than those in the pre-industrial period (Kaufman et al. 2009). However, as no ^{210}Pb and ^{137}Cs analyses were performed to improve the chronology for 04GC (top of the composite sequence 02CS), this interpretation needs to be taken with caution.

In inner Dobbin Bay, the upward decrease in sediment accumulation rates (from 100 to 63 cm ka^{-1}) recorded after ~3 cal ka BP in 03PC (LFED3; 140 cm), together with the long-term decrease in D90 (from 40 to 20 µm), Ca/K and Dol/Cal, scattered IRD and an increase in Cal/Pl+Kfs and Ill+Chl+Bt/Pl+Kfs, suggest that sedimentary regimes in the inner bay were mainly driven by snowmelt runoff and meltwater plumes during the spring/summer season. We argue that cooler temperatures associated with the Neoglaciation promoted a greater advance of the Eugenie Glacier and local glaciers around Dobbin Bay towards the coast. A rapid increase in the Ca/K and a* profiles observed in cores 03PC and 12GC between ~2 and 1 cal ka BP, which is concomitant with the RWP and MWP, indicate that this Neoglacial re-advanced was likely interrupted during this time. Based on foraminifera fluxes of two sediment cores located in the North Water Polynya (NOW) area, Jackson et al. (2021) suggests an increasing incursion of Atlantic water into the region during the RWP and to a lesser extent during the MWP. Thus, we hypothesize that these warm oceanic conditions contributed to a rapid and short retreat of the glaciers around Dobbin Bay during the RWP and in less intensity during the MWP. Moreover, the higher k_{LF}, Zr/Rb Dol/Ca values observed between ~2 and 0.5 cal ka BP in core 12GC suggest that enhanced export of sea-ice-rafted sediments across the Nares Strait during this time (Georgiadis et al. 2020) considerably impacted the sedimentary environment at the entrance of Dobbin Bay. Following these warm periods, the high coarse ice-rafted clast contributions, together with high D90 and Ca/K values, recorded between 0.6 and 0.1 cal ka BP in cores 03PC and 12GC suggest colder conditions associated with the LIA promoted glacier growth and increased iceberg calving activity in Dobbin Bay.

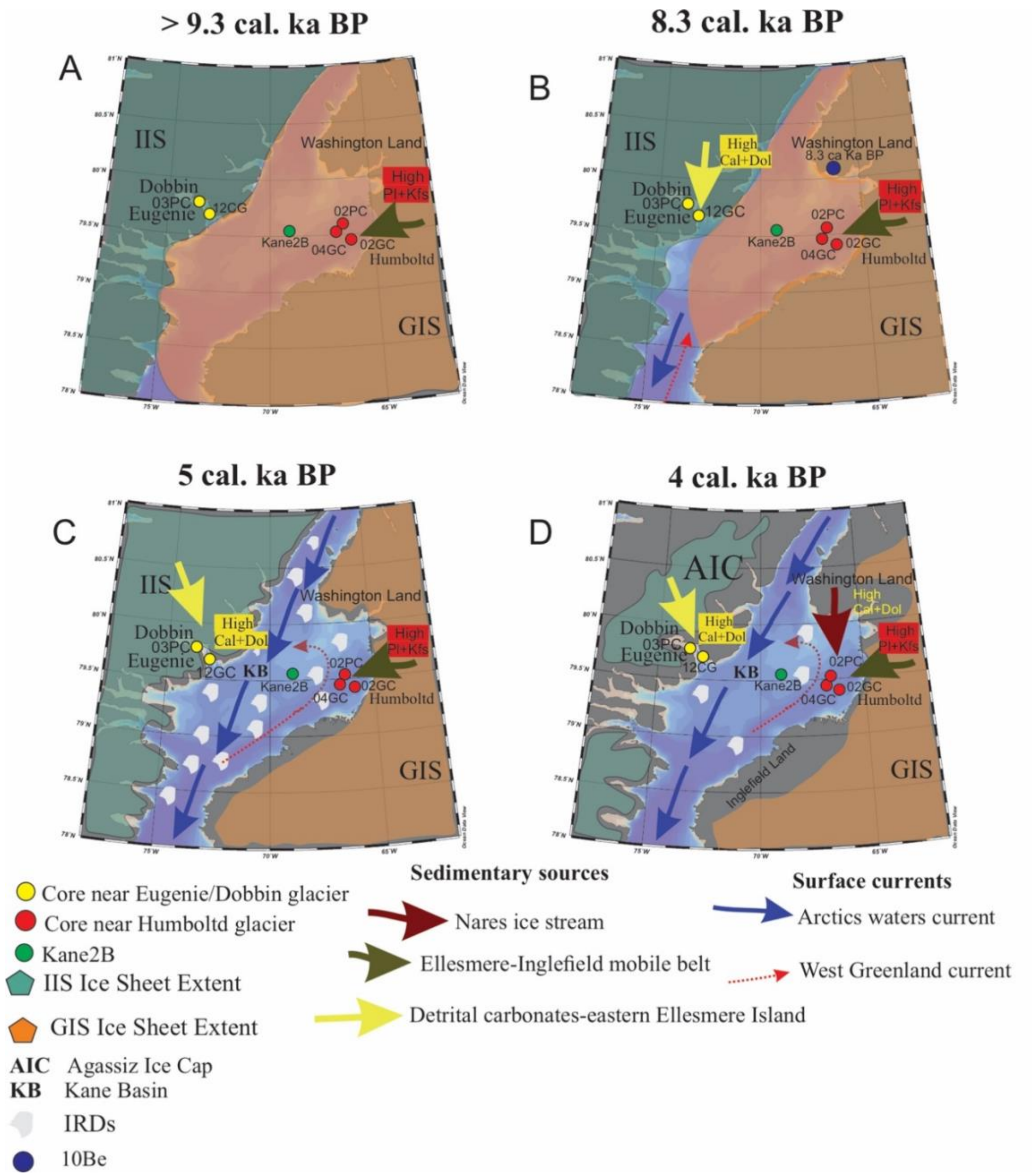

Fig. 21. Schematic map of the Kane Basin showing the evolution of Holocene sediment dynamics near the Humboldt and Eugenie-Dobbin glaciers (modified from Georgiadis et al. 2018). The West Greenland Current (WGC) is represented by red arrows and the southward flow of Arctic water (BIC) by blue arrows. The arrows represent the contribution of sediment sources.

6. CONCLUSIONS

The multiproxy approach performed on well-dated sediment cores recovered near Humboldt Glacier (northwest Greenland) and Eugenie-Dobbin Glaciers (Dobbin Bay, eastern Ellesmere Island) allowed us to reconstruct changes in detrital sediment provenance and transport on either side of the Kane Basin related to climate variability since the last deglaciation, as well as document the sensitivity of the Eugenie-Dobbin and Humboldt Glaciers to changing climatic and oceanic conditions during the Holocene. Overall, the results of this study yield the following generalizations and conclusions:

- The sedimentary processes were different on the two margins, with the presence of three distinct lithofacies (LF) at Humboldt and Eugenie-Dobbin corresponding to the periods of Glacial to Early Holocene sediment dynamics (~14 to 8.0-7.8 cal ka BP); Middle to Late Holocene sediment dynamics (8.0 to 3.0-2.2 cal ka BP) and Late Holocene to modern sediment dynamics (3.0-2.2 to present day).

- Near Humboldt Glacier, LFH1 represents a proximal glacial environment dominated by meltwater discharge (14 to 7.8 cal ka BP). LFH2 is interpreted as a distal glacial environment that existed predominated during the Middle Holocene, with repeated influence of IRD discharges (7.8 to 5.2 cal ka BP). LFH3 represents a landward retreat of the ice front during the Middle to Late Holocene (5.2 to 1.5 cal ka BP to present), followed by regrowth during the Late Holocene (1.5 cal ka BP to present). Near Eugenie-Dobbin Glacier, LFED1 is interpreted as a proximal glacial environment influenced by the presence of an extensive Dobbin Bay ice shelf (prior to 8.0 cal ka BP). LFED2 is interpreted as a distal glacial environment influenced by the Dobbin Bay deglaciation and by the landward retreat of glaciers around the bay (8.0 to 3.0-2.2 cal ka BP), while LFED3 is characterized by a sandy mud with scattered IRDs reflecting a period of glacier growth around the bay associated with Neoglacial cooling (3.0-2.2 cal ka BP to present).

- Linear discriminant analysis and the Cal+Dol - Pl+Kfs - Ill ternary diagram indicate that LFH1, near the Humboldt Glacier, is dominated by igneous-metamorphic rocks from the Ellesmere-Inglefield source. At the base of LFH2, the Ellesmere-Inglefield source predominates at LF, and towards the top of LFH2, the Nares Ice Stream source dominates. Finally, LFH3 is composed of sediments from the Nares Ice Stream at the base and igneous-metamorphic rocks from the Ellesmere-Inglefield source at the top. Detrital carbonate remains the only sediment source in the Dobbin Bay sedimentary record.

Overall, this multiproxy study has improved our knowledge on the deglacial to postglacial history of the Kane Basin (an important area for the establishment of the modern Arctic-Atlantic throughflow) and provided a better understanding of the glaciological and sedimentary processes operating near Eugenie-Dobbin and Humboldt Glaciers since the last ~14 cal ka BP.

7. Acknowledgments

We are grateful to the captain, officers, crew, and scientists on board the CCGS Amundsen during the 2019 ArcticNet expeditions (Leg 2b) for the recovery of cores used in this study. We also thank: Daniel Amirault and Paco Ferrand from Amundsen Science for the support with the mapping and sub-bottom surveys; Maria-Emilia Rodriguez-Cuicas, Anne Corminboeuf, Jade Brossard and Simon Faye from ISMER-UQAR and Joshua Evans from UNB for their help with the collection of sediment cores; Quentin Beauvais, Dominique Lavallée and Claude Belzile from ISMER-UQAR for their technical support and advice in the laboratory; Juliette Girard (ISMER-UQAR) for her assistance in the determination of paleomagnetic tie-points; and Camille Brice (ISMER-UQAR) for the drawing up of Fig. 4A. We also thank Urs Neumeier (ISMER-UQAR) and Matt O'Regan (Stockholm University) for their insightful comments on an earlier version of the manuscript. This research was funded by ArcticNet (a Network of Centres of Excellence Canada), Geotop (MSc scholarship provided to Christian Bicera Nfundiko), Québec-Océan, and the Natural Sciences and Engineering Research Council of Canada (NSERC) through Discovery Grants to J.-C. Montero-Serrano and G. St-Onge.

Data availability

All analytical data presented will be available electronically in the PANGAEA database (https://www.pangaea.de/).

Author contributions

Christian Bicera Nfundiko performed all analysis, co-wrote the original draft of the manuscript, and made the figures. Jean-Carlos Montero-Serrano led the project, acquired the funds for core sampling and analysis, ran the SedUnMix analyses, acquired the radiocarbon dates, determined the paleomagnetic tie-points, made the Bayesian age model and co-wrote the original draft of the manuscript. Guillaume St-Onge co-led the project, supervised the physical and paleomagnetic analysis of sediment cores, and acquired the radiocarbon ages. Alexandre Normandeau co-led the project, acquired the radiocarbon ages, and assisted with data interpretation. All authors contributed to reviewing and editing the manuscript.

CONCLUSION GÉNÉRALE

L'étude de cinq carottes sédimentaires, deux récupérées près des glaciers Eugénie-Dobbin (baie de Dobbin, île d'Ellesmere) et trois près du glacier Humboldt (nord-ouest du Groenland) ont été étudiées afin de : 1) déterminer des lithofaciès (LF) et reconstituer les transferts sédimentaires en provenance des glaciers Humboldt et Eugénie-Dobbin au cours de l'Holocène et 2) documenter l'influence des changements climatiques et océanographiques holocènes sur la dynamique des glaciers Humboldt et Eugénie-Dobbin.

Le cadre chronostratigraphique des carottes à proximité des glaciers Eugénie-Dobbin a été établie par des datations ^{14}C d'onze fragments de coquilles de mollusques. En revanche, les sédiments marins à proximité du glacier du glacier Humboldt (02PC et 04GC) sont caractérisés par une faible concentration des carbonates biogéniques (foraminifères et coquilles de mollusques), ce qui limite la construction d'un modèle d'âge dans cette région. Ainsi, l'une des contributions les plus importantes de ce travail a été le développement d'un modèle d'âge solide pour la séquence composite 02CS (qui comprend les carottes 04GC + 02PC) en combinant deux âges ^{14}C dérivés d'un mélange de foraminifères avec des marqueurs paléomagnétiques (plus précisément l'inclination). Le modèle âge indique que la séquence composite 02CS s'étend sur les derniers 14 000 ans. Cette séquence sédimentaire constitue ainsi une nouvelle archive paléoclimatique couvrant la période du Tardiglaciaire à l'Holocène dans l'est du bassin de Kane et le détroit de Nares.

L'ensemble des résultats montre qu'il y a eu des processus sédimentaires différents à l'est et à l'ouest du bassin de Kane, avec la présence des trois LF distinctifs à Humboldt (LFH) correspondant à la période Tardiglaciaire et aux trois périodes de l'Holocène (précoce, moyen et tardif) et de trois LF à Eugenie-Dobbin (LFED) qui correspondent aux deux dernières périodes de l'Holocène.

Près du glacier Humboldt, LFH1 représente un environnement glaciaire proximal dominé par les rejets d'eaux de fonte (14 à 7,8 cal ka BP). LFH2 suggère qu'un environnement glaciaire distal prédomine pendant l'Holocène moyen avec une influence répétée de débris délestés par les icebergs ou IRD (7,8 à 5,2 cal ka BP). LFH3 suggère un retrait du front glaciaire vers la côte pendant l'Holocène moyen à tardif (5,2 à 1,5 cal ka BP à nos jours), suivi d'une re-croissance (1,5 cal ka BP à nos jours). Quant à la provenance de sédiments proche du glacier Humboldt, les sédiments détritiques de LFH1 proviennent des roches ignées-métamorphiques de la ceinture d'Ellesmere-Inglefield. LFH2 est constitué à sa base de roches provenant de la ceinture d'Ellesmere-Inglefield, vers le sommet, la source des sédiments provient du courant glaciaire de Nares (*Nares Ice Stream)*. Ensuite, LFH3 comprend des sédiments du courant glaciaire de Nares à sa base et des roches ignées-métamorphiques de la ceinture Ellesmere-Inglefield vers le sommet.

Près du glacier Eugénie-Dobbin, LFED1 est interprété comme un environnement glaciaire proximal influencé par la présence d'une plate-forme glaciaire étendue de la baie de Dobbin (avant 8,0 cal ka BP). LFED2 est interprété comme un environnement glaciaire distal influencé par la déglaciation de la baie Dobbin et par le retrait vers l'intérieur des terres des glaciers autour de la baie (8,0 à 3,0-2,2 cal ka BP), tandis que LFED3 est caractérisé par une boue sableuse avec des IRD disséminés qui reflètent une période de croissance des glaciers autour la baie associée au refroidissement néo-glaciaire (3.0-2,2 cal ka BP à nos jours). Les carbonates détritiques restent la seule source de provenance de sédiments dans les enregistrements sédimentaires de la baie de Dobbin avec une influence secondaire de sédiments provenant du détroit de Nares pour la carotte située à l'entrée de la baie.

Dans l'ensemble, cette étude multi-traceurs a permis de peaufiner l'évolution de la dynamique sédimentaire dans la région de l'est du bassin de Kane depuis la période Tardiglaciaire ainsi que de documenter l'impact des changements climatiques et océanographiques holocènes sur les apports de sédiments provenant des glaciers Eugenie-Dobbin et Humboldt. Finalement, des analyses similaires à la présente étude pourraient être réalisées sur des carottes à boites (~45 cm) recueillies lors de l'expédition ArcticNet de l'été 2019 à bord du NGCC Amundsen dans le bassin proximal aux glaciers Eugenie-Dobbin et à proximité de la marge Est du glacier Humboldt (Montero-Serrano et al., 2019). Cela permettra de documenter les processus glaciaires (ex. activité de vêlage d'icebergs) et sédimentaires opérant sur ces glaciers au cours du dernière millénaire, et donc de mieux comprendre l'effet des changements climatiques actuels et futurs sur ces glaciers.

ANNEXES

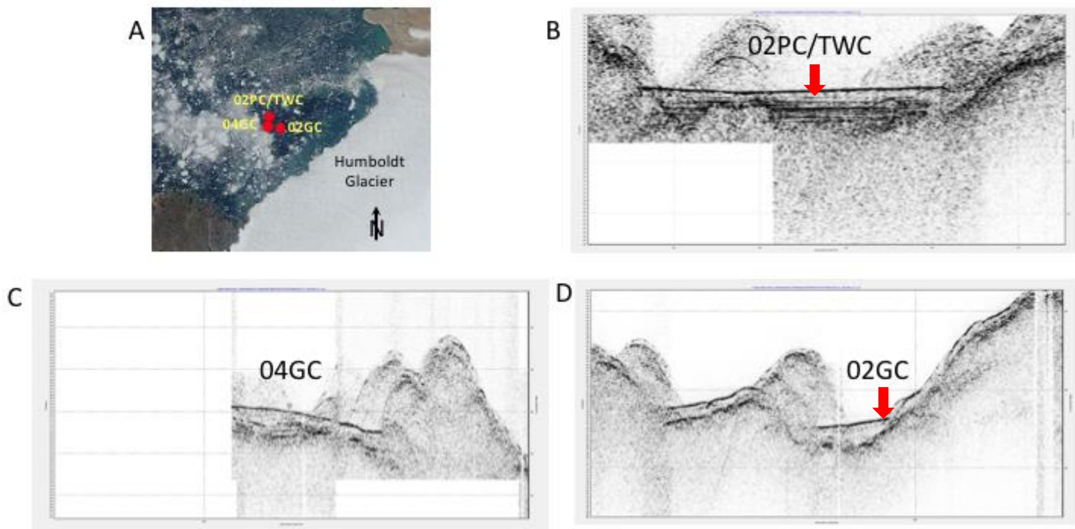

Fig. S1. (A) MODIS satellite image from 14 August 2019 showing a snapshot of Humboldt Glacier (source: NASA Worldview), as well as the location of the cores in this study. (B-D) Sub-bottom profiles (3.5 kHz) across coring stations.

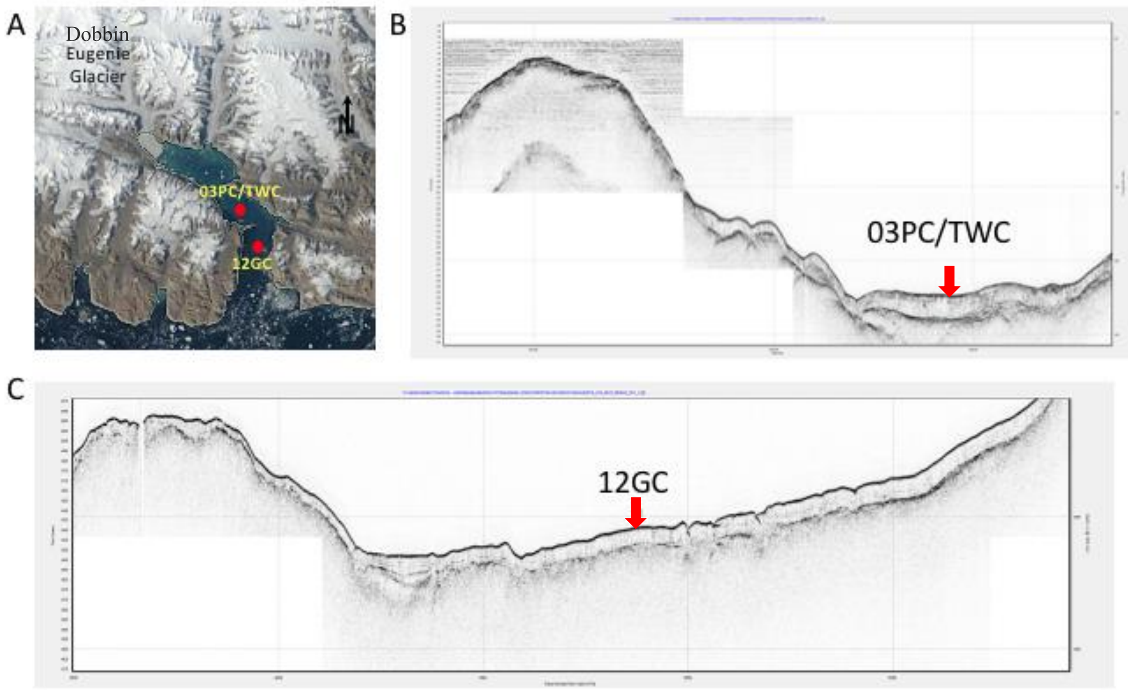

Fig. S2. (A) MODIS satellite image from 14 August 2019 showing a snapshot of Eugenie-Dobbin Glaciers (source: NASA Worldview), as well as the location of the cores in this study. (B-C) Sub-bottom profiles (3.5 kHz) across coring stations.

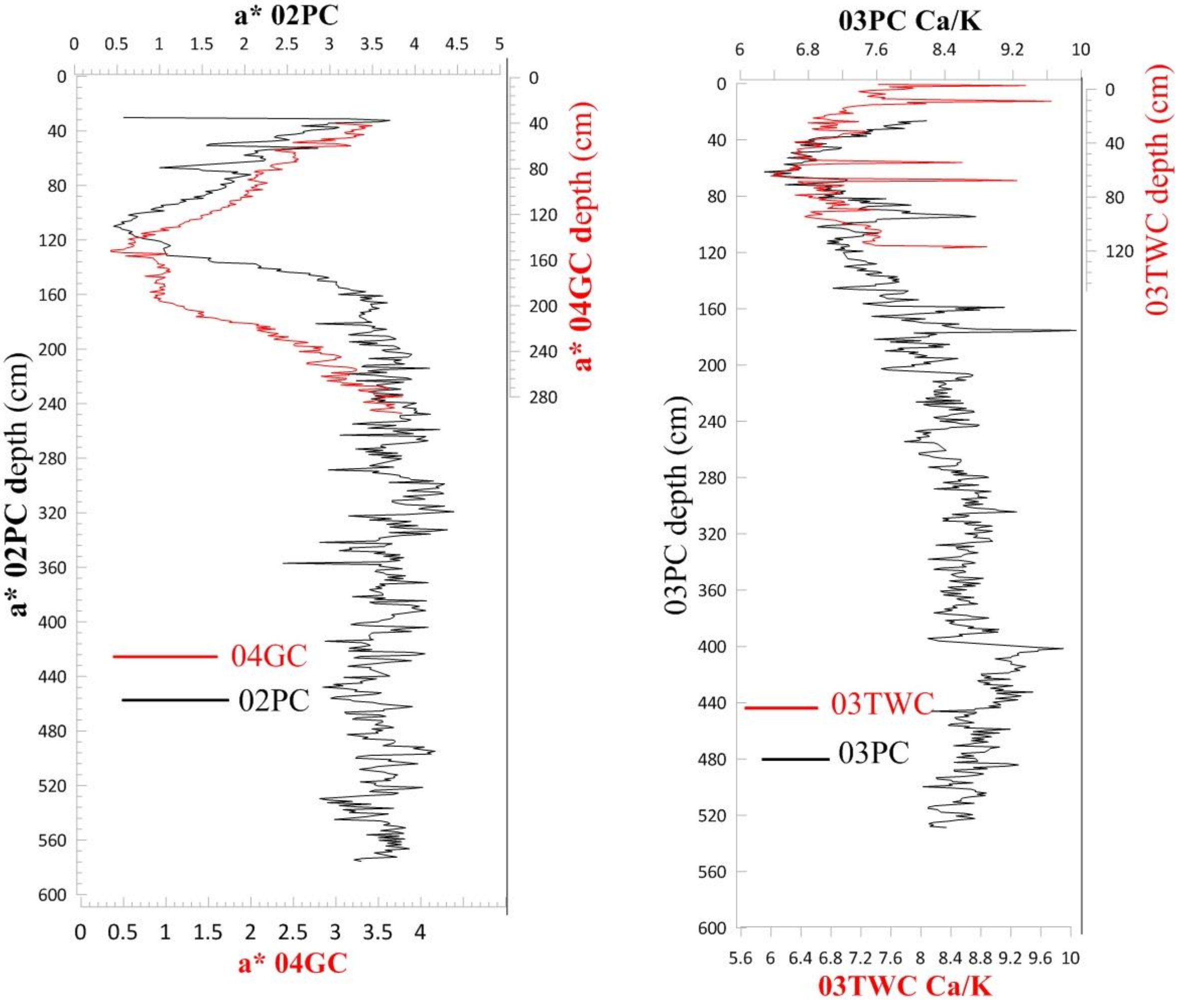

Fig. S3. Core top correlations of cores 04GC and 02PC and cores 03PC and 03TWC with the help of Ca/K and color reflectance parameter a* profiles, respectively. These correlations suggest that: i) approximately 2 cm and 8 cm of sediments at the top of cores 02PC and 03PC, respectively, were lost during piston coring; and ii) the uppermost parts of cores 02PC and 03PC show deformations at approximately 35 cm and 32 cm, respectively, which is related to the cumulative action of compaction and stretching during piston coring.

.

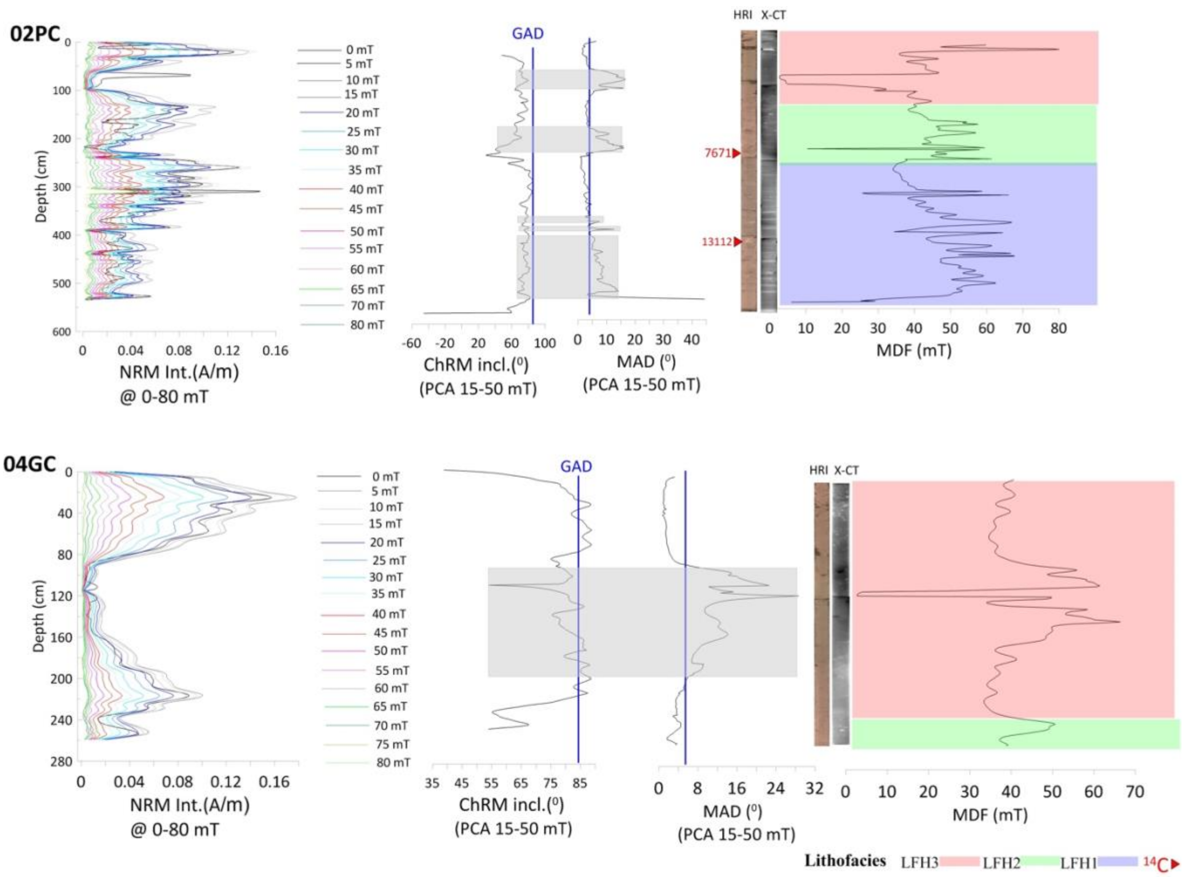

Fig. S4. Paleomagnetic results from cores 02PC and 04GC. From left to right: NRM intensities following AF demagnetization from 0 to 80 mT. ChRM inclination and MAD values calculated using a PCA over the 15-50 mT demagnetization range. ChRM inclinations often plot near the geocentric axial dipole (GAD) hypothesis predicted value (blue line). The vertical blue line delineates a MAD value of 5°. Unreliable intervals for paleomagnetic reconstruction are highlighted in gray. MDF_NRM values show variations between 30 and 80 mT in LFH1, LFH2 and the upper part of LFH3 in cores 02PC and 04GC, suggesting that a finer magnetic grain size predominates in these intervals (Stoner and St-Onge, 2007; St-Onge et St-Onge, 2014). Lower MDF_NRM values (<30 mT) are observed at the base of LFH3 in cores 02PC and 04GC, consistent with lower k_{LF} and a* values (Fig. 11), possibly indicating the presence of coarser magnetic grain sizes (Dankers, 1981). These coarser magnetic grains could have been transported by large meltwater episodes related to the landward retreat of the Humboldt glacier between ~3.7 and 0.3 cal ka BP.

Table. S1. Average mineralogical composition of the main sources used in the SedUnMix modeling.

Minerals	eastern Ellesmere Island (n=8)		Ellesmere-Inglefield mobile belt (n=11)		Nares Ice Stream (n=11)	
	Median	SD	Median	SD	Median	SD
Quartz	15.7	0.9	19.3	4.5	18.2	4.9
K-feldspar	4.4	0.7	15.3	1.0	7.0	1.2
Plagioclase	3.2	0.6	28.0	2.5	3.3	1.3
Calcite	21.4	1.2	0.1	0.2	12.6	5.1
Dolomite	16.8	2.6	1.9	0.4	7.6	1.7
Fe-bearing	0.6	0.2	1.0	0.5	0.5	0.6
Kaolinite	1.2	0.3	2.6	2.3	0.3	0.4
Illites	20.8	5.1	8.6	3.2	27.1	6.9
Chlorite&Biotite	7.9	1.7	11.6	2.9	10.3	1.7

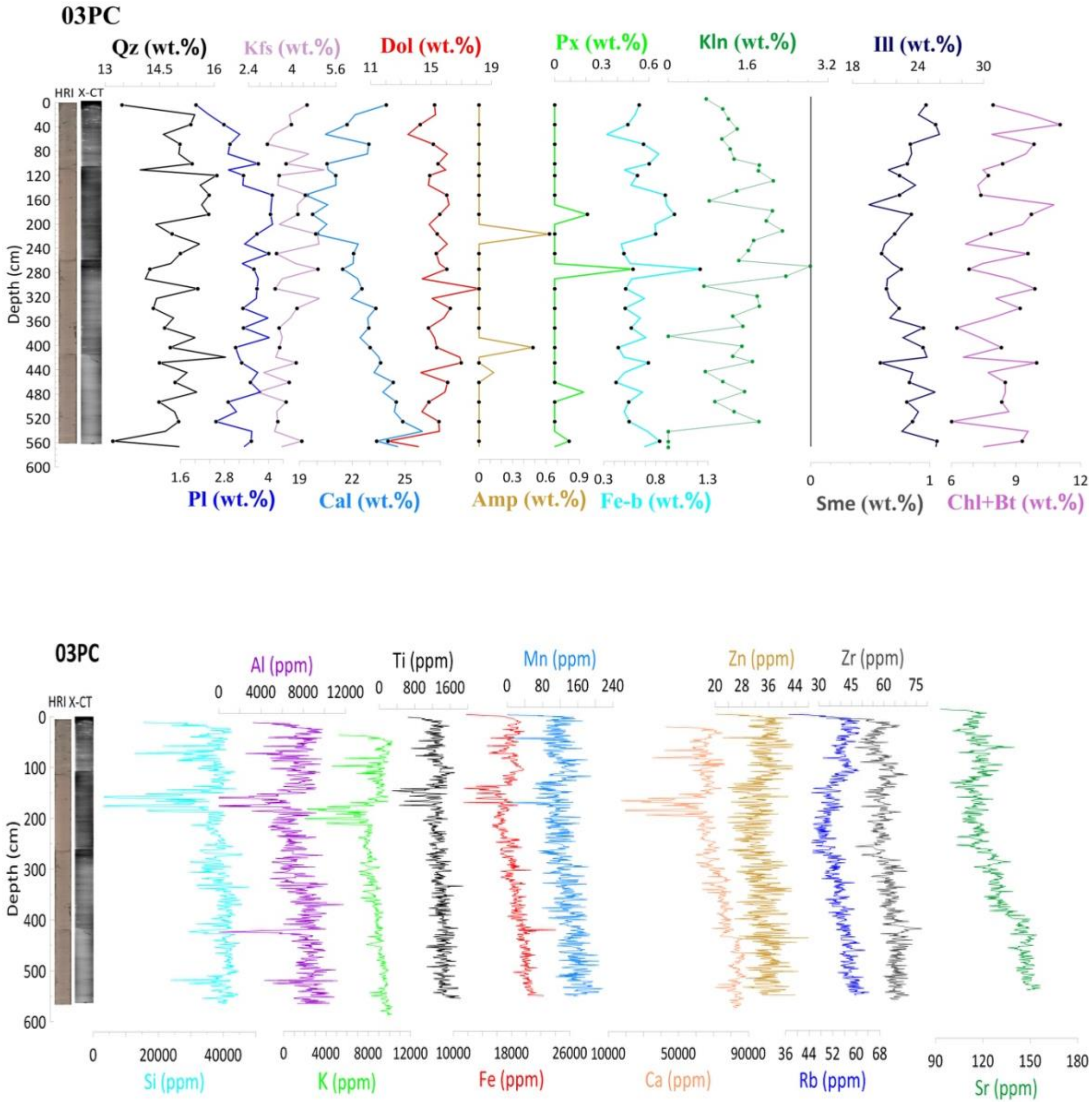

Fig. S5. Downcore mineralogical and geochemical variations in cores 03PC.

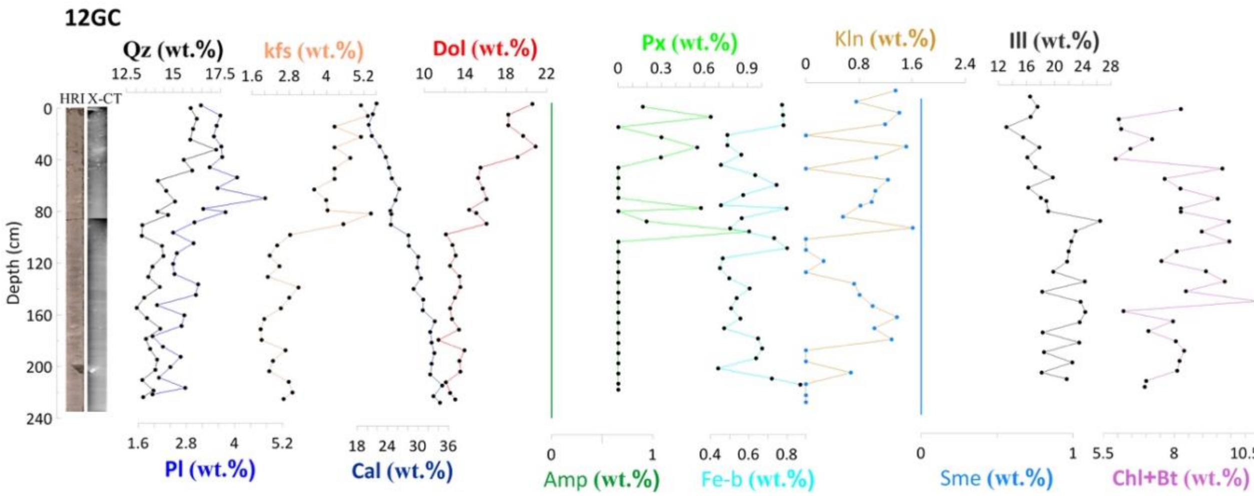

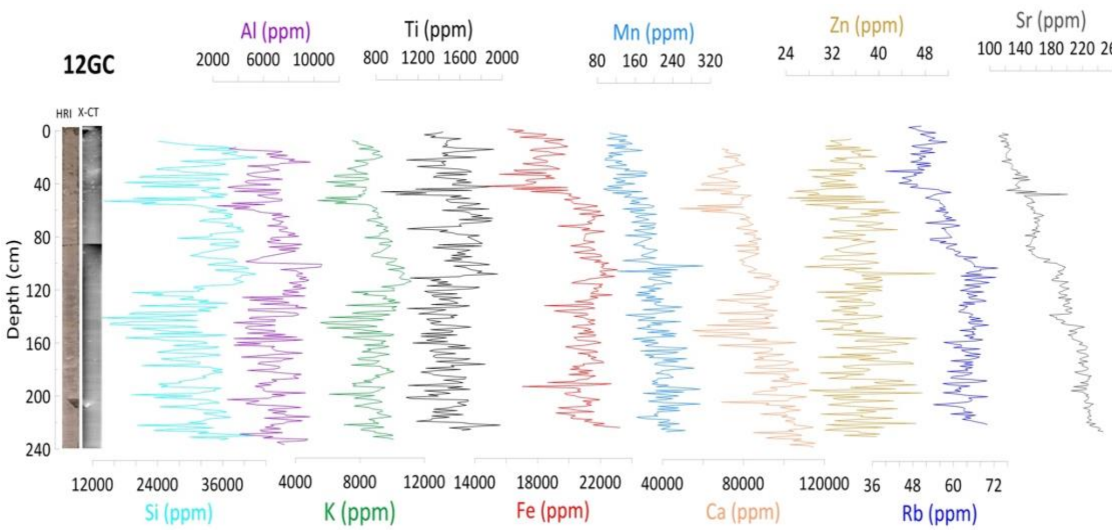

Fig. S6. Downcore mineralogical and geochemical variations in cores 12GC.

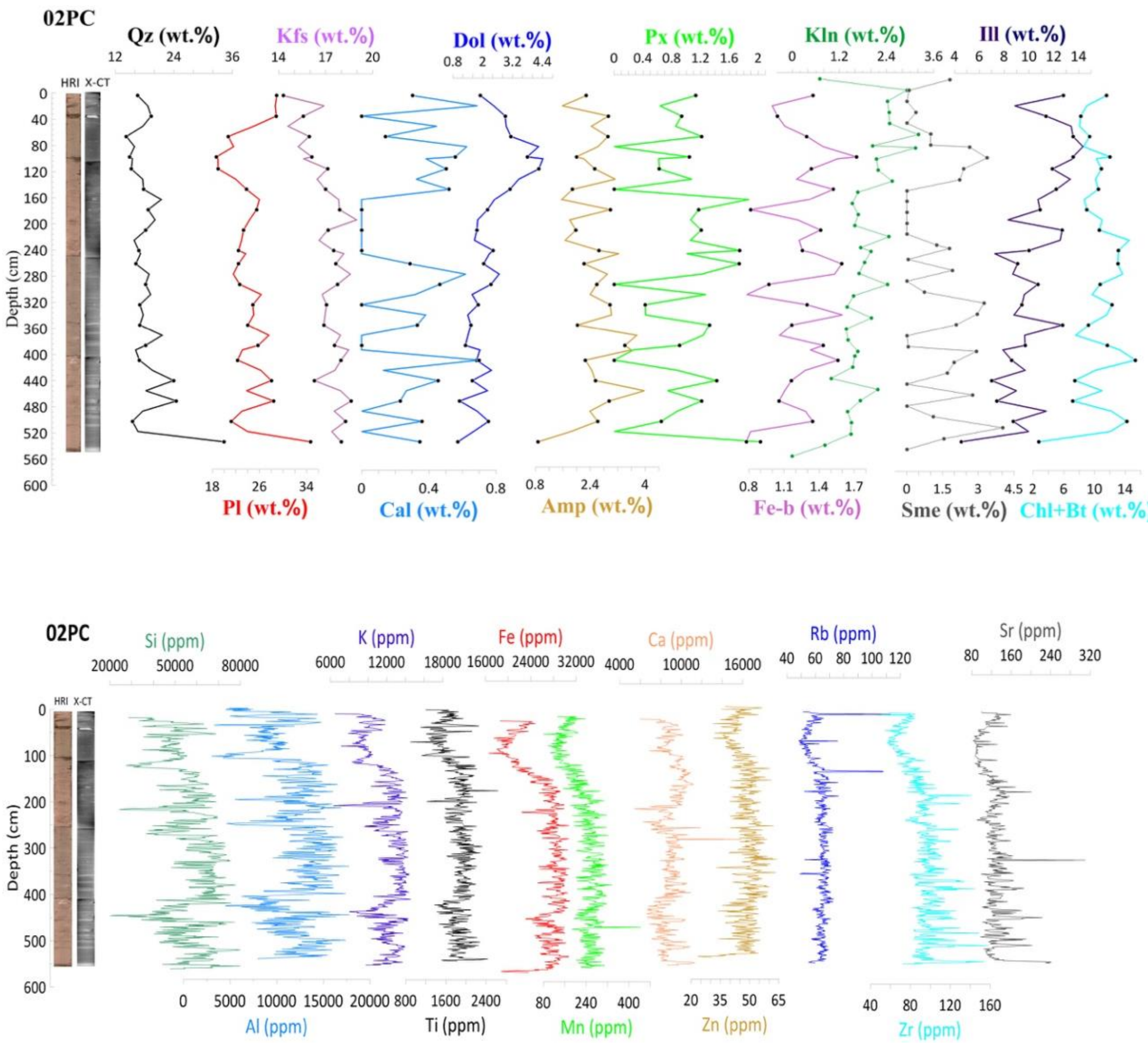

Fig. S7. Downcore mineralogical and geochemical variations in cores 02PC.

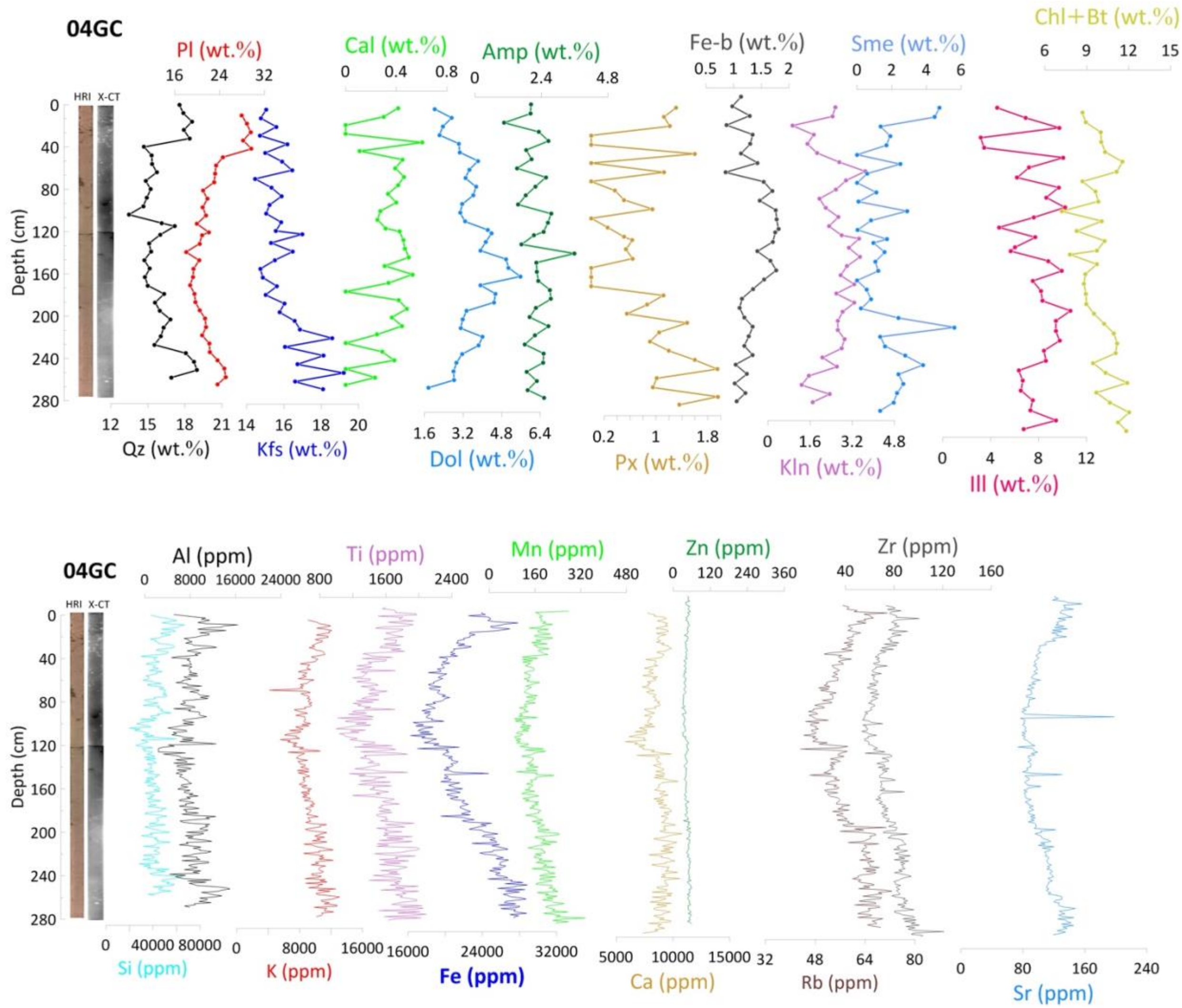

Fig. S8. Downcore mineralogical and geochemical variations in cores 04GC.

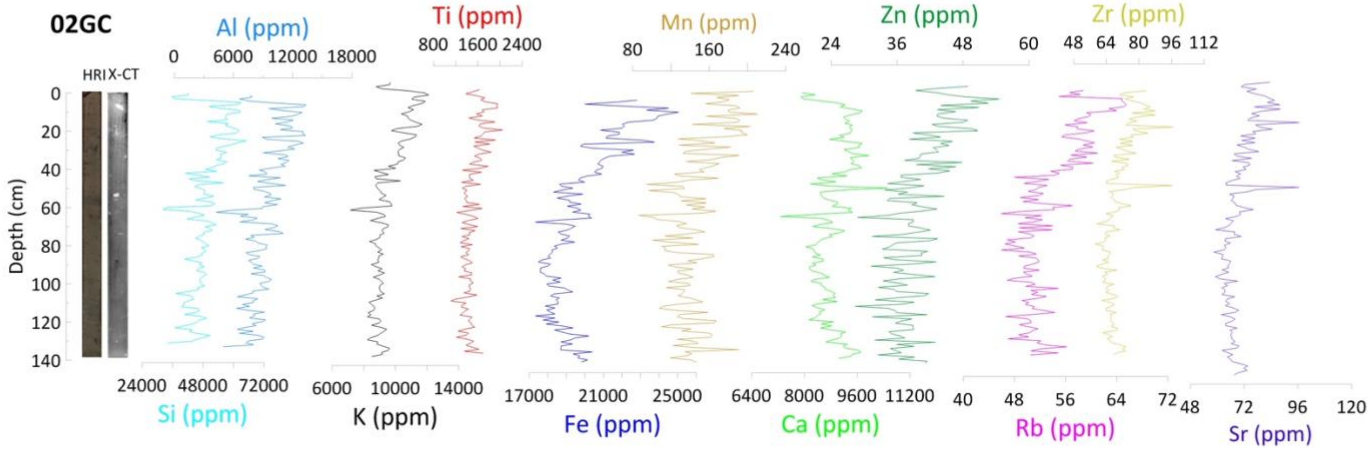

Fig. S9. Downcore geochemical variations in cores 02GC.

RÉFÉRENCES BIBLIOGRAPHIQUES

Adegbie, A. T., Schneider, R. R., Röhl, U., & Wefer, G. (2003). Glacial millennial-scale fluctuations in central African precipitation recorded in terrigenous sediment supply and freshwater signals offshore Cameroon. *Palaeogeography, Palaeoclimatology, Palaeoecology*, *197*(3-4), 323-333.

Aitchison, J. (1982). The statistical analysis of compositional data. *Journal of the Royal Statistical Society: Series B (Methodological)*, *44*(2), 139-160.

Aitchison, J. (1986). A classification as a source for a thesaurus: The Bibliographic Classification of HE Bliss as a source of thesaurus terms and structure. *Journal of documentation*.

Aitchison, J. (1990). Relative variation diagrams for describing patterns of compositional variability. Mathematical Geology, 22(4), 487–511.

Aksu, A. E., and Piper, D. J. (1987). Late quaternary sedimentation in Baffin Bay. *Canadian Journal of Earth Sciences*, *24*(9), 1833-1846.

Al-Mufti, O. N., Arnott, R. W. C., Hinton, M. J., Alpay, S., and Russell, H. A. (2022). Using computed tomography (CT) to reconstruct depositional processes and products in the subaqueous glaciogenic Champlain Sea basin, Ottawa, Canada. *Geomorphology*, *403*, 108165.

Andrews, J. T. (2000). Icebergs and Iceberg Rafted Detritus (IRD) in the North Atlantic: facts and assumptions. Oceanography. 13: 100–108.

Andrews, J. T. & Eberl, D. (2012). Determination of sediment provenance by unmixing the mineralogy of source-area sediments: the 'SedUnMix' program. Marine Geology. 291–294: 24–33.

Andrews, J. T., Bjork, A. A., Eberl, D. D., Jennings, A. E. & Verplanck, E. P. (2015). Significant differences in late Quaternary bedrock erosion and transport: east versus West Greenland~70^{o}N- evidence from the mineralogy of offshore glacial marine sediments. Journal of Quaternary Science. 30: 452–463.

Andrews, J. T., Klein, A. J., Jenner, K. A., Jennings, A. E. & Campbell, C. (2018). The variability of Baffin Bay seafloor sediment mineralogy: the identification of discrete glacial sediment sources and application to Late Quaternary downcore analysis. Canadian Journal of Earth Sciences. 55: 620-639.

Barber, D. C., Dyke, A., Hillaire-Marcel, C., Jennings, A. E., Andrews, J. T., Kerwin, M. W., & Gagnon, J. M. (1999). « Forcing of the cold event of 8,200 years ago by catastrophic drainage of Laurentide lakes ». *Nature*, 400(6742), 344.

Berger, A.& Loutre, M.F. (1991). Insolation values for the climate of the last 10 million years. Quaternary Science Reviews 10, 297–317.

Bennike, O., & Björck, S. (2002). Chronology of the last recession of the Greenland Ice Sheet. *Journal of Quaternary Science 17(3)*, 211-219.

Buizert, C., Sigl, M., Severi, M., Markle, B. R., Wettstein, J. J., McConnell, J. R., & Steig, E. J. (2018). Abrupt ice-age shifts in southern westerly winds and Antarctic climate forced from the north. *Nature*, *563*(7733), 681-685.

Blake, J.W. (1992). Shell-bearing till along Smith Sound, Ellesmere Island-Greenland: age and significance. Sveriges Geologiska Undersökning 81, 51–58.

Butler, B. M. & Hillier, S. (2020). PowdR: An R package for quantitative mineralogy using full pattern summation of X-ray powder diffraction data. Computers & Geosciences. 104662. https://doi.org/10.1016/j.cageo.2020.104662.

Bradley, R. S., Hughes, M. K., & Diaz, H. F. (2003). Climate in medieval time. *Science*, *302*(5644), 404-405.

Brice C., Montero Serrano J.-C., St-Louis R. (2022). Geochemical baseline of major and trace elements in sediments from the Canadian Arctic Archipelago. ArcTrain Annual Meeting, May 4-6, Jouvence, Canada.

Blaauw, M., & Christen, J. A. (2011). Flexible paleoclimate age-depth models using an autoregressive gamma process.

Blake, J.W. (1993). Holocene emergence along the Ellesmere Island coasts of northernmost Baffin Bay. Norsk Geologisk Tidsskrift 73, 147–160.

Blott, S. J., & Pye, K. (2001). GRADISTAT: a grain size distribution and statistics package for the analysis of unconsolidated sediments. *Earth surface processes and Landforms*, *26*(11), 1237-1248.

Briner, J. P., Håkansson, L., & Bennike, O. (2013). The deglaciation and neoglaciation of Upernavik Isstrøm, Greenland. *Quaternary Research* 80(3), 459-467.

Brossard, J. (2021): Dynamique s´sédimentaire holocène dans le détroit de Jones reconstituée à partir des carottes sédimentaires recueillies dans la baie de Belcher (calotte glaciaire de Devon, Nunavut, Canada). Mémoire. Rimouski, Québec, Université du Québec à Rimouski, Institut des sciences de la mer de Rimouski (ISMER), 116 pp.

Caron M., St-Onge G., Montero-Serrano J.C., *et al.* (2018). Holocene chronostratigraphy of northeastern Baffin Bay based on radiocarbon and paleomagnetic data. *Boreas*.

Caron, M., Rochon, A., Montero-Serrano, J. C. & St-Onge, G. (2019). Evolution of sea-surface conditions on the northwestern Greenland margin during the Holocene. Journal of Quaternary Science. 34: 569–580.

Caron, M., Montero-Serrano, J. C., St-Onge, G., & Rochon, A. (2020). Quantifying provenance and transport pathways of Holocene sediments from the northwestern Greenland margin. *Paleoceanography and Paleoclimatology*, *35*(5), e2019PA003809.

Ciracì, E., Velicogna, I. & Swenson, S. (2020). Continuity of the mass loss of the world's glaciers and ice caps from the GRACE and GRACE Follow-On missions. Geophysical Research Letters. 47: e2019GL086926. doi:10.1029/2019GL086926.

Cook, A. J., Copland, L., Noël, B. P., Stokes, C. R., Bentley, M. J., Sharp, M. J., & van den Broeke, M. R. (2019). Atmospheric forcing of rapid marine-terminating glacier retreat in the Canadian Arctic Archipelago. *Science Advances*, *5*(3), eaau8507.

Crespin, E., H. Goosse, T. Fichefet, and M. E. Mann. (2009). The 15th century Arctic warming in coupled model simulations with data assimilation. Clim. Past 5: 389-401.

Croudace, I. W. & Rothwell, R. G. (2015). Micro-XRF Studies of Sediment Cores: Applications of a Non-Destructive Tool for the Environmental Sciences. 421 pp. Springer, Dordrecht.

Dankers, P., 1981. Relationship between median destructive field and remanent coercive forces for dispersed natural magnetite, titanomagnetite and hematite. Geophysical Journal International 64, 447–461. https://doi.org/10.1111/j.1365-246X.1981.tb02676.x

Dalton, A. S., Margold, M., Stokes, C. R., Tarasov, L., Dyke, A. S., Adams, R. S.,& Wright Jr, H. E. (2020). An updated radiocarbon-based ice margin chronology for the last deglaciation of the North American Ice Sheet Complex. *Quaternary Science Reviews*, *234*, 106223.

Dawes, P. R. (1997). The proterozoic thule supergroup, Greenland, and Canada: history, lithostratigraphy and development. *Geology of Greenland Survey Bulletin*, *174*, 1-150.

Dawes, P. R. (2004). Explanatory notes to the geological map of Greenland, 1: 500 000, Humboldt Gletscher, Sheet 6. *Geological Survey of Denmark and Greenland Map Series*, *1*, 1-48. https://doi.org/10.34194/geusm.v1.4615.

Dawes, P. R. (2006). Explanatory notes to the Geological map of Greenland, 1: 500 000, Thule, Sheet 5. *Geological Survey of Denmark and Greenland Map Series*, *2*, 1-100. https://doi.org/10.34194/geusm.v2.4614.

Debret, M., Sebag, D., Desmet, M., Balsam, W., Copard, Y., Mourier, B., & Winiarski, T. (2011). Spectrocolorimetric interpretation of sedimentary dynamics: The new “Q7/4 diagram”. *Earth-Science Reviews*, *109*(1-2), 1-19.

Deschamps, C.-E., J.-C. Montero-Serrano, and G. St-Onge. (2018a). Sediment Provenance Changes in the Western Arctic Ocean in Response to Ice Rafting, Sea Level, and Oceanic Circulation Variations Since the Last Deglaciation. Geochemistry, Geophysics, Geosystems 19: 2147-2165.

Deschamps, C.-E., G. St-Onge, J.-C. Montero-Serrano, and L. Polyak. (2018b). Chronostratigraphy and spatial distribution of magnetic sediments in the Chukchi and Beaufort seas since the last deglaciation. Boreas 47: 544-564.

Dowdeswell, J. A., Hogan, K. A., Arnold, N. S., Mugford, R. I., Wells, M., Hirst, J. P. P. & Decalf, C. (2015). Sediment-rich meltwater plumes and ice-proximal fans at the margins of modern and ancient tidewater glaciers: Observations and modelling. Sedimentology. 62: 1665-1692.

Dyke, A. S. (1998). Holocene delevelling of Devon Island, Arctic Canada: implications for ice sheet geometry and crustal response. Canadian Journal of Earth Sciences 35: 885-904.

Dyke, A. S., J. T. Andrews, P. U. Clark, J. H. England, G. H. Miller, J. Shaw, and J. J. Veillette. (2002). The Laurentide and Innuitian ice sheets during the Last Glacial Maximum. Quaternary Science Reviews 21: 9-31.

Dyke, A. S. (2004). « An outline of North American deglaciation with emphasis on central and northern Canada ». In: *Developments in Quaternary Sciences,* Vol. 2, pp. 373-424. Elsevier.

Dyke, A. S., Savelle, J. M., Szpak, P., Southon, J. R., Howse, L., Desrosiers, P. M. & Kotar, K. (2019). An assessment of marine reservoir corrections for radiocarbon dates on walrus from the Foxe basin region of Arctic Canada. Radiocarbon 61, 67–81.

Eberl, D. D. (2003). User Guide to RockJock - A Program for Determining Quantitative Mineralogy from X-Ray Diffraction Data. Open-File Report.

England, J. (1999) « Coalescent Greenland and Innuitian ice during the last glacial maximum: revising the Quaternary of the Canadian High Arctic ». *Quaternary Science Reviews*, 18(3), 421-456.

England, J. (1996). Glacier dynamics and paleoclimatic change during the last glaciation of eastern Ellesmere Island, Canada. Canadian Journal of Earth Sciences. 33(5): 779-799. https://doi-org.ezproxy.uqar.ca/10.1139/e96-060

Shroyer, E. L., Padman, L., Samelson, R. M., Münchow, A., & Stearns, L. A. (2017). Seasonal control of Petermann Gletscher iceshelf melt by the ocean's response to sea-ice cover in Nares Strait. *Journal of Glaciology*, *63*(238), 324-330.

Shroyer, E. L., R. M. Samelson,L. Padman, and A. Münchow (2015),Modeled ocean circulation in NaresStrait and its dependence on landfast-ice cover,J. Geophys. Res. Oceans,120,7934–7959, https://doi.org/10.1002/2015JC011091.

Stoner, J.S., St-Onge, G., 2007. Chapter Three Magnetic Stratigraphy in Paleoceanography: Reversals, Excursions, Paleointensity, and Secular Variation, in: Hillaire–Marcel, C., De Vernal, A. (Eds.), Developments in Marine Geology. Elsevier, pp. 99–138. https://doi.org/10.1016/S1572-5480(07)01008-1

St-Onge, M.-P. and St-Onge, G. (2014). Environmental changes in Baffin Bay during the Holocene based on the physical and magnetic properties of sediment cores. J. Quaternary Sci., 29: 41-56. https://doi.org/10.1002/jqs.2674.

England, J., N. Atkinson, J. Bednarski, A. S. Dyke, D. A. Hodgson, and C. Ó Cofaigh. (2006). The Innuitian Ice Sheet: configuration, dynamics, and chronology. QuaternaryScience Reviews 25: 689-703.

Lacourse, T. & Gajewski, K. (2020). Current practices in building and reporting age–depth models. Quaternary Research 96, 28–38.

Laskar, J., P. Robutel, F. Joutel, M. Gastineau, A.C.M. Correia, and B. Levrard. (2004). A long-term numerical solution for the insolation quantities of the Earth. Astronomy& Astrophysics 428:261-285.

Lenaerts, J. T., van Angelen, J. H., van den Broeke, M. R., Gardner, A. S., Wouters, B., & van Meijgaard, E. (2013). Irreversible mass loss of Canadian Arctic Archipelago glaciers. *Geophysical Research Letters*, *40*(5), 870-874.

Fisher, D., J. Zheng, D. Burgess, C. Zdanowicz, C. Kinnard, M. Sharp, and J. Bourgeois. (2012). Recent melt rates of Canadian arctic ice caps are the highest in four millennia.Global and Planetary Change 84-85: 3-7

Funder, S. (1990). Late Quaternary stratigraphy and glaciology in the Thule area, Northwest Greenland (Vol. 22). Museum Tusculanum Press.

Funder, S., Kjeldsen, K.K., Kjær, K.H., Ó Cofaigh, C., (2011). The Greenland Ice Sheet During the Past 300,000 Years: A Review. *Dev. Quat. Sci.* 15, 699–713.

Georgiadis, E., Giraudeau, J., Jennings, A., Limoges, A. & Jackson, R. (2020). Local and regional controls on Holocene Sea ice dynamics and oceanography in Nares Strait, Northwest Greenland. Marine Geology. 422. https://doi.org/10.1016/j.margeo.2020.106115. hal-02991666.

Georgiadis, E., Giraudeau, J., Martinez, P., Lajeunesse, P., St-Onge, G., Schmidt, S. & Mass E. G. (2018). Deglacial to postglacial history of Nares Strait, Northwest Greenland: a marine perspective from Kane Basin. Climate of the Past. 14: 1991–2010.

Grobe, H. (1987). A simple method for the determination of ice-rafted debris in sediment cores. Polarforschung. 57: 123–126.

Hansen, K. E., Giraudeau, J., Wacker, L., Pearce, C. & Seidenkrantz, M.-S. (2020). Reconstruction of Holocene oceanographic conditions in Eastern Baffin Bay. Climate of the Past 16, 1075–1095.

Harrison, J. C., T. A. Brent, and G. N. Oakey. (2011). Chapter 40 Baffin Fan and its inverted rift system of Arctic eastern Canada: stratigraphy, tectonics, and petroleum resource potential. Geological Society, London, Memoirs 35: 595-626.

Heaton, T.J., Köhler, P., Butzin, M., Bard, E., Reimer, R.W., Austin, W.E.N. et al. (2020) Marine20—the marine radiocarbon age calibration curve (0–55,000 cal BP). Radiocarbon, 62(4), 779–820.

Hesse, R., Klaucke, I., Ryan, W. B., & Piper, D. J. (1997). Ice-sheet sourced juxtaposed turbidite systems in Labrador Sea. *Geoscience Canada*.

Hillebrand, T. R., Hoffman, M. J., Perego, M., Price, S. F., & Howat, I. M. (2022). The contribution of Humboldt Glacier, northern Greenland, to sea-level rise through 2100 constrained by recent observations of speedup and retreat. *The Cryosphere*, *16*(11), 4679-4700.

Hiscott, R., A. E. Aksu, and O. Nielsen. (1989). Provenance and Dispersal Patterns, Pliocene-Pleistocene Section at Site 645, Baffin Bay. Proc., scientific results, ODP, Leg 105, Baffin Bay, and Labrador Sea: 31-52.

Hodson, D. L. R., Keeley, S. P. E.,West, A., Ridley, J., Hawkins, E. & Hewitt, H.T. (2013). Identifying uncertainties in Arctic climate change projections. Climate Dynamics 40, 2849–2865.

Hogan, K. A., Jakobsson, M., Mayer, L., Reilly, B. T., Jennings, A. E., Stoner, J. S., Nielsen, T., Andresen, K. J., Nørmark, E., Heirman, K. A., Kamla, E., Jerram, K., Stranne, C. & Mix, A. (2020). Glacial sedimentation, fluxes and erosion rates associated with ice retreat in Petermann Fjord and Nares Strait, north-west Greenland. The Cryosphere 14, 261–286.

Jackson, R., Kvorning, A. B., Limoges, A., Georgiadis, E., Olsen, S. M., Tallberg, P., & Ribeiro, S. (2021). Holocene polynya dynamics and their interaction with oceanic heat transport in northernmost Baffin Bay. *Scientific Reports*, *11*(1), 10095.

Jakobsson, M., Hogan, K. A., Mayer, L. A., Mix, A., Jennings, A., Stoner, J., & Stranne, C. (2018). The Holocene retreat dynamics and stability of Petermann Glacier in northwest Greenland. *Nature communications*, *9*(1), 2104.

Jennings, A. E., C. Sheldon, T. M. Cronin, P. Francus, J. Stoner, and J. Andrews. (2011). TheHolocene history of Nares strait Transition from Glacial Bay to Arctic-Atlantic Throughflow. Oceanography 24: 26-41.

Jennings, A. E., Campbell, D. C. & Piper, D. J. W. (2018). Along-slope variations in sediment lithofacies and depositional processes since the Last Glacial Maximum on the northeast Baffin margin, Canada. Marine Geology. 405: 92-107.

Jennings, A. E., Andrews, J.T., Oliver, B., Walczak, M. & Mix, A. (2019). Retreat of the smith sound ice stream in the early Holocene. Boreas. 48: 825–840.

Jennings, A., Reilly, B., Andrews, J., Hogan, K., Walczak, M., Jakobsson, M., Stoner, J., Mix, A., Nichols, K. W., O'Regan, M., Prins, M. A., and Troelstra, S. R., (2022). Modern and Early Holocene ice shelf sediment facies from Petermann Fjord and northern Nares Strait, Northwest Greenland. Quaternary Science Reviews, 283. https://doi.org/10.1016/j.quascirev.2022.107460.

Jombart, T. (2008). Adegenet: A R package for the multivariate analysis of genetic markers. Bioinformatics, 24(11), 1403–1405.

Jones, P.D. & Mann, M. E. (2004). Climate over past millennia. Review of Geophysics. 42: RG2002. https://doi.org/10.1029/2003RG000143.

Kalenitchenko, D., Joli, N., Potvin, M., Tremblay, J. É., & Lovejoy, C. (2019). Biodiversity and species change in the Arctic Ocean: A view through the lens of Nares Strait. *Frontiers in Marine Science*, *6*, 479.

Kassambara, A. and Mundt, F. (2020). Factoextra: Extract and Visualize the Results of Multivariate Data Analyses. R Package Version 1.0.7. https://CRAN.R project.org/package=factoextra.

Kaufman, D. S., D. P. Schneider, N. P. McKay, C. M. Ammann, R. S. Bradley, K. R.Briffa, G. H. Miller, B. L. Otto-Bliesner, J. T. Overpeck, and B. M. Vinther. (2009). Recent warming reverses long-term arctic cooling. Science 325: 1236-1239.

Kirschvink, J. L. (1980). The least-squares line and plane and the analysis of palaeomagnetic data. Geophysical Journal International 62: 699-718.

Kerr, J. W. (1967). New nomenclature for ordovician rock units of th e eastern and southern queen Elizabeth Islands, Arctic Canada. *Bulletin of Canadian Petroleum Geology*, *15*(1), 91-113.

Kerr, J. W. (1970). Geology of outstanding arctic aerial photographs: 1. Cape Storm Area, Southern Ellesmere Island. *Bulletin of Canadian Petroleum Geology*, *18*(4), 463-468.

Kinnard, C., Zdanowicz, C. M., Fisher, D. A., Isaksson, E., de Vernal, A., & Thompson, L. G. (2011). Reconstructed changes in Arctic Sea ice over the past 1,450 years. *Nature*, *479*(7374), 509-512.

Kliem, N., & Greenberg, D.A. (2003). Diagnostic simulations of the summer circulation in the Canadian Arctic Archipelago. *Atmosphere-Ocean, 41*, 273 - 289.

Knudsen, K. L., B. Stabell, M.-S. Seidenkrantz, J. EirÍKsson, and W. Blake. (2008). Deglacial and Holocene conditions in northernmost Baffin Bay: sediments, foraminifera, diatoms, and stable isotopes. Boreas 37: 346-376.

Koerner, K. A., Limoges, A., Van Nieuwenhove, N., Richerol, T., Massé, G., & Ribeiro, S. (2021). Late Holocene sea-surface changes in the North Water polynya reveal freshening of northern Baffin Bay in the 21st century. *Global and Planetary Change*, *206*, 103642.

Kravitz, J.H. (1976). Textural and Mineralogical Characteristics of the Surficial Sediments of Kane Basin. *Journal of Sedimentary Research*, *46*, 710-725.

Kwok, R., Spreen, G., & Pang, S. (2013). Arctic sea ice circulation and drift speed: Decadal trends and ocean currents. *Journal of Geophysical Research: Oceans*, *118*(5), 2408-2425.

Lecavalier, B. S., Fisher, D. A., Milne, G. A., Vinther, B. M., Tarasov, L., Huybrechts, P., Lacelle, D., Main, B., Zheng, J., Bourgeois, J. & Dyke, A. S. (2017). High ArcticHolocene temperature record from the Agassiz ice cap and Greenland ice sheet evolution. PNAS. 114: 5952–5957.

Ledu, D., A. Rochon, A. de Vernal, and G. St-Onge. (2010). Holocene paleoceanography of the northwest passage, Canadian Arctic Archipelago. Quaternary Science Reviews 29: 3468-3488.

Lenaerts, J. T., van Angelen, J. H., van den Broeke, M. R., Gardner, A. S., Wouters, B., & van Meijgaard, E. (2013). Irreversible mass loss of Canadian Arctic Archipelago glaciers. *Geophysical Research Letters*, *40*(5), 870-874.

Levac, E., De Vernal, A. & Blake, W. J. (2001). Sea-surface conditions in northernmost Baffin Bay during the Holocene: Palynological evidence. *Journal of Quaternary Science 16*, 353–363.

Lévesque, Y., St-Onge, G., Lajeunesse, P., Desiage, P.-A., Brouard, É. (2020). Defining the maximum extent of the Laurentide Ice Sheet in Home Bay cross-shelf trough duringthe Last glacial episode. Boreas 49, 52-70.

Lucchi, R. G., & Rebesco, M. (2007). Glacial contourites on the Antarctic Peninsula margin: insight for palaeoenvironmental and palaeoclimatic conditions. *Geological Society, London, Special Publications*, *276*(1), 111-127.

MacGregor, J. A., Colgan, W. T., Fahnestock, M. A., Morlighem, M., Catania, G. A., Paden, J. D., & Gogineni, S. P. (2016). Holocene deceleration of the Greenland ice sheet. *Science*, *351*(6273), 590-593.

MacLean, B., Woodside, J. M., & Girouard, P. (1984). Geological and geophysical investigations in Jones Sound, District of Franklin. *Current Res. Part A, Geol. Surv. Canada, Paper*, 359-365.

Mazaud, A. (2005): User-friendly software for vector analysis of the magnetization of long sediment cores. Geochemistry, Geophysics, Geosystems 6: Q12006.

McNeely, R., Dyke, A.S., Southon, J., (2006). Canadian Marine Reservoir Ages: PreliminaryData Assessment. Geological Survey of Canada. Open File 5049.

Melling, H., Y. Gratton and G. Ingram. (2001). Ocean circulation within the North Water polynya of Baffin Bay. Atmos. Oceans, 39, 301–325.

Millan, R., Mouginot, J., & Rignot, E. (2017). Mass budget of the glaciers and ice caps of the Queen Elizabeth Islands, Canada, from 1991 to 2015. *Environmental Research Letters*, *12*(2), 024016.

Montero-Serrano, J. C., V. Bout-Roumazeilles, T. Sionneau, N. Tribovillard, A. Bory, B. P.Flower, A. Riboulleau, P. Martinez, and I. Billy. (2010). Changes in precipitation regimes over North America during the Holocene as recorded by mineralogy and geochemistry of Gulf of Mexico sediments. Global and Planetary Change 74: 132-143.

Montero-Serrano, J.-C., K. B. Föllmi, T. Adatte, J. E. Spangenberg, N. Tribovillard, A. Fantasia, and G. Suan. (2015). Continental weathering and redox conditions during the early Toarcian Oceanic Anoxic Event in the northwestern Tethys: Insight from the Posidonia Shale section in the Swiss Jura Mountains. Palaeogeography, Palaeoclimatology, Palaeoecology 429: 83-99.

Montero-Serrano, J. C., Brossard, J. & Corminboeuf, A. (2019). Collecting sedimentary sequences and plankton samples in the continental margins from the eastern Canadian Arctic Archipelago. ArcticNet Leg 2b Cruise Report – CCGS Amundsen (25 July to 15 August 2019).

Mortimer, A. & Sharp, M. (2018). Spatiotemporal variability of Canadian High Arctic glacier surface albedo from MODIS data, 2001–2016. The Cryosphere. 12: 701–720. doi:10.5194/tc-12-701-2018.

Morlighem, M., Williams, C. N., Rignot, E., An, L., Arndt, J. E., Bamber, J. L., Zinglersen, K. B. (2017). Bed Machine v3: Complete bed topography and ocean bathymetry mapping of Greenland from multibeam echo sounding combined with mass conservation. Geophysical Research Letters, 44, 11,051–11,061. https://doi.org/10.1002/2017GL074954

Mouginot, J., Rignot, E., Bjørk, A. A., van den Broeke, M., Millan, R., Morlighem, M., & Wood, M. (2019, May 7). Forty-six years of Greenland Ice Sheet mass balance from 1972 to 2018. Proceedings of the National Academy of Sciences of the United States of America. National Academy of Sciences. https://doi.org/10.1073/pnas.1904242116.

Mulder, T., Syvitski, J. P., Migeon, S., Faugeres, J.C.&Savoye, B. (2003). Marine hyperpycnal flows: initiation, behavior, and related deposits. Marine and Petroleum Geology 20, 861–882.

Münchow, A., Falkner, K. K., & Melling, H. (2007). « Spatial continuity of measured seawater and tracer fluxes through Nares Strait, a dynamically wide channel bordering the Canadian Archipelago ». *Journal of Marine Research*, 65(6), 759-788.

Münchow A., Padman, L., & Fricker, H. (2014). Interannual changes of the floating ice shelf of Petermann Gletscher, North Greenland, from 2000 to 2012. Journal of Glaciology, 60(221),489-499. https://doi.org:/10.3189/2014JoG13J135.

Ono, J., Watanabe, M., Komuro, Y., Tatebe, H., & Abe, M. (2022). Enhanced Arctic warming amplification revealed in a low-emission scenario. *Communications Earth & Environment*, *3*(1), 27.

O'Cofaigh, C., Andrews, J.T., Jennings, A.E., Dowdeswell, J.A., Hogan, K.A., Kilfeather, A.A. & Sheldon, C. (2013). Glacimarine lithofacies, provenance and depositional processes on a West Greenland trough-mouth fan. J. Quat. Sci. 28: 13-26.

O'Regan, M., Cronin, T. M., Reilly, B., Alstrup, A. K. O., Gemery, L., Golub, A., & Jakobsson, M. (2021). The Holocene dynamics of Ryder Glacier and ice tongue in north Greenland. *The Cryosphere*, *15*(8), 4073-4097.

Pieńkowski, A. J., Husum, K., Furze, M. F., Missana, A. F., Irvalı, N., Divine, D. V., & Eilertsen, V. T. (2022). Revised ΔR values for the Barents Sea and its archipelagos as a pre-requisite for accurate and robust marine-based 14C chronologies. Quaternary Geochronology, 68, 101244.

Powell, R. D. (1981). A Model for Sedimentation by Tidewater Glaciers. Annals of Glaciology 2: 129-134.

Rabe, B., Johnson, H. L., Münchow, A. Melling, H. (2012). Geostrophic ocean currents and freshwater fluxes across the Canadian polar shelf via Nares Strait. J. Mar. Res. 70, 603–640.

Rabe, B., M. Karcher, F.Kauker, U.Schauer, J. M. Toole, R. A. Krish-field, S. Pisarev, T. Kikuchi, and J. Su (2014). Arctic Ocean basin liquid freshwater storage trend 1992–2012, Geophys. Res. Lett.,41, 961–968. https://doi.org/:10.1002/2013GL058121.

Rantanen, M., Karpechko, A.Y., Lipponen, A. *et al.* The Arctic has warmed nearly four times faster than the globe since 1979. *Commun Earth Environ* **3**, 168 (2022). https://doi.org/10.1038/s43247-022-00498-3.

Reilly, B. T., Stoner, J. S., Mix, A. C., Walczak, M. H., Jennings, A., Jakobsson, M., & Cheseby, M. (2019). Holocene break-up and reestablishment of the Petermann Ice Tongue, Northwest Greenland. *Quaternary Science Reviews*, *218*, 322-342.

Reusche, M. M., Marcott, S. A., Ceperley, E. G., Barth, A. M., Brook, E. J., Mix, A. C., & Caffee, M. W. (2018). Early to late Holocene surface exposure ages from two marine-terminating outlet glaciers in northwest Greenland. *Geophysical Research Letters*, *45*(14), 7028-7039.

Ribeiro, S., Limoges, A., Massé, G., Johansen, K. L., Colgan, W., Weckström, K., & Davidson, T. A. (2021). Vulnerability of the North Water ecosystem to climate change. *Nature communications*, *12*(1), 4475.

Rignot, E., An, L., Chauche, N., Morlighem, M., Jeong, S., Wood, M., & Muenchow, A. (2021). Retreat of Humboldt Gletscher, North Greenland, driven by undercutting from a warmer ocean. *Geophysical research letters*, *48*(6), e2020GL091342.

Robertson, S. (1999). *Holocene deglacial and sea level history of dobbin bay, eastern Ellesmere Island, Arctic Canada*. PhD thesis. University of Alberta, Department of Earth and Atmospheric Sciences, Edmonton, Canada. 118 p. https://central.bac-lac.gc.ca/.item?id=MQ40101&op=pdf&app=Library&oclc_number=1006917138.

Rodríguez-Cuicas, M.-E., Montero-Serrano, J.-C., St-Onge, G. and Normandeau, A. (2023). A 600-year marine record associated with the dynamics of the eastern Penny Ice Cap (Baffin Island, Nunavut, Canada). J. Quaternary Sci. https://doi.org/10.1002/jqs.3531.

Sadler, H. E., (1976). « Water, heat, and salt transports through Nares Strait, Ellesmere Island ». *Journal of the Fisheries Board of Canada*, 33(10), 2286-2295.

Samelson, R. M., & Barbour, P. L. (2008). Low-level Jets, Orographic Effects, and Extreme Events in Nares Strait: A Model-Based Mesoscale Climatology, Monthly Weather Review, 136(129,4746-4759.

Schweinsberg, A. D., Briner, J. P., Miller, G. H., Bennike, O., & Thomas, E. K. (2017). Local glaciation in West Greenland linked to North Atlantic Ocean circulation during the Holocene. *Geology*, 45(3), 195-198.

Serreze, M. C., and J. A. Francis. (2006). The Arctic Amplification Debate. Climatic Change 76: 241-264.

Sharp, M., Burgess, D. O., Cawkwell, F., Copland, L., Davis, J. A., Dowdeswell, E. K., & Wyatt, F. (2014). Remote sensing of recent glacier changes in the Canadian Arctic. *Global land ice measurements from space*, 205-228.

Shepard, F.P., 1954. Nomenclature based on sand-silt-clay ratios. J. Sediment. Petrol. 24, 151–158.

Solomina, O. N., R. S. Bradley, D. A. Hodgson, S. Ivy-Ochs, V. Jomelli, A. N. Mackintosh, A. Nesje, L. A. Owen, H. Wanner, G. C. Wiles, and N. E. Young. (2015). Holocene glacier fluctuations. Quaternary Science Reviews 111: 9-34.

Søndergaard, A.S., Larsen, N.K., Lecavalier, B.S., Olsen, J., Fitzpatrick, N.P., Kjær, K.H., & Khan, S.A. (2020). Early Holocene collapse of marine-based ice in northwest Greenland triggered by atmospheric warming. *Quaternary Science Reviews*, *239*, 106360.

Spielhagen, R. F., Werner, K., S rensen, S. A., Zamelczyk, K., Kandiano, E., Budeus, G., Husum, K., Marchitto, T. M. & Hald, M. (2011). Enhanced modern heat transfer to the Arctic by warm Atlantic water. Science. 331: 450–453.

Stevenard, N., Montero-Serrano, J. C., Eynaud, F., St-Onge, G., Zaragosi, S. & Copland, L. (2021). Lateglacial and Holocene sedimentary dynamics in northwestern Baffin Bay as recorded in sediment cores from Cape Norton Shaw Inlet (Nunavut, Canada). Boreas. https://doi.org/10.1111/bor.12575.

Stuiver, M., Reimer, P.J., Reimer, R.W., (2017). CALIB 7.1. Available online at: calib.qub.ac.uk/calib.

Stoner, J. S., & G. St-Onge. (2007). Chapter Three Magnetic Stratigraphy in Paleoceanography: Reversals, Excursions, Paleointensity, and Secular Variation, p. 99-138. *In* C. Hillaire–Marcel and A. De Vernal [eds.], Developments in Marine Geology. Elsevier.

St-Onge, G., Mulder, T., Francus, P. & Long, B. (2007). Continuous Physical Properties of Cored Marine Sediments (pp. 63-98). In C. Hillaire–Marcel & A. De Vernal [eds.], Developments in Marine Geology. Elsevier.

St-Onge, M.-P., & G. St-Onge. (2014). Environmental changes in Baffin Bay during the Holocene based on the physical and magnetic properties of sediment cores. Journal of Quaternary Science 29: 41-56.

Syvitski, J. P. (1989). On the deposition of sediment within glacier-influenced fjords: oceanographic controls. Marine Geology. 85: 301-329.

Tang, C.C.L., Ross, C.K., Yao, T., Petrie, B., DeTracey, B.M., & Dunlap, E. (2004). The circulation, water masses and sea-ice of Baffin Bay. Prog. Oceanogr. 63: 183–228.

Telford, R. J., Heegaard, E., & Birks, H. J. B. (2004). All age–depth models are wrong: but how badly. *Quaternary science reviews*, *23*(1-2), 1-5.

Thomas, E. K., Y. Huang, J. P. Briner, & S. McGrane. (2010). An assessment of leaf wax hydrogen isotopes as a climate proxy in proglacial arctic lake sediments, p. PP51A-1604.

Thorsteinsson, R., & Mayr, U. (1987). The sedimentary rocks of Devon Island, Canadian Arctic Achipelago. Geological survey of Canada, Memoir 411. 182p.

Toucanne, S. (2008). Reconstruction des transferts sédimentaires en provenance du système glaciaire de Mer d'Irlande et du paléo-fleuve Manche au cours des derniers cycles climatiques (Doctoral dissertation, Bordeaux 1).

Trachsel, M., & Telford, R. J. (2017). All age–depth models are wrong but are getting better. *The Holocene*, *27*(6), 860-869.

Trettin, H.P. (1991). Chapter 4 Tectonic Framework. In Geology of the Innuitian Orogen and Arctic Platform of Canada and Greenland. Edited by H.P. Trettin. Geological Survey of Canada, Geology of Canada, 3: 59–66.

Van den Boogaart, K. & Tolosana-Delgado, R. (2008). “Compositions”: A unified R package to analyze compositional data. Computers & Geosciences. 34. https://doi.org/10.1016/j.cageo.2006.11.017.

Van den Boogaart, K. & Tolosana-Delgado, R. (2021). Analyzing compositional data with R. Computers & Geosciences. 34. https://doi.org/10.1016/j.cageo.2006.11.017.

Van Wychen W., Copland L., & Burgess D. (2020). Ice Masses of the Eastern Canadian Arctic Archipelago. In O. Slaymaker & N. Catto (eds) Landscapes and Landforms of Eastern Canada. World Geomorphological Landscapes. Springer, Cham. https://doi.org/:10.1007/978-3-030-35137-3_13.

Von Eynatten, H., Tolosana-Delgado, R., & Karius, V. (2012). Sediment generation in modern glacial settings: Grain-size and source-rock control on sediment composition. Sedimentary Geology, 280, 80–92. https://doi.org/10.1016/j.sedgeo.2012.03.008.

Weeks, R., Laj, C., Endignoux, L., Fuller, M., Roberts, A., Manganne, R., Blanchard, E. & Goree, W. (1993). Improvements in long-core measurement techniques: Applications in palaeomagnetism and palaeoceanography. *Geophysical Journal International 114(3)*, 651-662.

Weidick, A. & Bennike, O. (2007). Quaternary glaciation history and glaciology of Jakobshavn Isbræ and the Disko Bugt region, West Greenland: a review. Geological Survey of Denmark and Greenland Bulletin 14, xx pp.

Weiser, J., Titschack, J., Kienast, M., McCave, I. N., Lochte, A. A., Saini, J., Stein, R. & Hebbeln, D. (2021): Atlantic water inflow to Labrador Sea and its interaction with ice sheet dynamics during the Holocene. Quaternary Science Reviews 256, 106833, https://doi.org/ 10.1016/j.quascirev.2021.106833.

White, A. & Copland, L. (2018). Area changes of glaciers across Northern Ellesmere Island, Nunavut, between ~1999 and ~2015. Journal of Glaciology 64, 609–623.

Wood, M., Rignot, E., Fenty, I., An, L., Bjørk, A., van den Broeke, M., & Zhang, H. (2021). Ocean forcing drives glacier retreat in Greenland. *Science Advances*, *7*(1), eaba7282.

Wu, L., Wilson,D. J.,Wang, R.,Yin, X., Chen, Z., Xiao,W. & Huang, M.(2020): Evaluating Zr/Rb ratio from XRF scanning as an indicator of grain-size variations of glaciomarine sediments in the Southern Ocean. Geochemistry, Geophysics, Geosystems 21, e2020GC009350, https://doi.org/10.1029/2020GC009350.

Zweng, M. & Münchow, A. (2006). Warming and freshening of Baffin Bay, 1916 – 2003. J. Geophys. Res. 111: C07016. https://doi.org/10.1029/2005JC003093.